TREATMENT OF PERIPROSTHETIC FRACTURES OF THE DISTAL FEMUR

PROTOTYPE DEVELOPMENT FOR THE TREATMENT OF PERIPROSTHETIC FRACTURES OF THE DISTAL FEMUR

By AARON MUIZELAAR, B.ENG.MGMT.

A Thesis Submitted in Partial Fulfillment of the Requirements for
the Degree Masters of Applied Science

McMaster University MASTERS OF APPLIED SCIENCE (2012) Hamilton, Ontario

(Mechanical Engineering)

TITLE: Prototype Development for the Treatment of Periprosthetic Fractures of the Distal Femur

AUTHOR: Aaron Muizelaar, B.Eng.Mgmt (McMaster University)

SUPERVISOR: Dr. Gregory R. Wohl & Dr. Cheryl E. Quenneville

NUMBER OF PAGES: 159

Abstract

Current stabilization methods for periprosthetic fractures of the distal femur have been inadequate in achieving sufficient fixation and can lead to complications rates as high as 29%. Therefore, the overall objective of this study was to design, manufacture and evaluate (experimentally and computationally) a novel plating method for improving the treatment of periprosthetic fractures of the distal femur.

Medial and lateral prototype plates were designed and manufactured based on the geometry of a synthetic femur and a femoral prosthesis. The two plates were linked via a compression screw and a small tab on each plate that inserts into pre-existing slots on the prosthesis to enhance rigidity of the construct. Synthetic femurs were used to assess the ability of the prototype plates to stabilize a periprosthetic fracture compared to a traditional single lateral plate. Each femur was subjected to a testing protocol that involved compressive and bending loading of the sample. The relative motion between the distal and proximal fragments during loading was then measured using both 2D and 3D motion tracking techniques. Both techniques revealed that the prototype bilateral plates were able to reduce motion of the fracture site compared to a single lateral plate.

The final objective concerned the development of a finite element model to represent the experimental testing. The fracture gap motion obtained from the final model did not completely agree with the experimental data; however, additional experimental measurements found that the majority of these differences could be attributed to

simplification made at the tab-slot interaction. Despite the difference, the model represents a significant step forward in the simulation of periprosthetic fracture treatment, and further refinement would allow for optimization of the plate design.

Overall, the results of this thesis indicate that an alternative approach to treating periprosthetic fractures exists that is capable of improving fracture stabilization.

Acknowledgements

I would like to take this opportunity to express my sincere appreciation to those who helped support me through the completion of this thesis. Thank you to Dr. Greg Wohl and Dr. Cheryl Quenneville for their support and guidance throughout this process, it has been a pleasure to work with you. Thank you to Dr. Mitch Winemaker for dreaming of a better way to treat periprosthetic fractures and all the clinical experience you contributed.

Thank you to all the other colleagues who have assisted in this project: Stryker Canada for the donation of equipment and supplies, Paul McNicol for your help in implanting the femurs, Paul Grunthal for your patent and 'industry relations' expertise, and anyone else who has contributed along the way.

I would like to thank all the technicians in the department (JP, Ron, Mark, Jim and Joe) for their help and advice. I would also like to thank all those in the biomechanical engineering lab for their help and the biomechanics lab in the kinesiology department for their assistance with the 3D motion capture system.

Finally, I would like to send my deepest thanks to my family and friends who have supported me in these past two years of my life. It means so much to have a group of people who love me the way you all do. Last and certainly not least, I would like to thank Emily for the incredible love she has shown me throughout this whole process. You have always been my number one fan and thank you for understanding how slow of a writer I am.

Table of Contents

List of Figures

List of Tables

List of Abbreviations and Medical Nomenclature

Abbreviations:

ANOVA	analysis of variance
CAD	computer aided design
CBP	condylar buttress plate
CNC	computer numerical control
CoCr	cobalt chromium
CT	computed tomography
DBL	double plated
DBL2	double plated with distal screws
DCP	dynamic compression plate
DCS	dynamic condylar screw
DMLS	direct metal laser sintering
FCL	far cortical locking
FEA	finite element analysis
IM Nail	Intramedullary nail
K	Kirschner
LAT	single lateral plate
LC-DCP	limited contact dynamic compression plate
LCP	locking compression plate
LISS	less invasive stabilization system
LSMG	liquid metal strain gauge
N	Newton
Pa	Pascal
PC-FIX	point contact fixator
PE	polyethylene
RMS	root mean square
TKR	total knee replacement
UHMWPE	ultra-high-molecular-weight polyethylene

Medical Nomenclature:

Anterior: Towards the front of the body

Arthroplasty: Surgery in which the arthritic or dysfunctional joint surface is replaced

Cancellous: The sponge like interior of bone that often located at the epiphysis

Collateral Ligament: Ligament located on either side of a hinge joint such as the knee

Comminuted: A fracture in which a bone is broken or crushed into a number of pieces

Condyle: Round prominence at the end of a bone (often part of the joint)

Coronal: Vertical plane that divides the body into front and back

Cortical: The hard outer layer of compact bone, forms diaphysis

Diaphysis: The central shaft of a long bone

Distal: Further away from a point of origin or attachment

Epiphysis: The expanded end of a long bone

Ex Vivo: Outside a plant or animal

Femur: The bone between the hip and the knee joints

In Vivo: In the living body of a plant or animal

Intramedullary canal: The canal in the center of the bone filled with marrow

Lamellar bone: Regular alignment of collagen into sheets, mechanically strong

Lateral: Away from the midline of the body

Lesser trochanter: Pyramidal process that projects from the proximal shaft of the femur

Medial: Towards the midline of the body

Osteoporosis: Disease characterized by low bone mass and deterioration of bone tissue

Percutaneous: Access to the body is obtained via needle-puncture of the skin

Posterior: Towards the back of the body

Proximal: Closer to a point of origin or attachment

Resorption: Destruction or dissolution of a tissue or part by biochemical activity

Sagittal: Vertical plane that divides the body into right and left halves

Tibia: The larger and stronger of the two bones in the leg below the knee

Valgus: Outward angulation of the distal segment of a bone or joint

Varus: Inward angulation of the distal segment of a bone or joint

Woven bone: Characterized by random organization of fibers, mechanically weak

Declaration of Academic Achievement

I, Aaron Muizelaar performed all design work, experimental testing, and analytical (finite element) modeling presented in this thesis and am solely responsible for the content. My co-supervisors, Drs. Cheryl Quenneville and Gregory Wohl supervised and provided guidance in this work. The design for the bilateral fracture fixation plates, presented in Chapter 2, was based on the original concept by Dr. Mitchell Winemaker.

CHAPTER 1: INTRODUCTION

1.1 FRACTURES AND FRACTURE HEALING

1.1.1 Fracture Mechanics and Classifications

Bone fracture occurs when excessive or prolonged forces are transmitted to the bone causing it to break. The load required to fracture a bone depends on several factors. Pre-existing conditions such as osteoporosis or other bone diseases will lower the strength of the bone and may cause fractures to occur at loads that normally wouldn't fracture healthy bone. Smaller forces can also cause fractures in healthy bones if they are repeated over time (Hamblen & Simpson, 2007). These forces induce microdamage in the bone that occurs at rates that exceed the rate of repair (Hamblen & Simpson, 2007).

The most common cause of fracture is a single large force that exceeds the ultimate strength of the bone (Hamblen & Simpson, 2007). This mode of failure is present in various patterns or mechanisms of fracture. Figure 1.1 shows the four main types of fracture mechanisms and the different loading scenarios that cause them (Carter & Spengler, 1982). While occasionally these loads can occur independently of one another, they are often experienced in combination; this can lead to more complex fractures involving multiple bone fragments.

1.1.2 Fracture Healing

Bone repair following fracture can occur under multiple conditions based on the amount of micromotion permitted between the fragments of bone. Primary healing occurs when fracture motion is within 0-2% of the total gap width (Egol et al., 2004). This type

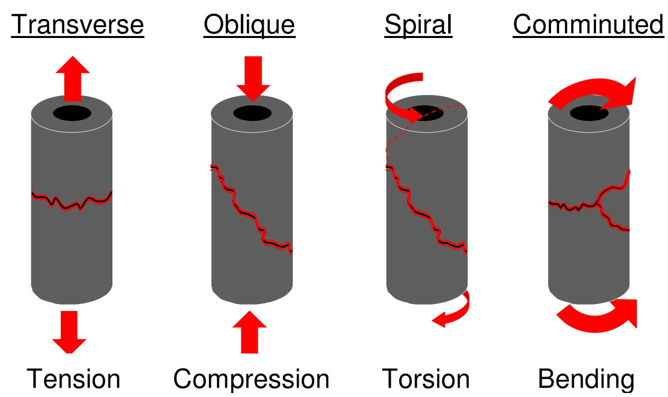

Figure 1.1: **Fracture mechanisms.**
Four basic classifications of fractures along with the corresponding mechanisms of failure.
(Adapted from: Carter & Spengler, 1982)

of healing demands compression of the bone fragments together under a controlled environment (Egol et al., 2004). Secondary healing is characterized by the formation of a callus around the fracture site and requires motions of 2-10% (Egol et al., 2004). An under-immobilized fracture (>10%) can result in excessive motion that leads to additional damage and delayed healing. In comparison, over-immobilization (<2%) can cause stress shielding (redistribution of load/stress to another area of bone) that prevents callus formation, thereby also delaying healing (Egol et al., 2004).

The range for secondary healing was found based on strain tolerances in certain types of bone (Perren, 2002). Strain values of up to 2% were found to be tolerated by lamellar bone, up to 10% tolerated by woven bone and for strains between 10% and 30% bone resorption occurs (Perren, 2002). It should be noted that one study suggested that secondary bone healing occurs when fracture gap motion is in the range of 5-15% (L. E. Claes & Heigele, 1999). However, the aforementioned 2-10% appears to be the more commonly used range in literature (Downing et al., 2008).

Fixation devices are often used to assist in controlling interfragmentary motion and maintaining the alignment of the bone. Internal fixation refers to the use of surgical implants within the body to promote fracture repair. These implants can include a combination of metallic plates, screws, and rods, and provide the surgeon with a great deal of flexibility to treat a wide range of fractures.

1.1.3.1 Intramedullary Nail Fixation of Fractures

Intramedullary (IM) nails are one common treatment method for internal fixation of fractures. The metallic nail is inserted into the intramedullary canal of a long bone and is often fixed at either end using screws (Figure 1.2). The IM nail in theory acts like an internal splint that helps to prevent excessive fracture motion under applied loads (Cunningham, 2001). They are best suited for mid-diaphyseal fractures since this allows adequate bone-nail surface contact for either fragment (Cunningham, 2001). Bending loads are transmitted along the nail to the bone on the opposite side of loading and are generally well handled by this device (Cunningham, 2001). Motion under torsional loads is also prevented through fixation of either end of the nail to the epiphysis (Cunningham, 2001). Finally, the nail is beneficial in that it allows slight motion when axial loads are applied, this helps to stimulate callus formation during healing (Cunningham, 2001).

Two main factors govern the level of fixation provided by an IM nail. First, the nail must have a relatively tight fit within the medullary canal, which will increase its contact with the bone (Cunningham, 2001). This is often controlled through reaming of the canal to a specified diameter. The stiffness of the nail also characterizes the level of fixation, and is often modified through optimization of the cross-sectional profile (Cunningham, 2001). Open-section hollow nails provide an interference fit when inserted into the bone and offer good bending resistance (Cunningham, 2001). Similar close-section nails do not give the desired interference fit but do provide similar bending resistance and increased torsional strength (Cunningham, 2001).

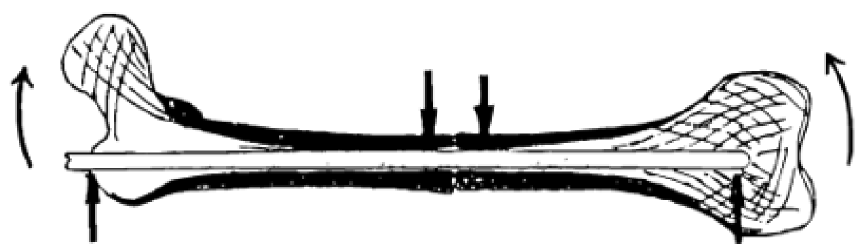

Figure 1.2: **Intramedullary nail under a bending load.**
A nail is shown inserted into the intramedullary canal of a femur. Bending (shown) or torsional loads are transmitted along the length of the nail and away from the fracture site.
(Cunningham, 2001)

1.1.3.3 Internal Plate Fixation of Fractures

Of the internal fixation options, plates provide the most treatment flexibility and have undergone substantial development in recent years. The first fixation plate was developed in 1895 by Lane as a simple metallic plate with several holes to allow screws to fasten it to the bone (Uhthoff et al., 2006). This style of plate was used for over fifty years with only slight metallurgical improvements to increase its corrosion resistance (Uhthoff et al., 2006). In 1949, Danis developed a method for incorporating axial interfragmentary compression using a plate with a tightening screw (Uhthoff et al., 2006). These “compression” plates targeted primary bone healing that required very little or no interfragmentary motion. Eventually the screw-based compression system transitioned into oval-tapered screw holes that compressed the fracture as the screw heads were inserted (Uhthoff et al., 2006). This style of plate is more commonly known as a dynamic compression plate (DCP). Despite moderate success, clinicians found that significant bone loss occurred directly under the plates, limiting their effective use.

One design feature hypothesized to contribute to this bone loss was the high contact area between the plate and the underlying bone (Uhthoff et al., 2006). Limited contact plates (LC-DCP) and point contact (PC-FIX) plates were then introduced to remedy this problem (Figure 1.3). Changing the geometry of the plates altered the contact area and created a plate that reduced the bone loss observed with previous DCP designs.

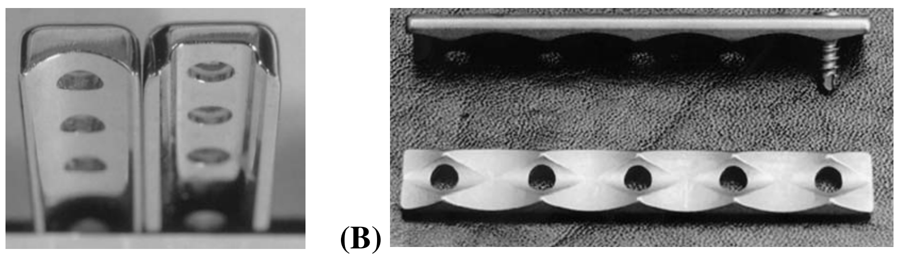

(A) (B)

Figure 1.3: Fracture plates with reduced contact area.
(A) Limited contact plates (LC-DCP) and **(B)** point contact (PC-FIX) plates were developed to reduce plate-bone contact area in order to prevent excessive bone loss and the disruption of vasculature.
(Uhthoff et al., 2006)

While bone loss was reduced with the use of these new plates, some patients experienced screw pull out and re-fracture after plate removal. The occurrence of re-fracture suggests that traditional compression plates were not capable of allowing primary bone healing to take place. Small motions between fragments that are compressed together create high strains that prevent optimal healing from occurring (Egol et al., 2004). By permitting a small gap between the fragments, and thus targeting secondary healing, strains can be reduced. Locking compression plates (LCP) were developed to decrease the incidence of screw pull-out and improve overall healing by allowing these small interfragmentary gaps (Egol et al., 2004).

In the LCP, traditional clearance screw holes were replaced with threaded holes. These threaded holes accommodate locking screws that have matching threaded heads. As the screw is inserted, the threads engage and the plate and screw become a single rigid construct. This construct no longer creates compression between the bone surface and plate. Since there is no compression, the plate geometry does not need to completely match the bone contours and a more generic plate can be used (Egol et al., 2004). Increased screw pull-out strength under bending loads can also be achieved through the use of locking screws (Figure 1.4). With standard plates the screws are able to orient themselves parallel to the applied load and minimal material is removed during pull-out (Egol et al., 2004). With fixed-angle devices, this rotation is constrained and the screws must remove a larger amount of material when the load is applied.

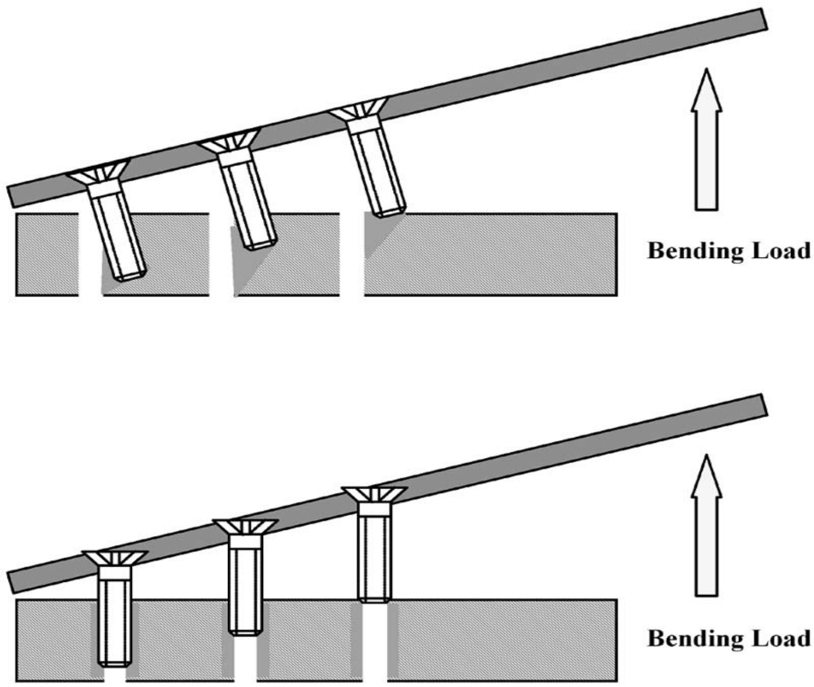

Figure 1.4: **Improved pull-out strength with a locking compression plate.**
The amount of disrupted bone (shaded) is larger for a locking compression plate [*top*] compared to a dynamic compression plate [*bottom*] during pull-out. This increases the bending load required for screw pull-out.
(Egol et al., 2004)

The primary limitation of a LCP is that the use of fixed-angle screws limits their applicability to complex comminuted fractures. Hybrid plates were introduced to remedy this issue by allowing surgeons to use both traditional compression screws (variable angle) and locking screws. This flexibility is achieved by either having slotted holes that will accept either screw (Figure 1.5) or by using threaded inserts that snap into clearance holes when a locking screw is required.

Recently, variable-angle locking screws have also been developed to provide the surgeon with even greater flexibility. Variable-axis self-locking threaded bushings are inserted into the screw holes and expand upon screw insertion to lock the screw at the desired angle (Otto et al., 2009). This new variable-angle system has shown comparable biomechanical characteristics (stiffness and strength) to traditional locking plates (Otto et al., 2009). Two-piece friction fit devices also achieve similar variable-angle flexibility but sacrifice stiffness and strength (Otto et al., 2009).

There is debate over how many screws are required for optimal fracture healing in plating systems, with the majority of clinicians recommending that there be at least two screws inserted into each fragment of bone (Gautier, 2003; Hertel et al., 2001). Caution also has to be exercised when preparing the holes for screw insertion. Too small of a pilot hole will result in a high insertion torque and may crack the bone; too large of a pilot hole will result in poor fixation. Optimal pilot hole size has been suggested to be 85-90% of the major screw diameter (Cunningham, 2001). Pre-tapping of the holes should be

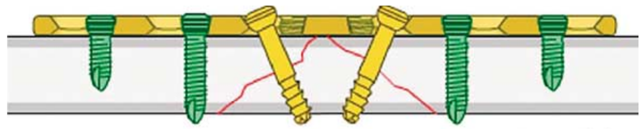

Figure 1.5: Treatment of a comminuted fracture with a hybrid plate.
A comminuted fracture is treated using bone fixed-angle locking (green) and variable-angle compression (yellow) screws.
(Wagner, 2003)

reserved only for cortical bone screws since it limits cracking of the bone during screw insertion (Cunningham, 2001). Since cancellous bone is much more porous, tapping should not be performed as it can remove bone that helps to increase the pull-out strength (Cunningham, 2001). To assist in fixation, screw thread designs have been optimized for either cortical or cancellous bone. Cancellous bone screws have a coarse thread with large teeth to increase the contact area between the screw and bone (Cunningham, 2001). As the screw is inserted, the threads displace the bone towards the walls of the hole to create a more dense contact surface and increase pull-out strength. Cortical screws have a finer thread and smaller teeth since excessive bone displacement during insertion can lead to cracking of the bone (Cunningham, 2001).

Another development in screw technology is the use of far cortical locking (FCL) screws. Locking plates are designed to target secondary bone healing; however, they have been reported to be as stiff as conventional plates that target primary healing (Fitzpatrick et al., 2009). Therefore, reducing the stiffness of the construct would better stimulate secondary bone healing by allowing the required micromotion. FCL screws reduce the stiffness of the construct and increase the strength of the healed bone (Bottlang et al., 2010). The shaft of a standard locking screw is machined down to create clearance between the shaft and the bone (Figure 1.6). This shaft is then able to bend elastically under axial loads to allow for small amounts of interfragmentary motion.

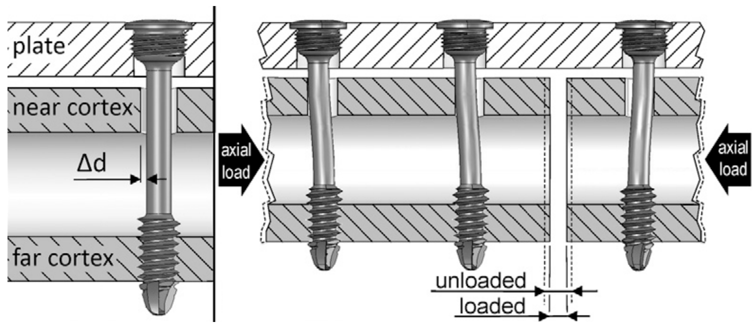

Figure 1.6: **Mechanics of far cortical locking (FCL) screws.**
The machined shaft of the FCL screws introduces a clearance (Δd) between the bone and screw. The reduced shaft diameter also increases the flexibility of the screw. This decreases the overall stiffness of the construct and allows a certain amount of controlled micromotion of the fracture site.
(Bottlang et al., 2010)

1.1.4 Current Research in Fracture Treatment

A large amount of current internal fixation research is focused on customizing and increasing the flexibility of treatment for as many different fracture scenarios as possible. This development is at work on multiple levels, all with the intention of improving healing effectiveness and efficiency. While traditional plates were designed for the "average" patient, orthopaedic companies continue to expand their product lines to reach those on the edges of the scale. Patient-specific plate customization would allow for improved treatment of complex fractures in areas where the profile and size of the plate is crucial. Skull fractures along with certain pelvic or spinal fractures may require low-profile plates to match specific contours of the native bone so as to not affect the function of surrounding structures. Using pre-operative imaging techniques to generate 3D CAD models of the fracture site would allow engineers and clinicians to construct virtual plates that could then be manufactured. The current method of patient-specific customization involves plastic deformation of generic plates by the surgeon just prior to implantation.

More recent developments in plate design are focused on managing fractures that are in difficult locations and increasingly more complex. While companies are increasing the size options for more standard plates they are also increasing the types of plates so that any possible fracture in any location may someday soon be treatable. The process of developing a new method of treatment for a fracture that was once poorly treated requires exhaustive research to determine the best possible approach. Both experimental and computational work is often performed to gain a complete understanding of the way in which plates or other devices influence fracture healing.

1.2 PERIPROSTHETIC FRACTURES OF THE DISTAL FEMUR

Periprosthetic fractures are fractures that occur around a previously-implanted prosthesis. In patients who have undergone a total knee replacement (TKR), periprosthetic fractures occur in the distal femur at a rate of 0.6-2.5% (Bong et al., 2002). In addition to traumatic incidents, other risk factors for distal femoral periprosthetic fractures include osteoporosis, wear of the polyethylene tibial insert, anterior femoral notching during TKR, and revision surgeries (Bong et al., 2002; Nauth et al., 2011).

TKR's are becoming an exceedingly common procedure, and some estimates have forecasted up to a 670% increase (to 3.48 million / year in the United States) between the years 2005 and 2030 (Kurtz et al., 2007). This increase is likely due to a number of factors; most notably elderly patients are living longer and remaining active in their later years (Platzer et al., 2010). These patients have higher performance expectations and demands on the joint that can lead to multiple revisions being performed over the remainder of their lifetime. As the number of procedures increases so too will the incidence of periprosthetic fractures (Streubel et al., 2010).

With the projected increase in the number fractures, proper management of this injury must be achieved to ensure quality of life for patients. Current treatment methods include various types of plates, intramedullary rods, external fixation, condylar screws, and revision arthroplasty with a long-stem femoral prosthesis (Bong et al., 2002). While these options are capable of treating some fractures, complication rates are increased for comminuted fractures or in patients with poor distal bone quality (McGraw & Kumar, 2010). Reported complications include nonunion (9%), fixation failure (4%), infection

(3%), and revision surgery (13%) (Herrera et al., 2008). Other issues with these treatment methods are that they are not always compatible with the existing prosthesis, and at times the high number of screws required to stabilize the fracture can be invasive. For example, intramedullary nails are not always compatible with prostheses that have a femoral box, and their performance deteriorates rapidly when treating comminuted fractures (Bong et al., 2002). The screws can disrupt the vascular network surrounding the fracture leading to poor healing and increased recovery times for patients.

1.2.1 Experimental Research

Very few studies have investigated the biomechanical behaviour of different treatment options for periprosthetic fractures. Instead, the majority of experimental biomechanical research has focused on treating distal femur fractures without the presence of a prosthesis. However, the tools, techniques, and knowledge gained from these studies are still useful for determining the best option for fixing periprosthetic fractures of the distal femur.

1.2.1.1 Marti et al. – 2001

A 2001 study by Marti et al. compared three different fixation techniques for distal femur fractures (Marti et al., 2001). A dynamic condylar screw (DCS) and a condylar buttress plate (CBP) were compared with the then recently-introduced locking screw plate system: the Less Invasive Stabilization System (LISS) (Figure 1.7).

Two different configurations were tested with each of the three treatment methods using eleven pairs of human cadaveric limbs. The first configuration tested the ability of the plates to stabilize a 10 mm supracondylar gap in the distal portion of the femur. The

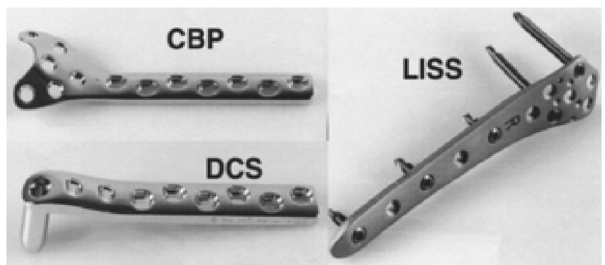

Figure 1.7: Three plating techniques used to treat distal femur fractures.
Three different fixation techniques are shown: condylar buttress plate (CBP), dynamic condylar screw (DCS) and the less invasive stabilization system (LISS).
(Marti et al., 2001)

second setup studied the screw anchorage of the systems using a 10 mm gap in the epiphysis. Each sample was embedded in polymethylmethacrylate (at an angle of 13° for configuration 1) and loaded using a uni-axial compression tester. The load was applied through the proximal portion of the femur in an increasing cyclic fashion (Figure 1.8). Four steps (F_{max}=1,000 N, 1,400 N, 1,800 N, and 2,200 N) of ten cycles each (between F_{max} and F_{min}=100 N) were applied at a rate of 20 N/s. Medial and lateral optical displacement transducers were used to track the motion of the fracture gap during loading.

The results obtained from configuration 1 (the supracondylar fracture) showed the LISS had less plastic deformation in 72% of the paired cadaveric comparisons. In configuration 2 (the epiphyseal fracture), the LISS had less plastic deformation in 83% percent of the samples but had a higher elastic deformation. The higher elastic deformation in the LISS samples was attributed to the material property differences between titanium (LISS) and steel (CBP, DCS). The authors concluded that the promising biomechanical results for the LISS construct indicate it as a possible alternative for treating distal femur fractures.

1.2.1.2 Higgins et al. – 2007

A similar cadaveric study was conducted by Higgins et al. in their comparison of a distal femoral locking plate to a condylar blade plate. Eight femur pairs were randomly assigned one of the two fixation options, potted proximally at 6° varus angulation, and a 10 mm transverse fracture gap was created.

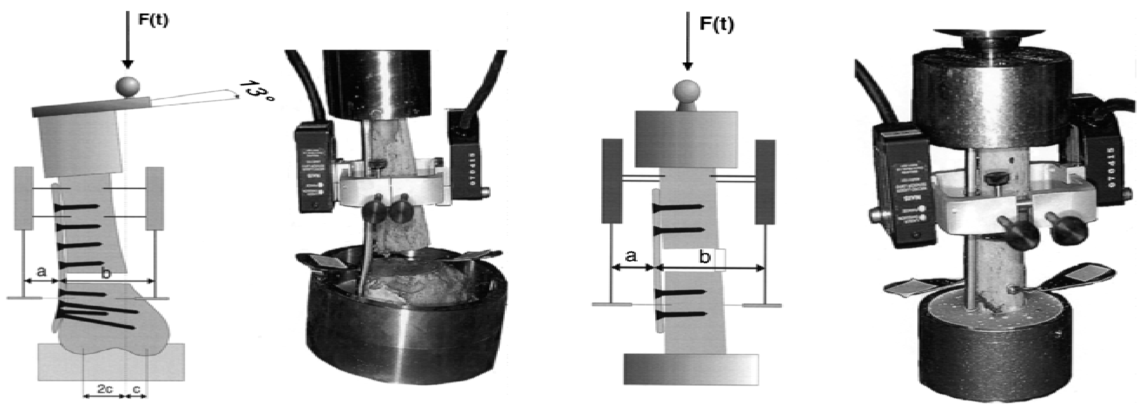

Figure 1.8: **Fractures fixation in two different regions is tested.**
The first configuration [*left*] tests the ability of the plates to stabilize a distal femur fracture. The second configuration [*right*] studied the screw anchorage of the systems using a gap in the epiphysis.
(Marti et al., 2001)

A servo-hydraulic testing machine loaded each sample via a custom fiberglass resin mold to apply an axial force evenly to the condyles from 100 N-1,000 N at 100 N/s. Using the same force magnitudes, a cyclic load was applied for 10,000 cycles at 3Hz. Finally, the constructs were loaded to failure from 100 N at 100 N/s. Fracture gap displacement was recorded during all tests using the data collection system on the testing machine. The average plastic deformation after cyclic loading was 1.04±0.33 mm for the locking plate group and 1.70±0.45 mm for the blade plate. Similarly, the average loads to failures were 9085±1585 N and 5591±945 N, respectively. These results suggest superior performance of the locking plate when fixing fractures of the distal femur.

1.2.1.3 Heiney et al. – 2009

The performance of plating systems has also been compared to other forms of fixation available to the surgeon. In a 2009 study, Heiney *et al.* compared a DCS (similar to Marti *et al.*) and locking plate (LCP) to an intramedullary (IM) nail (Figure 1.9) (Heiney et al., 2009). Unlike the previously-mentioned cadaveric studies, these constructs were tested using eighteen 2nd generation synthetic femurs (Pacific Research Laboratories, Vashon Island, WA). In addition to a standard 10 mm transverse fracture, the study also conducted tests on a more unstable T-fracture. The simple transverse fracture was first created and loaded non-destructively. Then an intercondylar T-fracture was created in each specimen and tested for fatigue. Each femur was potted at 9-10° of valgus angulation and loaded using a servo-hydraulic testing machine. A flat “frictionless” plate was used to load the condyles evenly at various axial loads. The non-destructive cyclic testing was conducted up to 2,224 N for eight cycles. Fatigue testing

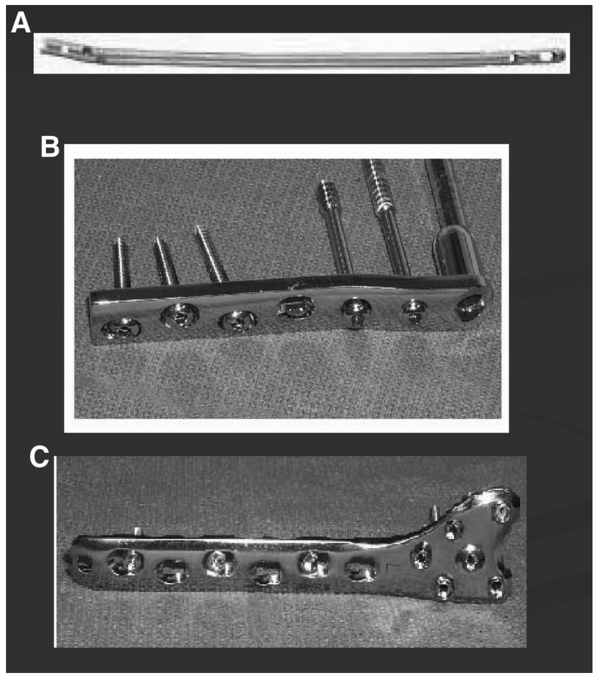

Figure 1.9: **Three different options for treating a distal femur fracture.**
The biomechanical performance of three different treatment options were compared: **[A]** retrograde intramedullary nail, **[B]** dynamic condylar screw (DCS), **[C]** locking plate (LCP).
(Heiney et al., 2009)

was applied between 134N-1,780 N for 80,000 cycles and then increased to 134 N-2,670 N until failure. Three 25.4 mm liquid metal strain gauges (LMSG) were used to measure the anterior, posterior, and medial fracture motion during the tests.

Based on the data from the LMSG's, the stiffness of the IM nail, DCS, and LCP were determined to be 1,106, 750, and 625 N/mm, respectively. The non-destructive tests yielded maximal gap micromotion for the IM nail, DCS, and LCP of 1.96, 10.55, and 17.74 mm, respectively. Only eight samples were available for fatigue testing (3 DCS, 3 LCP, 2 IM nail). During the second stage of fatigue testing, the distal screws of the IM nail failed at 9,000 cycles, the DCS did not fail, and the LCP failed at an average of 21,250 cycles. These results suggest that while an IM nail may be the strongest construct for simple transverse fractures, when more complicated patterns are introduced (*e.g.*, a T-fracture) the nail's performance drastically declines.

1.2.1.4 Bong et al. – 2002

There are very few studies that replicate a periprosthetic distal femur fracture. One such study compared an IM nail to the LISS locking plate system on cadaveric samples implanted with a femoral prosthesis (Bong et al., 2002). Six pairs of matched cadaveric femurs were implanted with one of the two devices, potted in acrylic cement, and an oblique fracture was created at 45° just proximal to the prosthesis. The initial fracture gap size was created to be very small (size not specified). Each sample was loaded statically via a polyethylene tibial insert in the anterior (200 N), posterior (200 N), and varus/valgus directions (500 N). The gap was then increased to 10 mm and each sample was re-tested. The specimens were also tested cyclically to a maximum load of 500 N for 10,000 cycles at 5 Hz on a point 4 mm medial to the center of the tibial insert. Finally, each sample was loaded to an axial load of 500 N through each condyle (simulating varus and valgus loading).

Fracture displacement and translation were measured with a calliper to the nearest 0.1 mm using paired K-wires attached to the anterior, lateral, and medial fragments. A goniometer was also used to measure relative rotation of the fragments to the nearest degree. In the statically loaded tests with minimal fracture gap both constructs behaved similarly in the varus/valgus load cases. However, during anterior and posterior loading the IM nail allowed significantly less displacement. When the fracture gap was created, the samples stabilized with an IM nail had an 83% reduction in fracture displacement when compared to the plated samples. However, the samples stabilized with the LISS had a 93% reduction (compared to the IM nail) in fracture gap displacement when a valgus load was applied with a 10 mm gap. This difference is likely due to the lever arm that is created in varus loading of the LISS samples. In conclusion, the authors suggested that both treatment options have benefits and their use should depend on the type of fracture encountered.

1.2.1.5 Salas et al. – 2011

In 2011, Salas *et al.* conducted a study comparing a locking plate and IM nail construct in both cadaveric and synthetic samples (Salas et al., 2011a). Six 4th generation synthetic femurs with an osteoporotic cancellous foam were implanted with an IM nail, while five synthetic and two cadaveric samples were implanted with the locking plate. A wedge pattern fracture was created with a 10 mm transverse gap halfway through the bone from the medial side and a 1 mm gap continuing through to the lateral side.

The whole femurs were first subjected to combined axial/torsion cyclic loading (Axial: 50-500 N, 5000 cycles, 2 Hz; Torsion: 6° clockwise/counter-clockwise rotation). Medial and lateral cyclic bending loads were then applied to a maximum displacement of 10 mm (in each direction) at 2 Hz for 5000 cycles. Following cyclic loading, medial bending was simulated by displacing the femoral head at 1 mm/s until failure. Load vs. displacement data were collected directly from the loading machine for all tests. During the axial cyclic loading the locking plates were found to be more stable than the IM nails. The medial and lateral bending induced damage on the IM nail construct while the locking plate hardened with increasing cycles. Failure was also seen only in the locking plate samples, with the synthetic and cadaveric bones exhibiting similar fracture patterns.

1.2.2 Computational Research

Experimental limitations such as sample size and the time required to conduct multiple studies restrict the number of parameters that can be examined in the testing of fracture plate fixation. Computational testing using finite element analysis (FEA) allows for easier modification of parameters that are normally difficult and time consuming to alter during experimental testing. In the case of fracture treatment research, these parameters can include loading conditions, materials, treatment option design and boundary conditions. It also provides knowledge of the strain distribution throughout the entire bone as opposed to only discrete locations when using strain gauges experimentally.

FEA consists of creating virtual geometric models of the components of the experimental setup. The geometry of these components is then decomposed into numerous small geometrical shapes (elements) connected together at their corners (nodes). All of the elements and nodes for a single component combine to form a mesh. Material properties can then be applied to the elements within the mesh followed by loads and boundary conditions. The material properties are used to define the stiffness of the elements within the mesh. It is this stiffness that is used to determine the displacement of the nodes under the applied loads. Boundary conditions are used as a means of specifying initial conditions or restrictions in the behaviour of the model (*e.g.*, fixed base, constraining the movement of a component to a certain direction). Interactions (contact parameters) or other constraints between components can also be defined to help model the desired environment. After these primary variables have been specified, the model can be analyzed for a variety of outputs (primarily relating to stress, strain, and displacement). It is critical to verify the FE model against experimental testing in order to ensure that the results are valid.

1.2.2.1 Salas et al. – 2011

Only one known study was found to have investigated the treatment of distal femur fractures using FEA. As a continuation of the study described in Section 1.2.1.5, Salas et al. performed FEA on both the locking plate and the IM nail to investigate the probability of periprosthetic fracture (Salas et al., 2011b). A three-dimensional model of the synthetic bone that was tested was imported into ANSYS® (ANSYS Inc., Canonsburg, PA) and assigned appropriate material properties. Representations of the screws, plate, nail, and nuts were also imported into the model. To simulate the experimental boundary conditions, the anterior and posterior regions of the condyles were fixed in all degrees of freedom (Figure 1.10). The screws were assumed to be fully fixed to the locking plate and screw-to-bone and IM nail-to-bone frictional contact properties were assigned.

A nonlinear elastic, static structural analysis was performed on each model and the load-displacement results were compared to the corresponding experimental values for validation. Upon successful validation (RMS error < 3 mm), a probabilistic evaluation of fracture was conducted using material properties that varied randomly with each test. This analysis found that the locking plate had a probability of failure of 21.8% while the IM nail had that of only 0.019%.

1.2.2.2 Bougherara et al. – 2010

As part of the development of a hybrid knee replacement system, a FE model was developed to investigate stress shielding in the distal femur (Bougherara et al., 2010). A three-dimensional model of a 4th generation synthetic femur was generated using a computed tomography (CT) scan and imported into SolidWorks® (Dassault Systèmes, Waltham, MA). The components of the TKR were created in SolidWorks and 'virtual surgery' was performed to create a complete model. The model was then imported into ANSYS Workbench and each component was meshed using 10-node tetrahedral elements. The surfaces between all the components were assigned 'bonded' contacts to

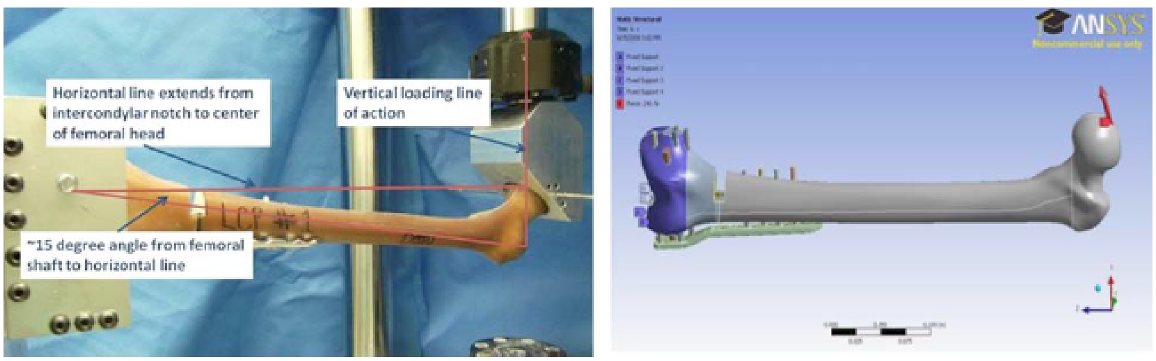

Figure 1.10: **Comparison of experimental and FE models.**
Images of both the experimental and FE models are shown. The boundary conditions and loads from the experimental setup were replicated in the model.
(Salas et al., 2011b).

prevent relative motion except for between the tibial insert and the femoral implant (coefficient of friction of 0.04). Normally a thin layer of bone cement is applied between the femoral component and the host bone. However, a pilot study by the same authors found that replacing the bone cement in the FE model with a 'bonded' contact constraint resulted in 98% of the stress levels.

The cement block used for potting the femur was modelled as a rigid fixed support using boundary conditions. Similarly, the four side faces of the cancellous block were constrained to have no displacement. This replicated the experimental setup by allowing only compressive forces to be applied to the tibial components through the top face of the block. Finally, linear elastic, isotropic material properties were assigned to each component.

The model was validated through comparison with strain data collected from experimental results in which a 3000 N compressive load was applied to the cancellous block. The study also compared surface stresses on the distal femur between a standard TKR and the novel hybrid TKR under three knee flexion angles. Stress shielding was found to be lower for the hybrid system in each of the orientations.

1.2.2.4 Shah et al. – 2011

A 2011 study compared fixation methods for femur fractures occurring around hip implants using FEA (Shah et al., 2011). Three constructs composed of a plate secured by different combinations of screws and cables were tested experimentally on synthetic femurs. Strain data were obtained from these tests and used in the validation of the FE model. Similarly to the previous study, the experimental samples were modelled in SolidWorks and imported into ANSYS for analysis (Figure 1.11).

The screws were simplified to be non-threaded rods tied directly to the femur. This simplification has been validated previously to show no significant change in the force, shear stress and energy during screw pull-out (Zdero et al., 2008). Plate/screw, bone/screw, bone/cement, and bone/cable interactions were modelled as being 'bonded' to simulate bone growth around and onto these components (Shah et al., 2011). The femur was constrained within a rigid fixed cement block. Each component was then meshed using 10-node tetrahedral elements and assigned appropriate material properties.

The FE model was successfully validated by the experimental strain data with a correlation coefficient of R^2=0.92. Construct stiffness was then found for each of the three treatment methods as well as the distribution of stress through the cortical bone.

1.3 STUDY RATIONALE

Several groups have sought to determine the optimal method for treating distal femur fractures experimentally. Computational research in this area has been less common, as a high level of expertise is often required to achieve accurate results. When implemented, FEA can be used to validate experimental results and investigate the stress shielding effects of implants. Very few studies (experimental or computational) have considered periprosthetic distal femur fractures and none have looked at developing an alternative treatment method to improve stability and outcomes for patients. Current clinical use of plating systems for treating these types of fractures has been satisfactory

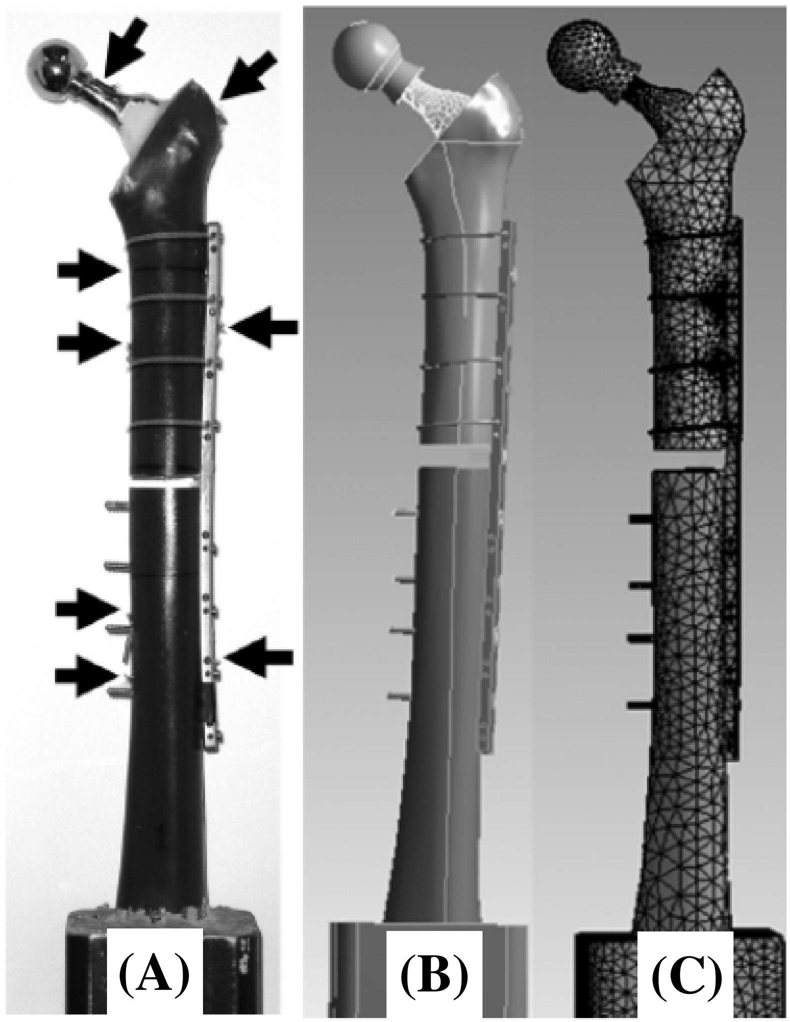

Figure 1.11: **FE model of a periprosthetic fracture of the proximal femur.**
The development of a FE model from **(A)** the experimental sample to **(B)** the CAD model to **(C)** the meshed construct in ANSYS.
(Shah et al., 2011)

and complications tend to arise in patients with comminuted fractures or poor distal bone quality.

The overall goal of this study was to design, manufacture and evaluate a novel plating method for treating periprosthetic fractures. Experimental testing was performed to compare the performance of the prototype to that of a currently used method of treatment. A finite element model was then developed to replicate the experimental setup and can be used to further refine the plating method. The overall motivation behind this study was to develop a new tool for treating these problematic fractures that would improve patient outcomes by controlling the relative fracture motion.

1.5 Objectives and Hypotheses

The objectives of this thesis were:

1. To develop a novel concept for treating distal femur periprosthetic fractures into functional plates that target the amount of fracture motion required to enhance healing and conform to existing surgical techniques;
2. To experimentally evaluate the performance of the prototype plates against a commercially-available single lateral plate (current method of choice for treating these fractures) under axial and bending loads; and
3. To develop a finite element model of the experimental test setup and validate it against the experimental results.

The corresponding hypotheses were:

1. Prototype plates for treating periprosthetic fracture can be developed that are capable of increasing the stabilization of the fracture site and conform to existing surgical techniques.
2. The prototype plates will reduce the relative motion observed at the fracture site when experimentally compared to a single lateral plate.
3. A finite element model can be developed with results that compare to the relative fracture motion obtained during experimental testing.

1.6 THESIS OVERVIEW

This thesis is written in an integrated article format. Chapter 2 describes the development and manufacturing of a novel plating system for treating periprosthetic distal femur fractures. Chapter 3 outlines the experimental study that was conducted to evaluate the proposed plates against a current method of treatment. Chapter 4 describes the development and results of a finite element model that simulates the experimental testing. Chapter 5 summarizes the conclusions of this thesis, its potential impact on clinical treatment of these fractures, and highlights future work in this area.

CHAPTER 2: DESIGN AND MANUFACTURING

2.1 INTRODUCTION

To address the high complication rates and poor management of periprosthetic fractures of the distal femur, Dr. Mitchell Winemaker conceptualized a treatment method whereby fracture fixation could be enhanced through attachment directly to the prosthesis. He envisioned plates on either side of the femur (medial and lateral plates) with tabs that insert directly into pre-existing slots on the sides of the femoral component of the total knee replacement (TKR) (Figure 2.1 and Figure 2.2). These tabs would then be held in place by a transverse compression screw inserted through the distal bone that applies a compressive force to the construct (Figure 2.3). Finally, the plates would be aligned with the femur and several standard proximal locking screws inserted into each plate.

The medial plate needs to be shorter than the lateral plate in order to reduce the disruption of soft tissues and vascularity. In principle, it is present to provide a point to which the transverse screw can apply the required compressive force and counteract any forces applied directly to the medial condyle. In comparison, the lateral plate would be designed to be much like existing distal femoral locking plates in terms of length and shape, with the attachment tab as an extension off the distal end.

Other treatment methods for these fractures (intramedullary (IM) nails and distal femoral locking plates) rely solely on fixation through the distal bone. However, this bone can be quite weak due to osteoporosis or stress shielding from the implant. Therefore, the

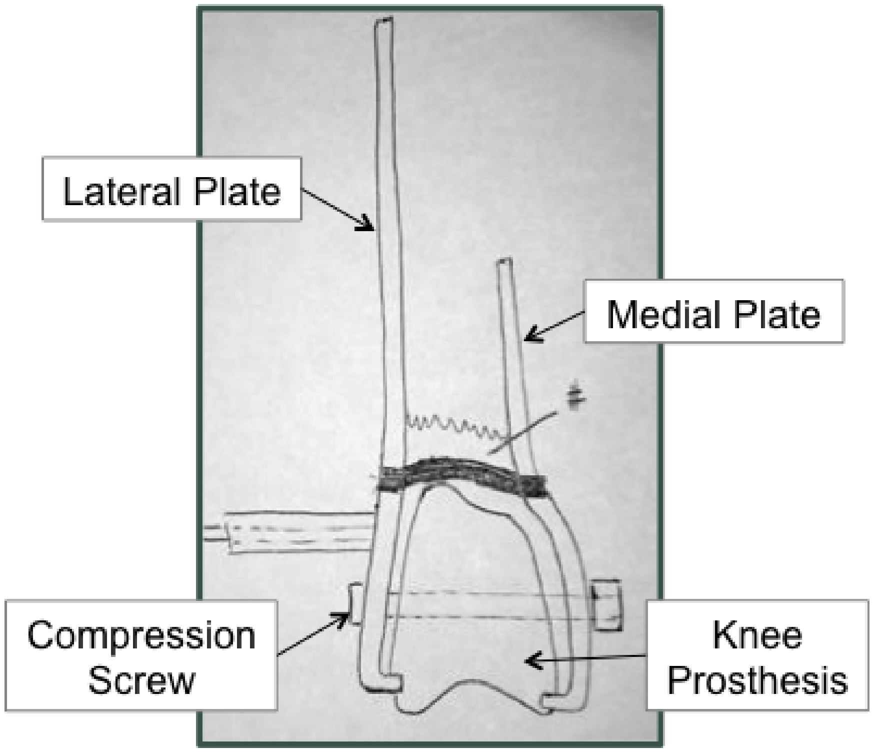

Figure 2.1: **Conceptual drawing of a double plated construct.**
A conceptual drawing created by Dr. Winemaker showing the anterior view of a distal femur. There are medial and lateral plates with tabs that insert directly into pre-existing slots on the prosthesis. A transverse compression screw is then used to apply a compressive force to the plates and hold them securely in place.
(Winemaker, 2007)

Figure 2.2: **Femoral component of a TKR showing attachment slots.**
A currently-available femoral component (Scorpio 7L PS [71-4507L]; Stryker Orthopaedics, Mahwah, NJ) with one of the pre-existing slots highlighted on the lateral aspect of the prosthesis. A similar slot is located on the medial side.
(Stryker, 2012)

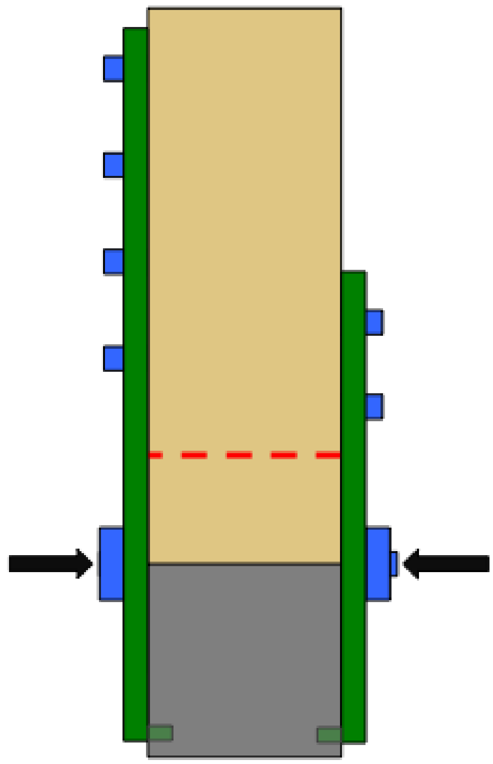

Figure 2.3: **Simplified schematic of the double plated construct.**
A simplified schematic of the proposed double plated construct is shown. A periprosthetic fracture (dotted red line) is stabilized using the medial and lateral plates (green), which are secured into the attachment slots of the femoral prosthesis (grey) by the transverse compression screw and additional proximal screws (blue).

envisioned plates were made to bypass the potentially weak bone and achieve stabilization through the more rigid prosthesis. Regardless of the kind of fracture, quality of bone, or combination of the two, sufficient fixation should be attainable through the rigid construct.

2.2 DESIGN

The medial and lateral plates were designed with three-dimensional computer aided design (CAD) software (Inventor 2011; Autodesk, San Rafael, CA) using the geometry of a composite femur (Biomed Town: “femur_sawbone.zip”; https://www.biomedtown.org/biomed_town/LHDL/Reception/datarepository/repositories/BEL/repository/Composite_femur_3rd_gen_solid_model) and a femoral prosthesis (Scorpio 7L PS [71-4507L]; Stryker Orthopaedics, Mahwah, NJ) (Figure 2.4). The original femur model was created to represent the geometry of a “large” format 3rd generation synthetic femur (Sawbones; Pacific Research Laboratories, Vashon, WA). Since 4th generation medium femurs were used for experimental testing (to match the size of the femoral component available), the 3D model was adjusted. Only the material properties were modified in the development of the newer 4th generation femur, with the morphology being identical to that of the 3rd generation model. The “large” model was scaled down to “medium” size using the dimensions provided on the Pacific Research Laboratories website (med/lat = 80%, ant/post = 90%, prox/dist = 94%) (Figure 2.5).

Both the femur and the prosthesis were imported into Inventor and ‘virtual surgery’ was performed to join the two models. Cuts along the femoral condyles were

Figure 2.4: **Profile of the femoral prosthesis.**
The profile of the prosthesis is shown and highlighted by the black lines. This profile guided the cuts that were created on the condyles of the femur in order to perform the "virtual surgery". One of the pre-existing slots on the side of the prosthesis is also shown (matching slot on the opposite side).

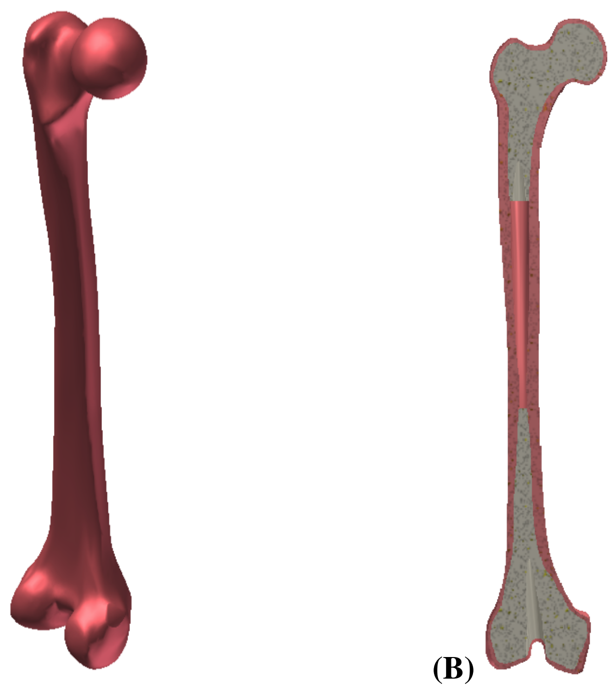

(A) **(B)**

Figure 2.5: **3D model of a 'medium' synthetic femur.**
(A) The 3D model of a 'medium' left femur is based on the geometry of a 3rd generation synthetic femur (Sawbones; Pacific Research Laboratories, Vashon, WA). **(B)** The two layers of bone are shown in a cut view of the model: the cortical shell and the cancellous core.

created to match the profile of the prosthesis. The orientations of the cuts were measured from a synthetic bone cut using the appropriate surgical tools and techniques. Surface constraints were then added to simulate the bone cement that fixed the prosthesis to the femur. Finally, the attachment sites of the medial and lateral collateral ligaments were projected onto the femur using the maximum possible footprint as described in a previous study (Otake et al., 2007) and shown in Figure 2.6.

2.2.1 Design Specifics

The exterior surface geometry of the femur was extruded to create medial and lateral plates. The plates were then modified to wrap over and anterior to the ligament attachment sites to preserve ligament function. Approximately 3-mm of clearance was created between the plates and the expected attachment sites. This clearance was introduced into the design to account for any differences between the 3D femur model and the femurs used experimentally. Extensions were also added to either plate in the form of tabs that fit securely in the existing slots on the femoral component (Figure 2.7). The tab profile was obtained directly from the prosthesis model and measured 0.1-mm smaller in all dimensions to create a tight fit within the slot.

For proof of concept, a 110-mm ¼-20 UNC threaded rod was used for the transverse compression screw, with a nut on either side to provide the compressive force to the plates. The location of the clearance holes for the screw was primarily governed by the profile of the plates required to avoid the ligament origins. The holes were placed in the middle of the plates, which resulted in the screw being slightly anterior to the

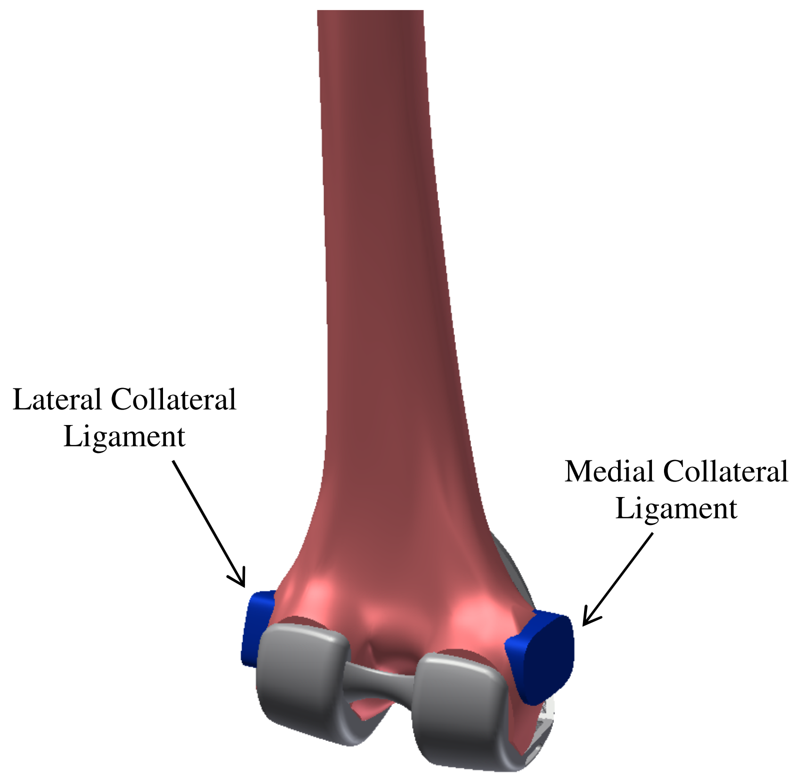

Figure 2.6: **3D femur model showing collateral ligament attachment sites.**
A synthetic femur model implanted with the femoral prosthesis and showing the attachment sites for the medial and lateral collateral ligaments (shown in blue). The locations of the ligament attachment sites were based on existing anatomical data (Otake et al., 2007).

Figure 2.7: **Medial and lateral plates created from femur geometry.**
Initially the medial and lateral plates were generated by extruding the surface geometry of the femur. Ligament attachment sites were avoided and tabs were created to insert directly into the pre-existing slots on the prosthesis.

prosthesis slots. The screw also had to be placed proximal enough as to not disrupt the prosthesis or the notch created during the TKR procedure (Figure 2.8). Another clearance hole for an additional compression screw was added 20-mm proximal to the first hole to increase flexibility for the surgeon.

Plate thickness was chosen to be between 3 to 6-mm (depending on the location measured) and was based on the thickness of an existing distal femoral locking plate (AxSOS distal lateral femur locking plate [437510]; Stryker Orthopaedics, Stryker Orthopaedics, Mahwah, NJ). The lateral plate length was 170-mm based on the reference lateral plate. The medial plate length was 120-mm since it is only required to act as an anchoring point for the transverse compression screw. A shorter plate is also less invasive and helps to preserve any surrounding vasculature. ANSI M6x1 holes were added to allow existing AxSOS 5.0mm locking screws to be used for fixation directly to the bone. Through consultation with Dr. Winemaker, the holes were spaced 20-mm apart, thus allowing for four holes in the proximal aspect of the lateral plate and two holes in the medial plate. Detailed drawings of both the medial and lateral plates can be found in Appendix A.

The initial design of the plates as described had various complex contours in multiple planes that made them difficult to manufacture given the available manufacturing resources. Therefore, several simplifications had to be made so that the majority of machining could be performed in two planes (Figure 2.9). Comparing Figure 2.9 to the original design in Figure 2.7, the most noticeable changes in the plates occurred

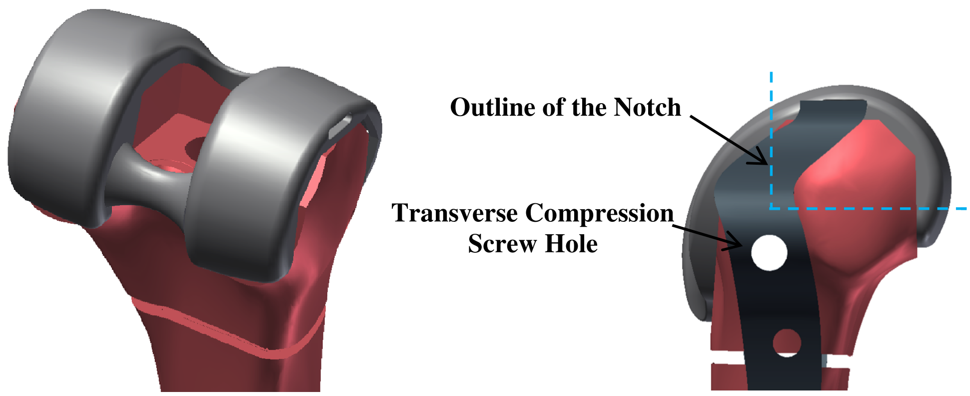

Figure 2.8: **Placement of the transverse compression screw.**
The transverse compression screw was placed in the middle of the plates and close to the femoral component without infringing on the notch created during the TKR procedure. In some TKR systems, this notch is used to further constrain the motion of the tibia on the femur.

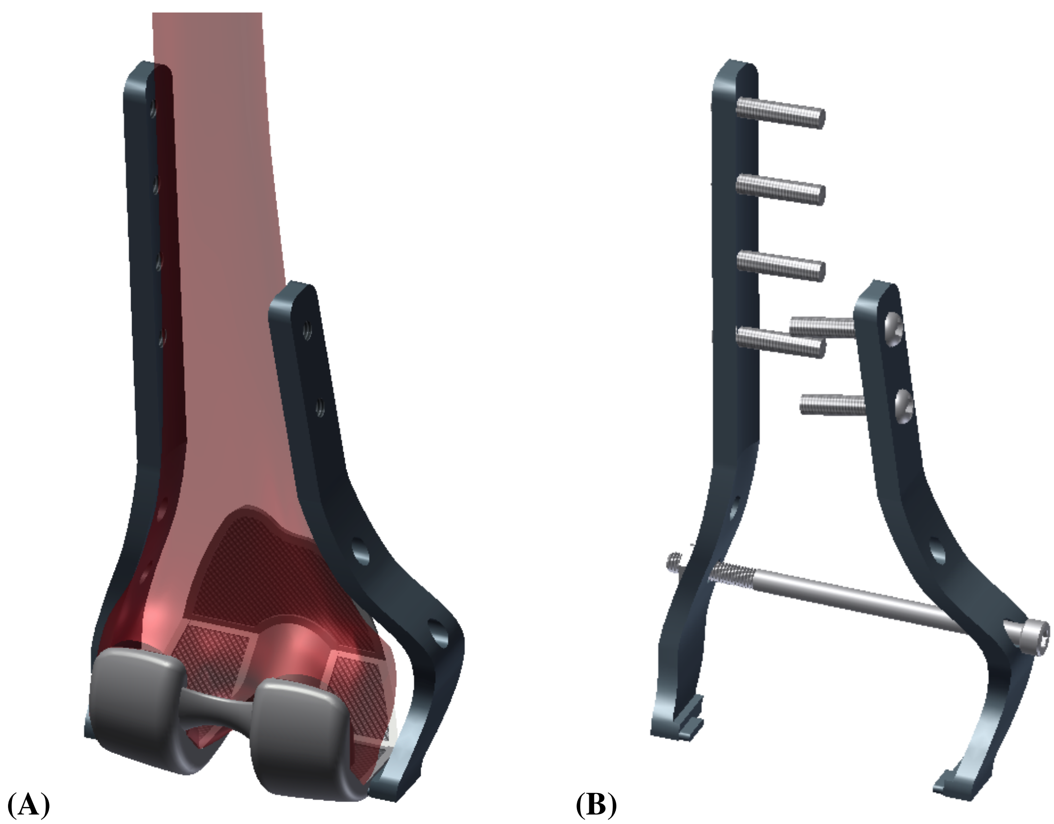

Figure 2.9: **Medial and lateral plates simplified for manufacturability.**
(A) The final plate geometry. The initial contours of the medial and lateral plates (Figure 2.7) were simplified for manufacturability. **(B)** The completed design of the construct showing the plates, the transverse compression screw and the proximal locking screws.

around the collateral ligaments. However, these modifications were accepted since the plates were meant to only serve as a proof-of-concept.

2.2.2 Surgical Procedure: Placement of the Compression Screw

One of the challenges in treating a fracture with the proposed construct is ensuring proper placement of the transverse compression screw. Its placement is governed by the clearance hole that must be drilled into the distal bone prior to fixation. The wrong location or trajectory of the hole can lead to misalignment of the plates and the prosthesis with respect to the bone.

To address this challenge, a custom drill guide was designed and manufactured to assist in the drilling of a clearance hole into which the compression screw is inserted (Figure 2.10). Similarly to the medial and lateral plates, the guide has tabs that insert into the slots on the prosthesis. A screw is tightened causing the guide to clamp onto the prosthesis. An extension arm attached to the guide has holes where a drill sleeve can be inserted that guides the location and trajectory of the hole. For the current application, the guide was created to be compatible with an existing drill sleeve (Percutaneous drill sleeve neutral [702958]; Stryker Orthopaedics, Mahwah, NJ). Using a standard surgical drill, Kirschner-wire (K-wire) and cannulated drill bit, the clearance hole can then be created as outlined in Appendix B. Engineering drawings of the drill guide can be found in Appendix C.

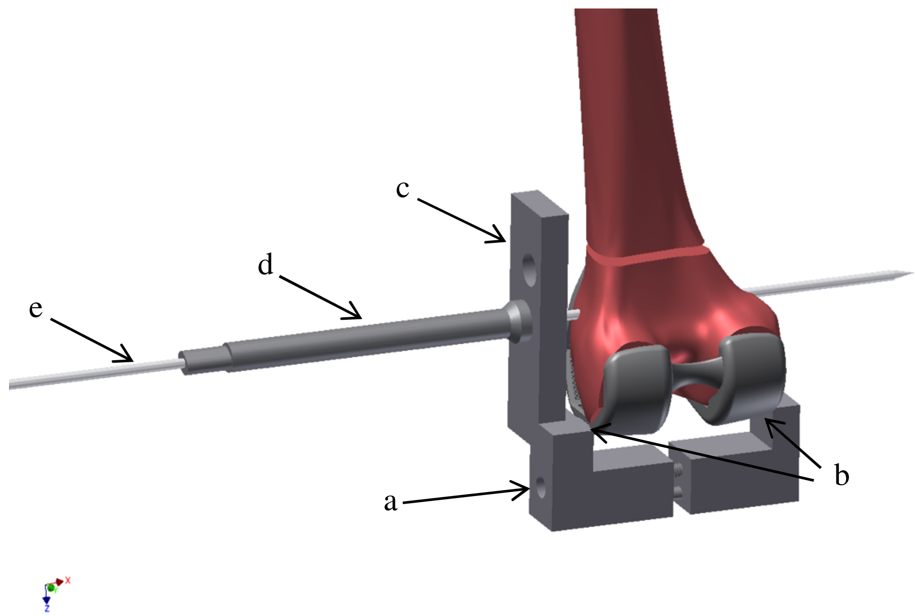

Figure 2.10: Custom drill guide used to create the compression screw hole. Drill guide used for placement of the clearance hole for the transverse compression screw. By tightening a screw (a) the guide clamps directly to the prosthesis via tabs (b) that insert into the pre-existing slots on the prosthesis. An extension arm (c) is mounted onto the guide with holes for inserting a drill sleeve (d). The drill sleeve provides the surgeon with the exact placement and orientation of the hole. A K-wire (e) drilled directly through the distal femur marks the spot for the transverse compression screw.

2.3 MANUFACTURING

The plates were manufactured from a section of 1.5” x 2.5” x 14” 316-stainless steel. This material was chosen based on its availability and similarity to other orthopaedic implants. A 5-axis water jet cutter (Paser 3; Flow International Corporation, Kent, WA) was used to cut out the initial profile of the plates in the frontal view. They were then rotated 90° and the side profile was cut. CNC machining was then used to create a concave underside to the plates, drill the holes and finish the tabs to the appropriate size. As a final step, the holes for the proximal locking screws on both plates were tapped. The manufactured plates are shown applied to a synthetic femur in Figure 2.11.

The drill guide (Figure 2.12) was manufactured from an aluminum block using a milling machine. Following the surgical procedure outlined in Appendix B, the guide was used to create the clearance hole in a synthetic femur (Figure 2.13).

2.4 DISCUSSION

Medial and lateral fixation plates were designed for treating periprosthetic fractures of the distal femur. Taking into consideration the femoral anatomy including the origins for the collateral ligaments, the plates are designed to enhance fixation by attaching directly to the prosthesis. This novel approach was used to avoid complications that can arise from attaching to the bone in a patient with a comminuted fracture or poor distal bone quality.

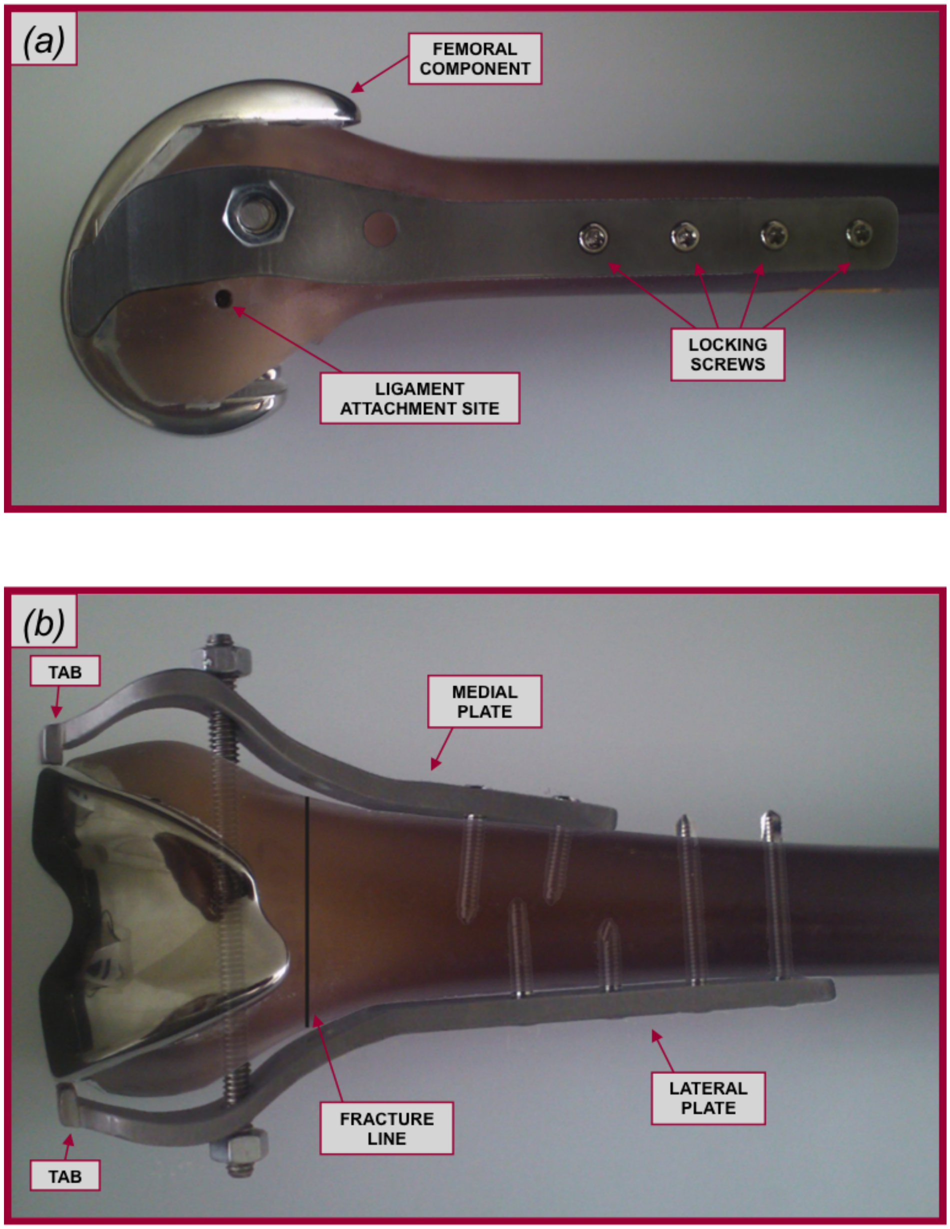

Figure 2.11: **Medial and lateral plates implanted on a synthetic femur.**
The complete double plated construct used to treat a periprosthetic fracture on a synthetic femur. The various components of the construct are labelled on the lateral **(A)** and anterior **(B)** views.

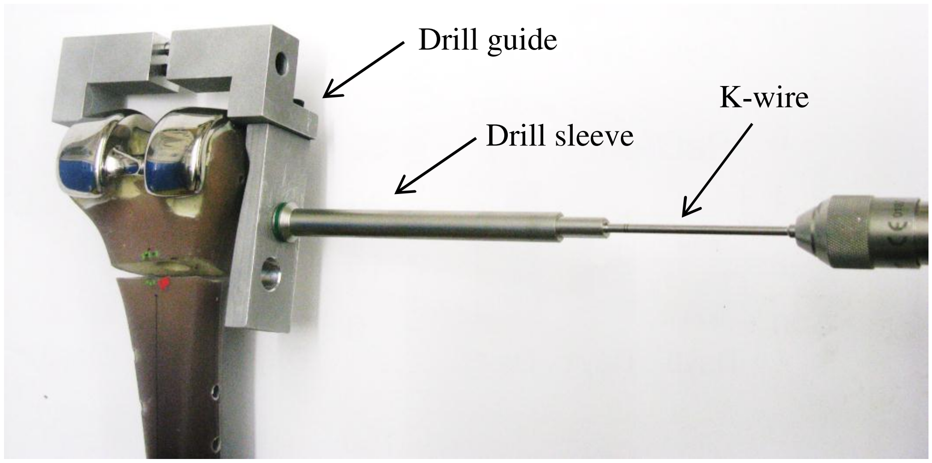

Figure 2.12: **Manufactured drill guide used for creating the clearance hole.** The drill guide is shown clamped to the femoral prosthesis. A K-wire is being drilled into the distal bone using a surgical drill.

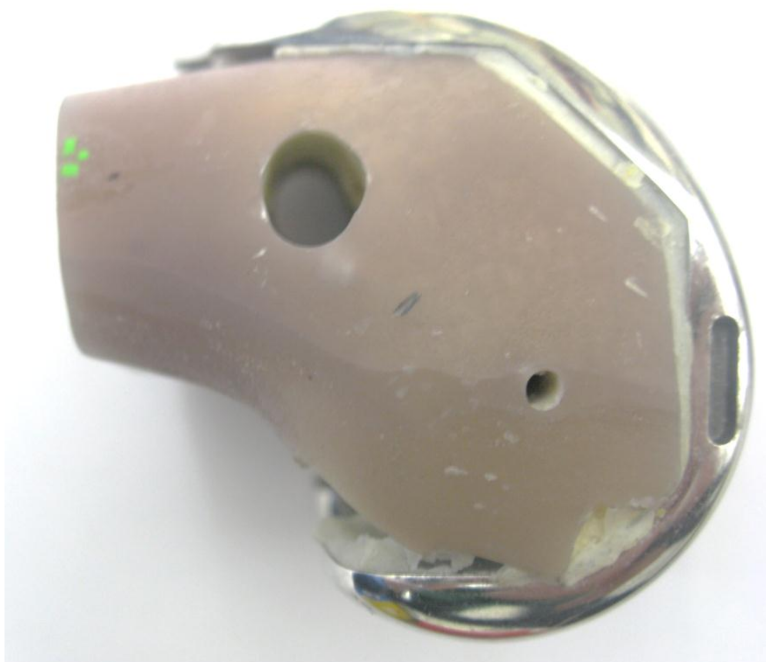

Figure 2.13: **Clearance hole created for the transverse compression screw.** The clearance hole for the compression screw created using the drill guide.

Several simplifications had to be made to the initial plate design to allow for manufacturing using a 5-axis water jet cutter and a CNC machine. These changes resulted in gaps between the plates and the femur, primarily around the ligament attachment points (Figure 2.12). The use of direct metal laser sintering (DMLS) or another additive material process in future design iterations would allow for the plate geometry to better match that of the femur. This would reduce the overall width of the construct and cause less disruption for the patient.

The designed plates were successfully able to avoid the ligament attachment sites based on the location and size reported in literature (Otake et al., 2007). However, it is difficult to know if the full function of the ligament will be preserved after the plates have been implanted. The distal portion of the proposed lateral plate is thinner than that of a traditional single lateral plate so it is unlikely to cause increased disruption of the vasculature. The impact of the medial plate on vasculature and nerves should be investigated in future studies. It is also important to note that the present design is for a single size and geometry of femur. Future designs should involve multiple sized plates to account for the variation in the shape of femurs.

Future design iterations should also consider the inclusion of additional screw holes on the distal aspect of the lateral plate. Current lateral plates can have upwards of eight holes in the distal portion to give the surgeon multiple options for stabilizing the distal bone. In the case of the proposed double plate construct, these holes would help to further suppress rotation of the distal fragment of bone and interfragmentary motion while allowing increased surgeon flexibility. Moving the transverse compression screw holes posteriorly to align them better with the tabs would lead to better a clamping force on the prosthesis. This would potentially reduce fracture motion, however; it could also lead to intrusion on the ligament attachment sites. Therefore, the benefits and impacts of these changes should be assessed through additional testing. A conceptual drawing for a possible second iteration plate design is shown in Figure 2.14.

Figure 2.14: Conceptual design for second iteration medial and lateral plates. Conceptual medial and lateral plates are shown with geometry to better match the contours of the femur. The distal aspect of the lateral plate was also made larger to accommodate additional locking screws.

CHAPTER 3: EXPERIMENTAL TESTING

3.1 INTRODUCTION

Periprosthetic fractures of the distal femur occur in 0.6 – 2.5% of patients with total knee replacements (Zehntner & Ganz, 1993). Current surgical treatment methods for these types of fractures include various types of plating and screw constructs as well as intramedullary nails. No single method has been found to be effective for treating the many types of periprosthetic fractures seen clinically. Complications stemming from these current surgical options include nonunion (9%), fixation failure (4%), infection (3%), and revision surgery (13%) (Herrera et al., 2008).

Previous biomechanical studies have sought to determine the optimal fixation method for distal femur fractures. The majority of these studies compare the fracture motion observed among two or three different treatment methods using synthetic or cadaveric femurs (Bong et al., 2002; Duffy et al., 2006; Higgins et al., 2007; Otto et al., 2009; Salas et al., 2011a). Devices such as condylar blade plates, distal femoral locking plates, dynamic condylar screws and intramedullary nails have all been previously tested. Few of these studies have looked at how the inclusion of a femoral prosthesis would affect the performance of the device, or if a better alternative exists that is capable of improving the fracture stabilization.

One option is to take advantage of the rigidity of the femoral prosthesis to enhance the stability of the fracture. Small slots are located on the medial and lateral sides of several commercially available prostheses. These could potentially serve as attachment points for a plating system. Therefore, two plates (medial and lateral) were envisioned attaching to the prosthesis to further improve stability of distal femoral fractures. The purpose of this study was to evaluate this novel bilateral plating technique to determine if it increases stabilization and maintains overall alignment of a femoral prosthesis with respect to the femur.

3.2 MATERIALS AND METHODS

A biomechanical comparison to a current surgical treatment option was conducted to evaluate the mechanical stability of the bilateral plate-prosthesis construct. Custom medial and lateral femoral plates were designed and manufactured (Chapter 2). The plates and prosthesis were then attached to a synthetic femur and the construct was loaded in compression and bending. The relative motion across a simulated fracture was measured using two different techniques: 1) a two-dimensional method that used a high-resolution microscope camera, and 2) a three-dimensional motion capture technique. The following sections describe the sample preparation, experimental setup / protocol and the technique used to track the fracture motion for each of the two constructs.

3.2.1 2D Fracture Motion Tracking

3.2.1.1 Sample Preparation

Three medium left 4th generation synthetic femurs (Sawbones; Pacific Research Laboratories, Vashon, WA) were implanted with the femoral component of a Scorpio total knee replacement system (Scorpio 7L PS [71-4507L]; Stryker Orthopaedics, Mahwah, NJ). An experienced orthopaedic surgeon implanted the prostheses using the instruments and technique recommended by Stryker. The proximal end of the implanted femur was cut off 40 mm distal to the lesser trochanter. The cut end of the femur was then potted in a section of aluminum tubing (OD = 1-5/8"; THK = 1/8") using dental cement (Denstone®; Heraeus Kulzer, South Bend, IN). The Denstone® filled approximately 105 mm of the tubing so that 230 mm of the distal portion of the femur remained exposed. The femurs were potted in the cylinder so that the long axis of the bone was aligned with the cylindrical axis of the tubing. A 3 mm transverse osteotomy was created in the distal femur 5 mm proximal to the anterior aspect of the prosthesis (Figure 3.1). Orientation of the osteotomy was not strictly controlled but was intended to be approximately perpendicular to the long axis of the bone.

A custom drill guide clamp (Section 2.3.2) was used to create the clearance hole for the transverse compression screw through the metaphyseal region of the distal femur. The tabs of the guide were inserted into the slots on the prosthesis and were clamped in place by tightening a socket head cap screw. Using the guide, a Kirschner wire was drilled into distal at the correct location. A cannulated drill bit was then used to create the 10 mm clearance hole. Figure 3.1 shows the implanted femur, the 3 mm wide simulated transverse fracture, and the clearance hole for the transverse compression screw.

The prepared femurs were treated with one of three fixation methods: 1) a single lateral femoral locking plate (AxSOS distal lateral femur locking plate [437510]; Stryker Orthopaedics, Mahwah, NJ) (Figure 3.2a); 2) the proposed bilateral locking plates with no distal locking screws (Figure 3.2b); or 3) the bilateral locking plates with two additional distal locking screws (Figure 3.2c). An experienced orthopaedic surgeon

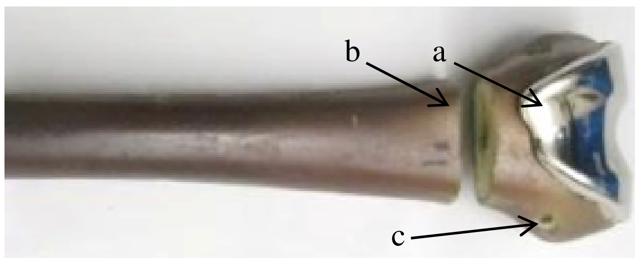

Figure 3.1: **Implanted femur.**
4th generation synthetic femur implanted with *[a]* the femoral component, *[b]* the simulated 3 mm wide transverse periprosthetic fracture and *[c]* the clearance hole for the distal transverse compression screw.

(A)

(B)

(C)

Figure 3.2: **Fixed femurs.**
The samples are shown fixed with one of three options: **(A)** distal lateral femoral locking plate, **(B)** proposed bilateral locking plates and no distal locking screws, or **(C)** proposed bilateral locking plates and two distal locking screws.

performed each of the three treatment procedures using standard tools and techniques. Screw length and type for each of the three treatments are detailed in Appendix D.

3.2.1.2 Experimental Setup and Protocol

Loads were applied to the fixed femurs using a materials testing machine (eXpert 5601; ADMET, Norwood, MA) (Figure 3.3). The loads were applied to the prosthesis via a tibial tray ([7376-0007]; Stryker Orthopaedics, Mahwah, NJ) and polyethylene insert ([72-13-0708]; Stryker Orthopaedics, Mahwah, NJ) that matched the femoral component to simulate a complete total knee replacement (TKR) system.

The aluminum tubes holding the potted bone samples were inserted into a custom holder that secured them for loading in either compression (Figure 3.3a) or bending (Figure 3.3b). A detailed description of the setup protocols for both compression and bending can be found in Appendices E and F.

Compression testing was performed to simulate loading of the knee during full extension whereas bending simulated loading during 90° of flexion. The loading protocol was chosen to be similar to those reported in similar research (Bong et al., 2002; Otto et al., 2009; Salas et al., 2011a), and is summarized in Table 3.1.

Each sample was tested four times in each of the compression and bending load configurations. Pre-conditioning was performed on the samples prior to each test in an effort to minimize creep and to ‘warm-up’ the construct. After initial preliminary testing, it was found that the stress relaxation in the construct was greatest during the compression tests. This stress relaxation made it difficult to maintain the constant load that was

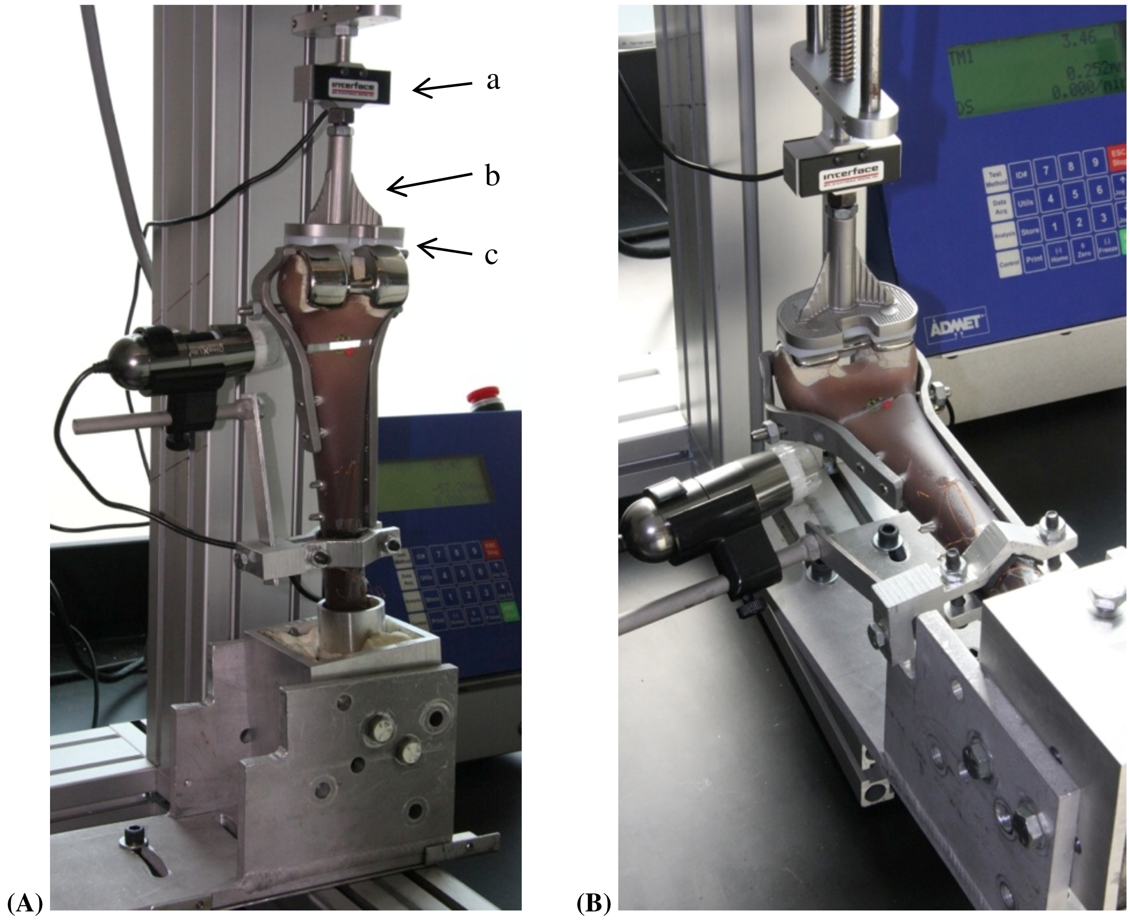

Figure 3.3: **Test setup.**
ADMET materials testing machine used to apply **(A)** compression loads, and **(B)** bending loads directly to the sample. Loads were measured using a *[a]* 300-lbf load cell (SML-300; Interface Inc., Scottsdale, AZ) and transmitted using a matching *[b]* tibial tray and *[c]* polyethylene insert.

Table 3.1: **Loading protocol for 2D testing.**
The parameters used for pre-conditioning, compression and bending during 2D testing are shown.

	Pre-conditioning	**Compression**	**Bending**
Load (N)	0 → 500 → 0	50, 100 → 600 → 100, 50	0 → 500 → 0
Rate (mm/min)	25	1 (100 N steps)	10 (100 N steps)
Duration (cycles)	5	1	1

required to capture fracture motion data. Therefore, the compression loading was started at 50 N to better preserve the effects of the pre-conditioning and reduce the stress relaxation. Repeatability of the system was assessed by testing the "bilateral plated sample without distal screws" (Figure 3.2b) ten times in each configuration.

3.2.1.3 Fracture Motion Tracking

The objective of the mechanical testing was to determine the amount of relative fracture motion between fragments for a given treatment method. Since relative motions were expected to be on the order of tenths of millimeters, a unique measurement system had to be developed. A digital microscope (DinoLite AM413MT; AnMo Electronics Corp, Taiwan) capable of capturing images at 10x-70x magnification with a resolution of 10-12 µm/pixel at roughly 30x was used. A custom clamp was designed to attach the DinoLite directly to the proximal aspect of the sample. The clamp enabled adjustment in five degrees of freedom so that optimal camera placement could be achieved. Since the clamp was attached directly to the femur, the camera would move with the bone as the bone flexed under applied loads. This kept the camera focused on the fracture site regardless of the overall displacement of the femur.

In order to quantify the relative motion of the fragments, the DinoLite was positioned to focus on one of two perpendicular aspects of the bone: posterior (Figure 3.4a) or medial (Figure 3.4b). The combination of these two views allowed for motion characterization in both the coronal (posterior view) and sagittal (medial view) planes.

(A) (B)

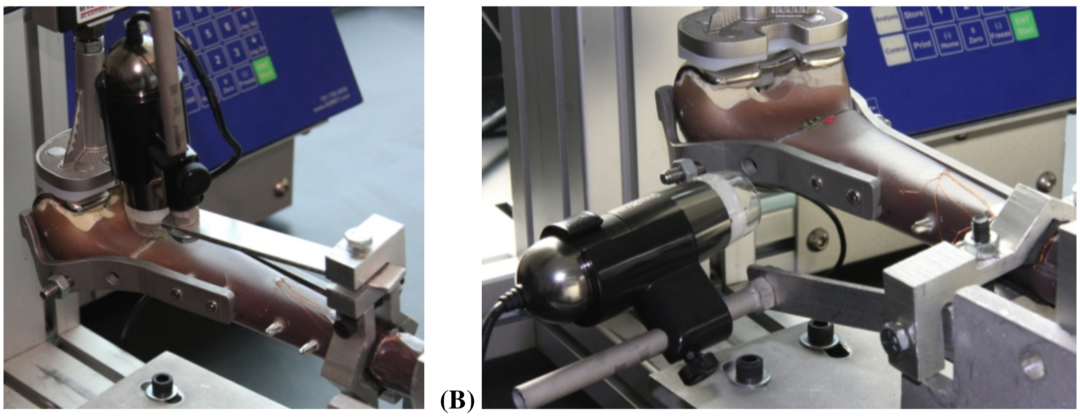

Figure 3.4: 2D motion capture with DinoLite microscope.
(A) DinoLite microscope camera focused on the posterior aspect of the femur to view fracture motion in the coronal plane. **(B)** DinoLite camera focused on the medial aspect of the femur to view fracture motion in the sagittal plane.

The DinoLite was calibrated before each test by placing a 1 mm high precision gauge block in the camera's field of view. After focusing, an image of the block was captured. A custom-written LabVIEW® (National Instruments, Austin, TX) program used edge detection to identify the opposing edges of the block. The program then calculated the perpendicular distance between the edges in pixels. The gauge block length (1 mm) was then divided by the number of pixels to obtain a test-specific resolution in μm/pixel.

Three small rectangular pieces of fluorescent green tape (approximately 1 mm x 1 mm size) were glued directly to each of the proximal and distal fragments in the posterior and medial views (Figure 3.5). The positions of these markers were captured as images by the DinoLite at each 100 N increment during loading and unloading using LabVIEW®. Figure 3.6 shows a 50 N image with a 600 N image overlaid to demonstrate the typical displacement observed during a compression test.

The sequence of images was imported into LabVIEW® and a colour thresholding operation was performed to identify the green markers by manually adjusting the permitted RGB values until only the markers remained (Figure 3.7). A number of additional operations (remove border objects, fill small holes and remove small objects) were performed automatically by the program to improve the marker shape within the image. The locations of the centroids of these markers (X,Y) were then calculated and the positions were written to a .txt file for each image in the sequence.

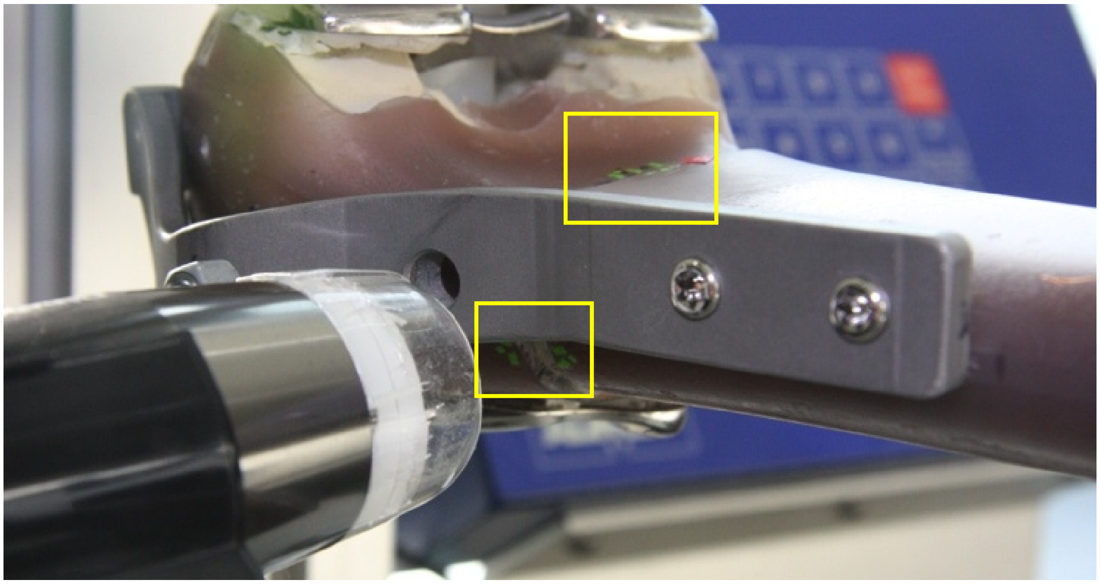

Figure 3.5: **Fluorescent green tracking markers.**
Green markers on the posterior and medial aspects of the bone were used to track the relative displacement of the fracture site during loading.

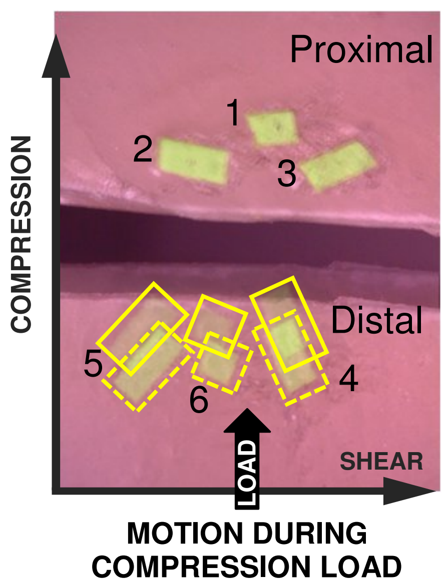

Figure 3.6: **2D marker motion.**
Two images overlaid showing the typical maximum displacement between proximal and distal fragments during a 600 N compression test. The green markers labeled 1-6 are shown. The dashed boxes highlight the initial positions of markers 4, 5 and 6 (at a 50 N load) while the solid boxes highlight their final positions at 600 N.

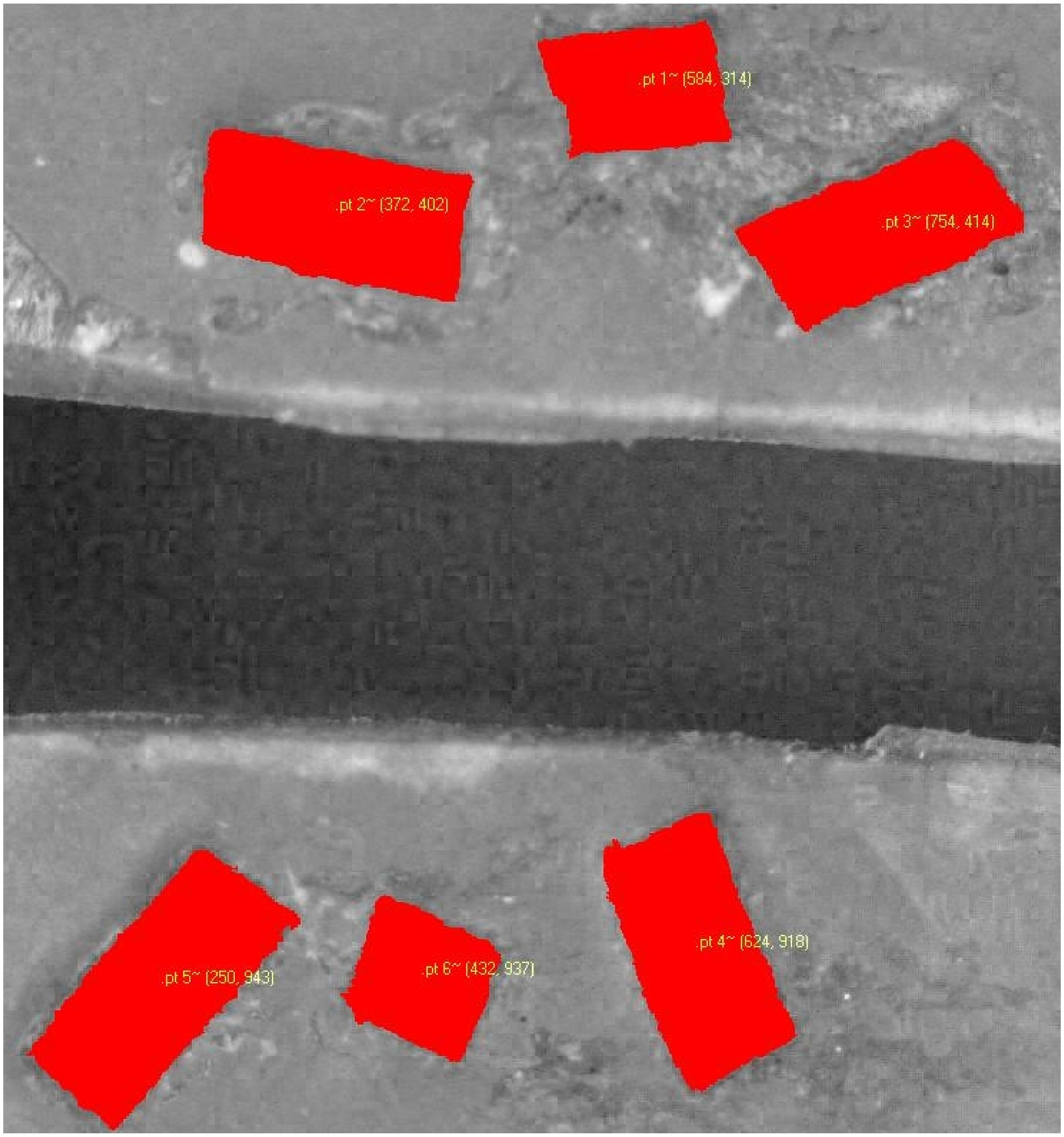

Figure 3.7: Colour thresholding of 2D image.
A sample image after the colour threshold operation was performed to identify markers and the centroid locations (shown in green text). Adjustment of the RGB values was performed for each sequence of images to highlight only the green markers. The RGB values used in the thresholding operation can be found in the output file from each test.

To better interpret the results the total motion was decomposed and transformed into three degrees of freedom within the image plane: 1) compression (along the long axis of the bone), 2) shear (90° to the compression), and 3) rotation about the axis normal to the compression and shear axes (Figure 3.8). To perform this transformation, the rotation between the desired motion coordinate system and marker coordinate system had to be calculated.

First, a line was drawn on the sample representing the load axis using a laser level and a custom wooden jig. The line was located close to the proximal posterior and medial markers for each sample. An image capturing the line and the markers was then imported into a custom-written LabVIEW® program (for the bilateral construct the medial plate was removed to allow better visualization). This program determined the orientation of the centroid axis and the load axis in terms of pixel coordinates of the image (as labelled in Figure 3.9). The load axis angle was then shifted by the predetermined angle between the compression and load axes: 6° for the posterior view and 3° for the medial view (Figure 3.8). This step defined the compression axis in terms of the image coordinates. The shear axis was then defined by subtracting 90° from the compression axis. Finally, the angle between the shear and centroid axes resulted in the coordinate "adjustment angle" needed to decompose the captured motion into the desired bone coordinate system. A similar procedure was performed using the medial view image by defining the load, centroid, compression and shear axes. In total, two adjustment angles were determined for each sample tested.

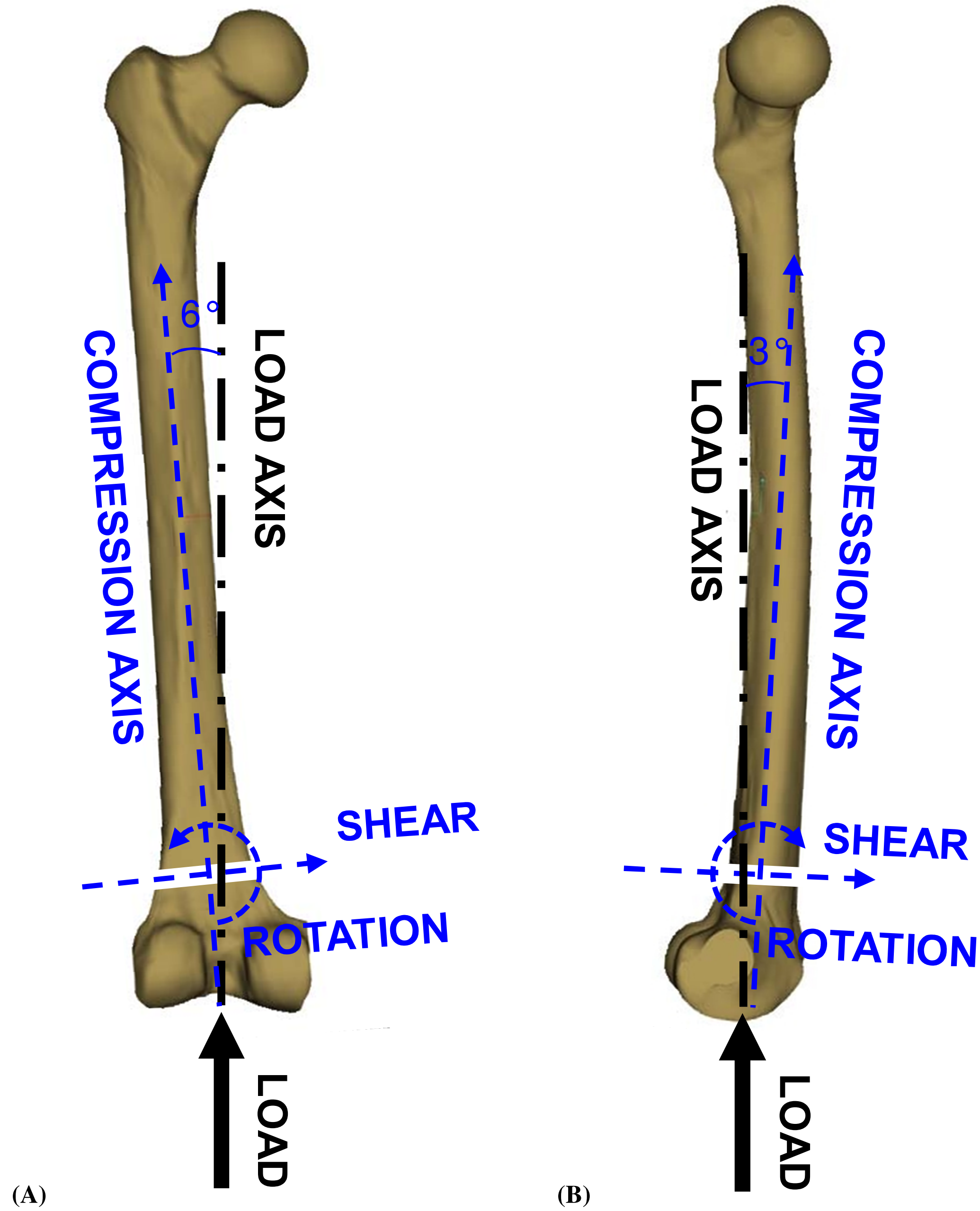

Figure 3.8: **Components of motion in posterior and medial views.**
Schematic showing the definitions of the three primary directions of motion (compression, shear and rotation) with respect to the load axis and fracture line in both views: **(A)** posterior and **(B)** medial. The compression axis was defined as parallel to the long-axis of the bone. The angle between the vertical load axis and the compression axis was measured (posterior = 6°; medial = 3°). The shear axis was defined as perpendicular to the compression axis. Rotation was defined about an axis normal to the compression and shear.

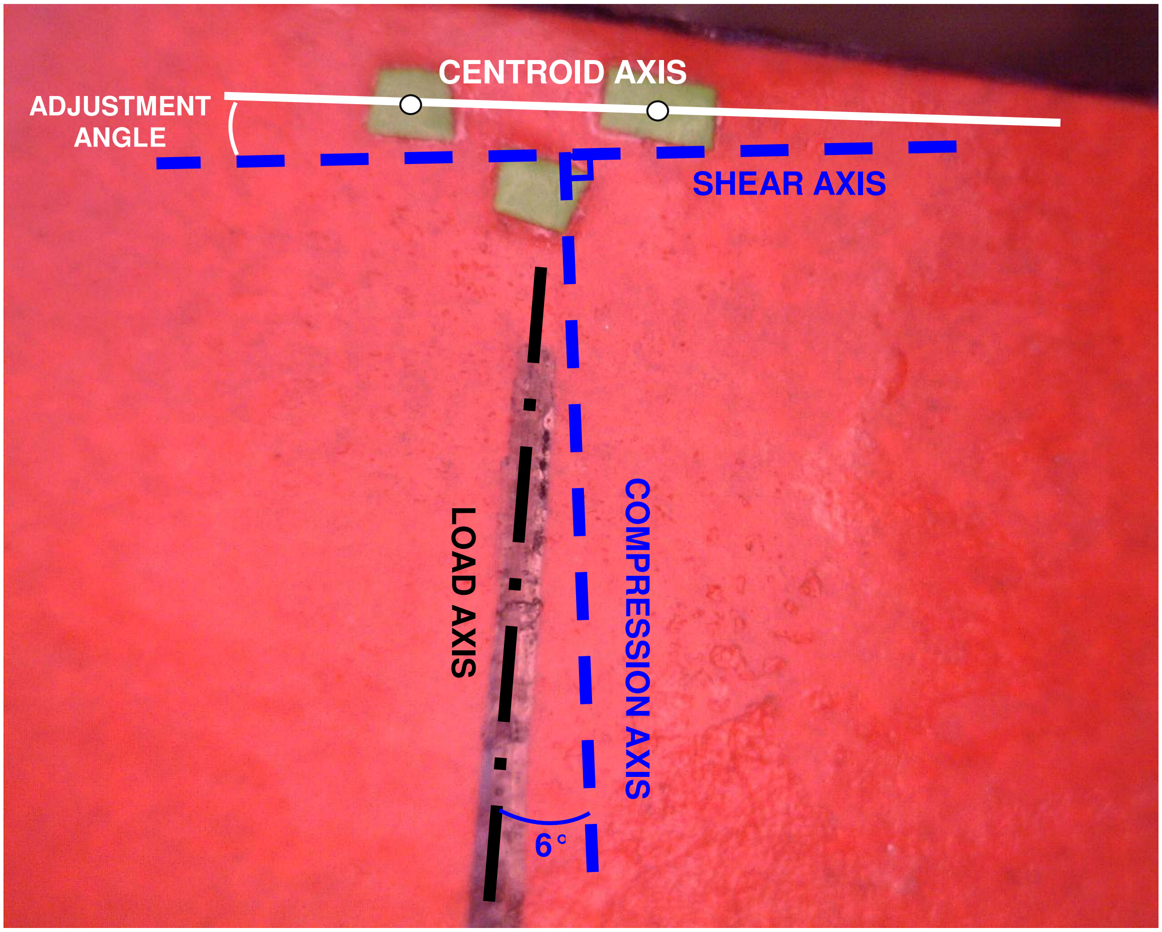

Figure 3.9: **Coordinate adjustment angle calculation.**
The method for calculating the "Adjustment Angle" is shown for the posterior view. The "Centroid Axis" was defined by a line connecting markers #2 and #3 (as labelled in Figure 3.6). The black marker line on the original image was used to define the "Load Axis". This axis was shifted by 6° (3° for the medial view) to define the "Compression Axis". The compression axis was rotated 90° to define the "Shear Axis". Finally, the angle between the "Shear Axis" and the "Centroid Axis" gave the "Adjustment Angle". A similar diagram can be used for the medial view.

The .txt files with the (X,Y) data from the colour thresholding and analysis LabVIEW® program were imported into Microsoft Excel for calculation of the fracture motion. For each image, marker #2 (Figure 3.6) was treated as the origin around which a local coordinate system was based. The coordinates of marker #2 were first subtracted from the other markers to simplify the procedure. Next, the rotation matrix:

$$\begin{bmatrix} x' \\ y' \end{bmatrix} = \begin{bmatrix} cos\theta & -sin\theta \\ sin\theta & cos\theta \end{bmatrix} \begin{bmatrix} x \\ y \end{bmatrix} \qquad \textbf{Eq. 3.1)}$$

was used to alter the coordinates for each marker by the previously calculated “adjustment angle”. This aligned the X- and Y-axes of the marker coordinates with the desired compression and shear motion axes. This process was repeated for each image in the loading sequence.

The changes in location of markers #2-5 were calculated by subtracting the (X,Y) coordinates of each loaded image from the initial unloaded image. The average of the (X,Y) change in location of markers #4 and #5 (distal) was subtracted from the average of markers #2 and #3 (proximal). The resultant X value gave the displacement in shear and the Y value gave the displacement in compression (relative to the original unloaded sample).

The angle of rotation normal to the compression and shear axes was calculated by finding the angle between a line connecting markers #2 and #3 and one connecting markers #4 and #5. The angle between these two lines in each image was subtracted from the angle in the initial image to find the relative rotation between the proximal and distal fragments.

3.2.2 3D Fracture Motion Tracking

Relying on a set of 2D images to characterize fracture motion has several limitations. It is difficult to combine the results from two views into a single vector since motion is measured at two different locations on the bone as opposed to capturing both views at one specific site. In the case of using a single camera it also assumes that there is a high level of repeatability between tests since medial and posterior views had to be captured separately. Therefore, to better calculate the global fracture motion that occurred during testing, 3D motion analysis was used.

3.2.2.1 Sample Preparation

Six medium left synthetic femurs (Sawbones; Pacific Research Laboratories, Vashon, WA) were used in this second stage of testing. Three of these femurs were implanted with the single lateral locking plate while the remaining three were treated with the bilateral prototype plates and two distal locking screws. All three samples from the 2D testing were re-used for this stage, with two distal screws being added to the sample originally without any. Sample preparation was performed in the same manner as described for the 2D testing (Section 3.2.1.1).

3.2.2.2 Experimental Setup and Protocol

The experimental setup used for the 3D testing was very similar to that described for 2D testing, with a few differences in loading protocol and number of tests performed on each sample. The loading parameters are shown in Table 3.2. During load cycling,

Table 3.2: Loading protocol for 3D testing.
The parameters used for pre-conditioning, compression and bending during 3D testing are shown.

	Pre-conditioning	**Compression**	**Bending**
Load (N)	25 → 250 → 25	25 → 500 → 25	25 → 250 → 25
Rate (mm/min)	*Compression*: 10 *Bending*: 25	5	25
Duration (cycles)	5	5	5

achieving a consistent position at 0 N load was found to be difficult. To reduce the error among tests and to better preserve pre-conditioning effects the minimum load was increased from 0 N to 25 N. Maximum bending loads were decreased to 250 N to protect the samples from accumulated damage. Since it was not necessary to hold the load at each step for image capturing during the 3D testing, increased load rates and additional cycles per test were permitted. Each of the six samples were tested three times in cyclic compression followed by three times in cyclic bending for a total of 36 tests.

3.2.2.3 Fracture Motion Tracking

3D motion analysis systems are commonly used for gait analysis and other larger-scale biomechanical applications. Multiple infrared cameras situated around the region of interest track reflective markers affixed to a moving object or person. Motion analysis software (Cortex v.1.1.4.368; Motion Analysis, Santa Rosa, CA) then uses the data from the cameras to calculate the locations of the markers over a specified duration of time.

Six 1.5 mm diameter reflective markers (B&L Engineering, Santa Ana, CA) were attached to the samples, with three on each of the bone segments (Figure 3.10). The markers on the proximal segment were glued directly to the bone surface using cyanoacrylate. A laser level was used to draw a line along the long axis of the bone and a square edge was used to create a line perpendicular to this ‘long axis’ line. One marker was placed at the intersection of the lines, and the other two markers were placed 15 mm proximal on the ‘long axis’ line and 10 mm medial on the ‘transverse’ line, respectively (Figure 3.11a). These markers were used to define the axes for the local coordinate system of the bone (Figure 3.11b). The remaining three markers were glued to a

(A)  **(B)** 

Figure 3.10: **Experimental setup with reflective markers.**
Experimental setup showing the 6 reflective markers (within the highlighted yellow box) on the proximal and distal fragments in **(A)** compression and **(B)** bending.

(A)  **(B)** 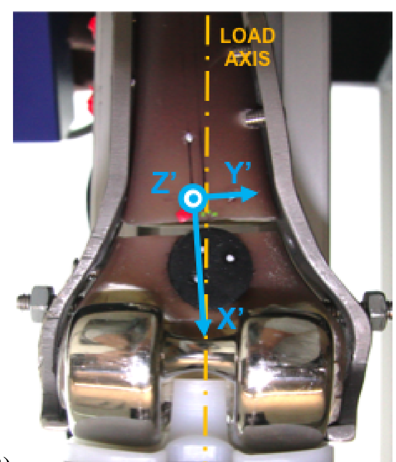

Figure 3.11: **Marker orientation and local coordinate system.**
(A) Magnified view of the reflective marker layout and **(B)** superimposed local coordinate system in relation to the load axis.

removable piece of Velcro® in a triangular configuration and attached to the distal fragment. This allowed the same distal markers to be reused for all the samples.

Four cameras (Raptor-4; Motion Analysis, Santa Rosa, CA) were situated around the ADMET mechanical test system (Figure 3.12). The focal length on each camera was set to 55 mm and focused using the camera focus card provided by the manufacturer. Calibration was a two-step process and performed according to manufacturer's instructions. First a 60x90 mm L-frame calibration unit (850-1774-001; Motion Analysis, Santa Rosa, CA) was used to specify the global coordinate system. Then one of the markers on the L-frame was removed to simulate a calibration wand with three collinear markers. The wand was used to determine the exact positions of the cameras relative to the 50 cm x 50 cm x 50 cm volume of interest.

Each sample was placed in the mechanical test system and the threshold and brightness levels for each camera were adjusted so that each marker was visible. Finally, a masking tool within the Cortex software was used to eliminate interference from any signals other than those of the markers. A section of dark fabric was also used to cover the reflective components of the test system. Mechanical loading was then performed on each of the samples according to the protocol outlined in Section 3.2.2.2.

Data were collected from the cameras at a rate of 60-Hz for the duration of the five cycles. This resulted in X,Y,Z coordinates for each marker within the global "lab" coordinate system, to which a 1-Hz Butterworth filter was applied to reduce noise. Any extraneous spikes in the data (representing 'jumping' around of the marker location) were

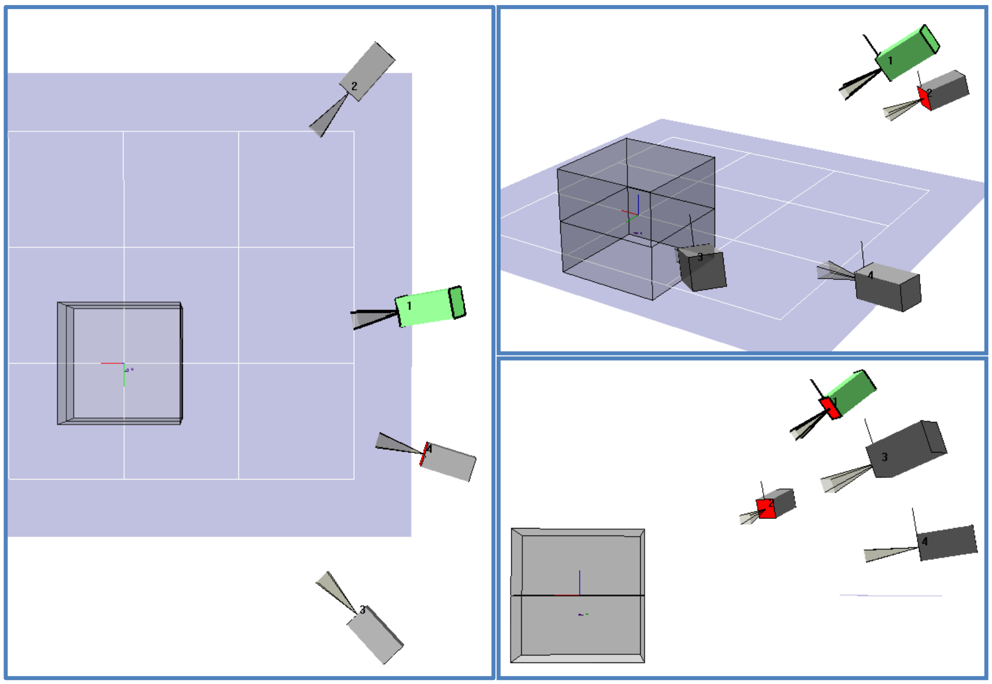

Figure 3.12: Infrared camera placement for 3D motion capture.
The placement of the 4 infrared cameras are shown with respect to the volume of interest (shaded grey). 3 views are displayed: **(A)** top, **(B)** side and **(C)** isometric. [Layout obtained from Cortex software]

smoothed using the 'cubic join' function within Cortex. Each marker was then labeled based on their location (Figure 3.13a) and the data exported as a .trc file.

To transform the global X, Y, Z data into the local X', Y', Z' coordinate system of the femur (Figure 3.13b), the axis X' was first defined as the vector connecting P2 to P1 (Figure 3.13a). The cross product of X' and vector P1-P3 was used to create axis Z'. Finally, the cross product of Z' and X' defined axis Y'. The projections of each of these local coordinate vectors onto the global coordinate system were divided by their unit lengths to obtain a rotation matrix, $R^0{}_1$ (rotation matrix from the global to local system for the femur). The translational distance between the origin of the local proximal system and the distal system for the femoral condyle fragment ("p^1", Figure 3.14) was then calculated using the equation accompanying Figure 3.14 (Sirouspour, 2012). The change in this vector length with increased load was then calculated to obtain the relative fracture motion in 3D coordinates relative to the proximal coordinate system for the femur.

3.2.3 Analysis Technique

3.2.3.1 Statistical Analysis

The results from the 3D motion testing for the single plate and the double plated construct were compared using a Single Factor ANOVA (α=0.05). Due to the small sample size (N=2), statistical analysis could not be performed on the 2D data.

3.2.3.2 Clinical Relevance

Optimal secondary fracture healing is thought to occur when total fracture motion is within 2-10% of the total fracture gap size (Egol et al., 2004) (detailed explanation in Section 1.1.2). Therefore, by dividing the observed translational motion (2D analysis:

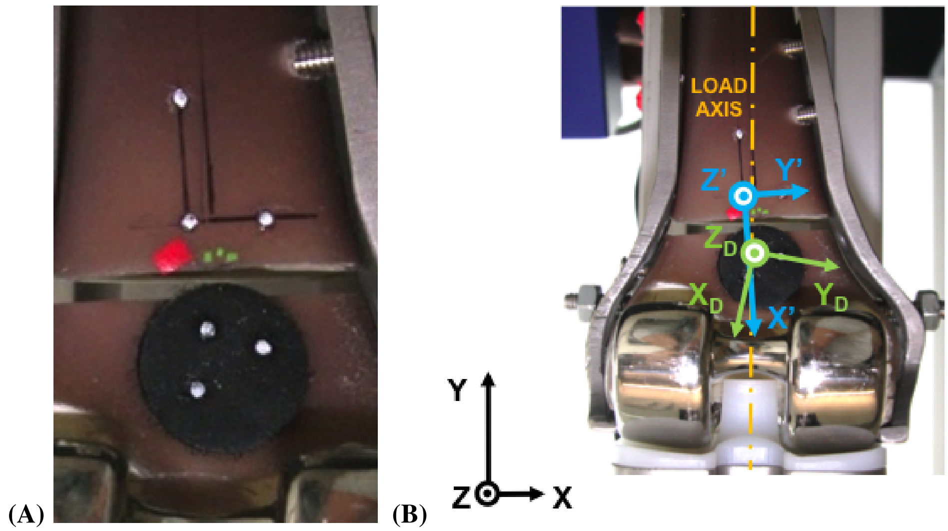

Figure 3.13: **Labelled markers and coordinate systems.**
(A) Magnified view of marker configuration showing labels, and **(B)** the coordinate systems used during analysis: Global: X,Y,Z; Local: X',Y',Z'; Distal: X_D,Y_D,Z_D.

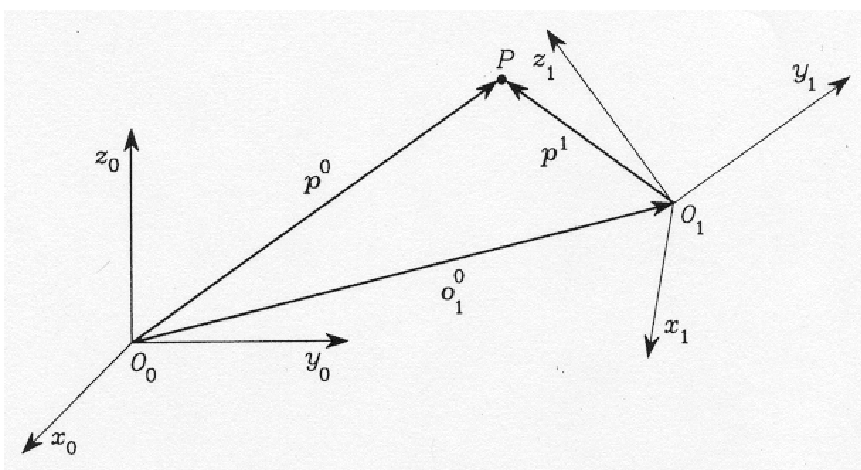

Figure 3.14: **Transformation from global to local motion (Sirouspour, 2012).**
"p^1" in the equation provides the coordinates of point "P" with respect to frame O_1 expressed in O_1. Here, system O_0 represents the global coordinate system; system O_1 represents the local femur coordinate system (on the proximal portion of the femur); point "P" represents the origin of the distal coordinate system (the femoral condyles and prosthesis); $R^1{}_0$ represents rotation matrix from the local to the global systems and is the inverse of $R^0{}_1$ (described in Section 0).

$\sqrt{compression^2 + shear^2}$; 3D analysis: $\sqrt{x'^2 + y'^2 + z'^2}$) by 3 mm (size of the fracture gap) we can obtain a measure of clinical performance of the treatment method. Rotation was neglected in this calculation for simplicity and to allow comparison between 2D results and 3D results (which did not account for rotational motion).

3.2.3.3 3D Motion Capture Resolution

One anticipated issue with using the proposed 3D motion capture system was its ability to track displacements in the range of 0.06 mm to 0.3 mm (2-10% of the 3 mm fracture gap). To assess the level of noise and the resolution of system, an 8-second static test was performed using the same experimental set-up as the other 3D tests but with no load applied to the sample. The resolution of the system was defined as the peak-to-peak displacement throughout the static test.

3.3 RESULTS

3.3.1 2D Fracture Motion Tracking

Values of shear, compression (or extension) and rotation were calculated for each individual test at the maximum load (600 N for compression, 500 N for bending). These values were then averaged for each treatment method and the standard deviation across the average was calculated. A summary of the averages and standard deviations for each camera view are shown in Figure 3.15 and Figure 3.16.

For the compressive loading, all three of the components of motion were less with the double plated construct both without distal screws (DBL) and with distal screws (DBL2) when compared to the lateral plate (LAT). DBL2 had slightly greater shear

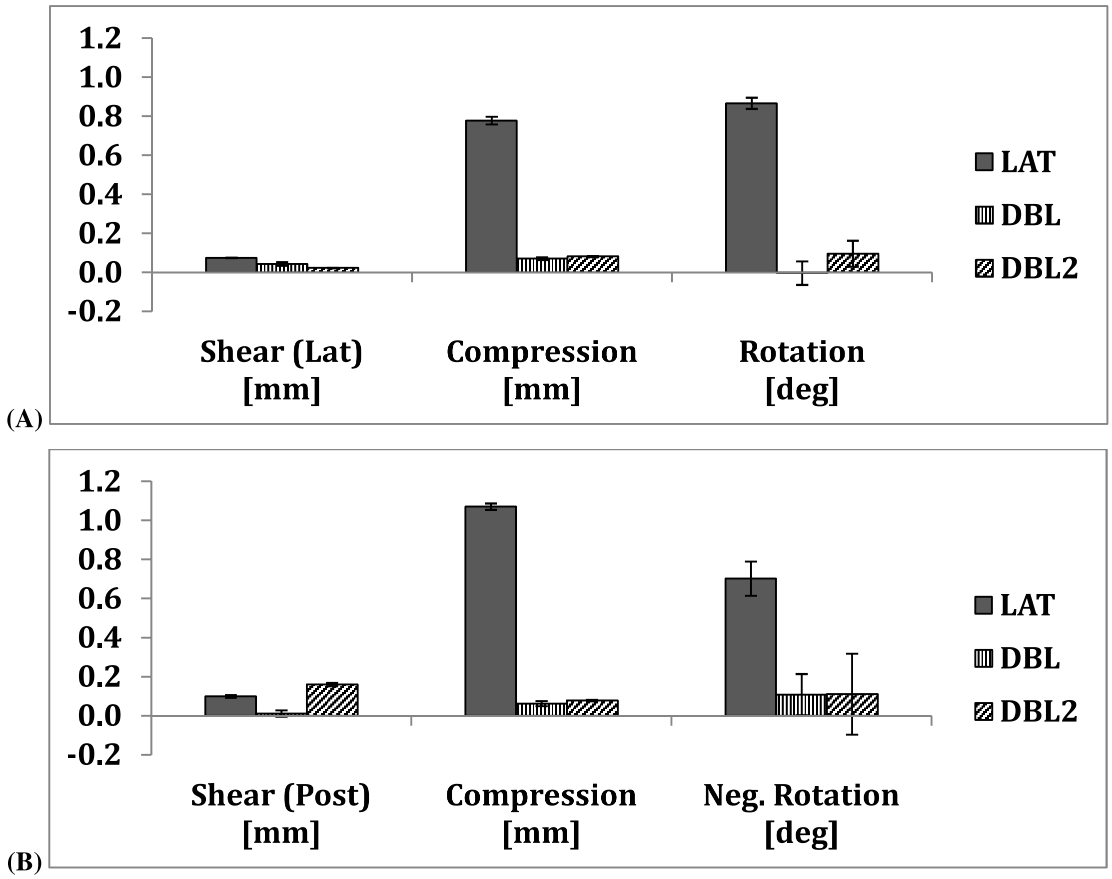

Figure 3.15: 2D compression test results (mean ± SD).
Comparison of the components of motion for compression tests between the lateral plate (LAT), double plated (DBL) and double plated with distal screws (DBL2): **(A)** Posterior view; **(B)** Medial view. Positive rotations are defined according to the direction shown in Figure 3.8.

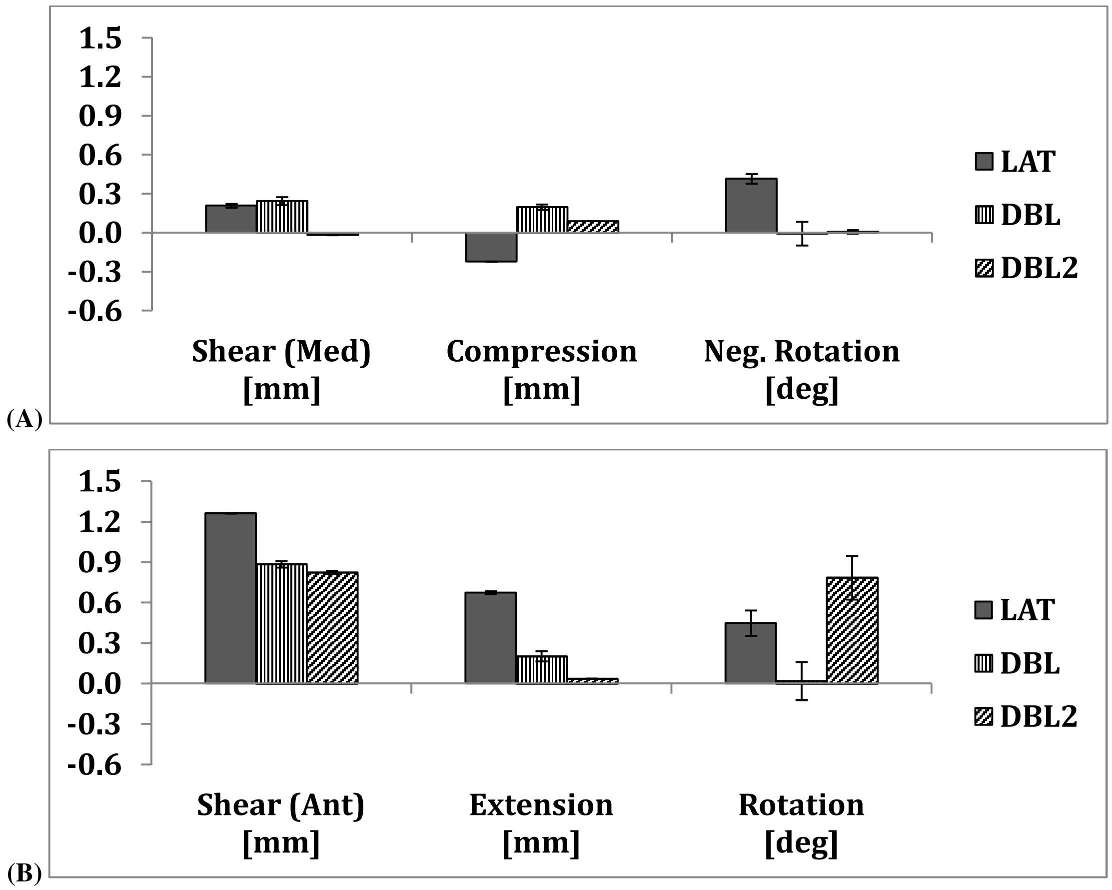

Figure 3.16: **2D bending test results (mean ± SD).**
Comparison of the components of motion for bending tests between the lateral plate (LAT), double plated (DBL) and double plated with distal screws (DBL2): **(A)** Posterior view; **(B)** Medial view. Positive rotations are defined according to the direction shown in Figure 3.8.

motion in the medial view compared to LAT (0.16 mm vs. 0.10 mm). Comparing DBL to DBL2 yielded similar results (<0.05 mm difference) for four of the six components measured during compressive loading. The other two components (rotation in the posterior view and shear in the medial view) had slightly larger motions for the DBL2 construct (0.1° and 0.15 mm, respectively).

Bending tests also resulted in less motion in most directions when comparing the double plated construct to the single lateral plate. The DBL2 construct showed less displacement in five of the six directions measured when compared to DBL. There was approximately a 0.8° increase in the rotational motion for the medial view between DBL2 and DBL. A summary table of 2D motion for each construct can be found in Appendix G.

Percent resultant fracture motion for each of the three constructs is shown in Table 3.3. These percentages were calculated by dividing the total translational motion by the fracture gap size (3 mm). The LAT construct allowed motion outside the desired 2-10% target range for each of the views with the posterior view of bending very close at 10.1%. However, since proper assessment of the results must consider both 2D views, the large motion observed in the medial view (44.1%) would likely raise the overall 3D motion well above the 10% threshold.

Improved percent fracture motion was demonstrated for each of the DBL and DBL2 samples, especially in the bending tests. Expected resultant 3D motion during bending for the DBL sample would likely still be well above 10% due to the large amount

Table 3.3: Percent fracture motion for 2D testing of LAT, DBL, and DBL2. Percent fracture motions are shown for each of the samples that underwent 2D testing. Percentages within the desired 2-10% threshold are coloured green while those outside are coloured red.

	View	***LAT***	***DBL***	***DBL2***
Bending	Medial	*47.7%*	*30.3%*	*27.5%*
	Posterior	*10.1%*	*10.5%*	*3.0%*
Compression	Medial	*35.8%*	*2.1%*	*5.9%*
	Posterior	*26.0%*	*2.7%*	*2.8%*

of motion observed in the medial view (30.3%). However, the addition of the two distal screws in DBL2 was able to further reduce the motion in the medial and posterior views.

During the 2D testing, the positions of markers #1 and #6 were used for verification that the markers on the same fragment (#1-3 and #4-6) were not moving with respect to each other. A triangle was created where each of the three markers represented the three vertices. The standard deviation of the length of the sides of the triangles was determined across the sequence of images. The average of the standard deviations for the sides of a given triangle (proximal or distal) was calculated and is shown in Appendix H for each test of the lateral plate. Finally, the average of the two tests of each view and load was taken, resulting in values ranging from 0.0023 - 0.0336 mm. To better understand the effect of this marker deviation as a source of potential error for the 2D results, the distal segment deviations were divided by the shear and compression motions (also shown in Appendix H). The distal segment was chosen for the analysis because the distal fragment experienced the largest displacement during testing and was therefore subject to the most error. The posterior view of the bending load had the highest potential error at 16.1% and 15.2% of the total motion for shear and compression, respectively.

3.3.2 3D Fracture Motion Tracking

The relative translational fracture motion in the local co-ordinate system (X’, Y’, Z’) was determined for all 36 tests. Figure 3.17 shows the motion data obtained from a representative compression test for the lateral and double plated samples. It should be

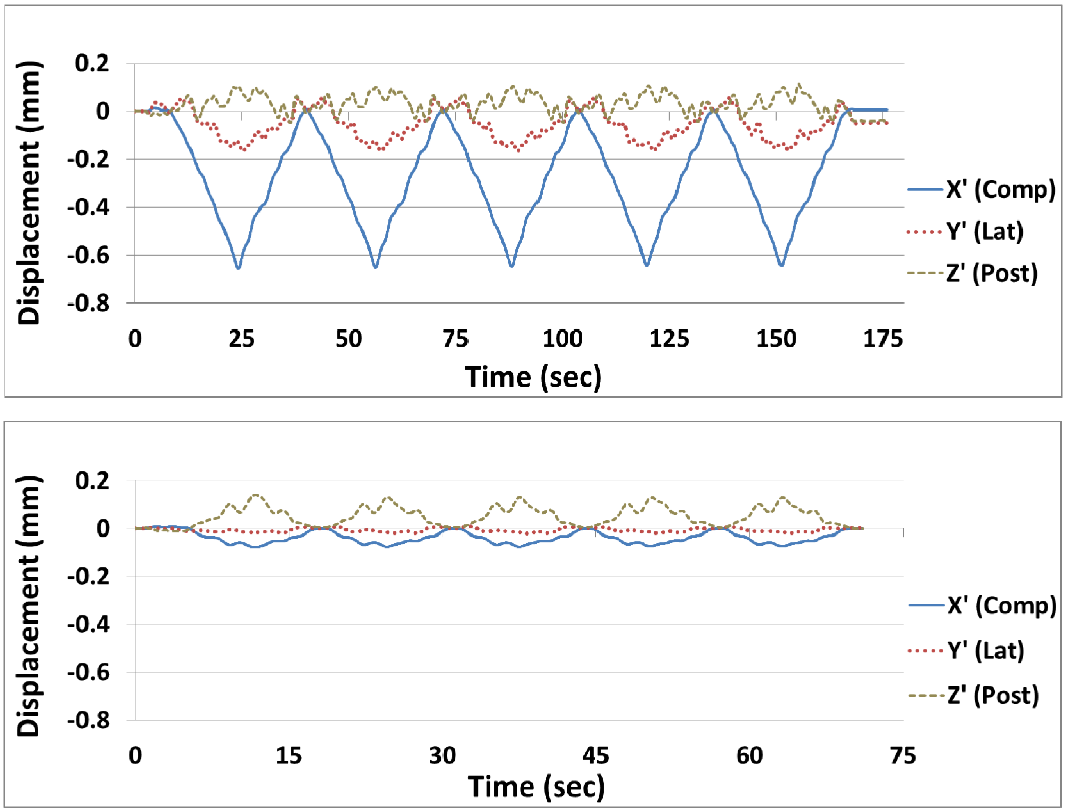

(A)

(B)

Figure 3.17: **3D motion for a representative sample.**
3D motion capture data for a representative compression test showing the three primary directions of motion (X, Y, Z). Results are shown for the **(A)** lateral plated sample; **(B)** double plated sample with distal screws.

noted that the response of the construct did not noticeably change over the duration of the five cycles.

In order to obtain the maximum and minimum values of motion for each direction, the time points corresponding to the maximum/minimum loads were identified for each test from the curve for the primary direction of loading of that test (X' for compression; Z' for bending). In several of the tests this local primary direction curve had excessive noise around the peaks, so time points were obtained from the global translation curve (X or Z). The maximum and minimum values of each of the (X', Y', Z') curves were taken based on the determined time points. For the curves with excessive noise, an average value of the data surrounding the time point (±1 second) was taken. The difference between the maximum and minimum values for each cycle in the X', Y' and Z' directions was then calculated and averaged to give the displacement for a given test. Only the final four of the five cycles were included in the average to further ensure the effectiveness of "warming up" the construct. The standard deviation for the four cycles in each direction was also calculated.

The results from the eight second static test to assess system noise are displayed in Figure 3.18. The noise along each of the local bone axes is displayed. The majority of the noise is contained within ±0.01 mm, with Z' occasionally increasing to ±0.015 mm.

Figure 3.19 and Figure 3.20 show the results for the compression and bending tests, respectively. The total resultant motion was also calculated by summing the vectors in the three directions ($Resultant = \sqrt{X^2 + Y^2 + Z^2}$). Significant differences were observed

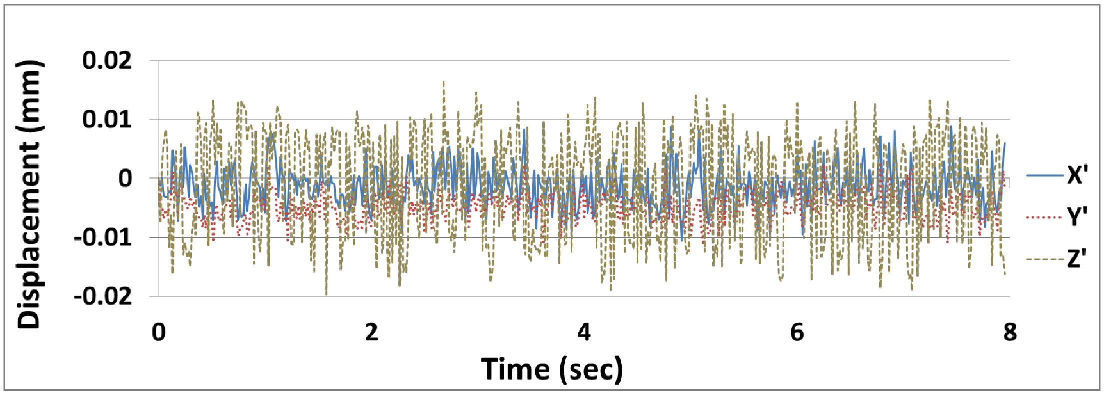

Figure 3.18: **3D static test to assess camera noise.**
An eight second test without any load being applied to the sample. This indicates the resolution of the system and marker noise during 3D motion capture. The noise along each of the local axis (X',Y',Z') are displayed.

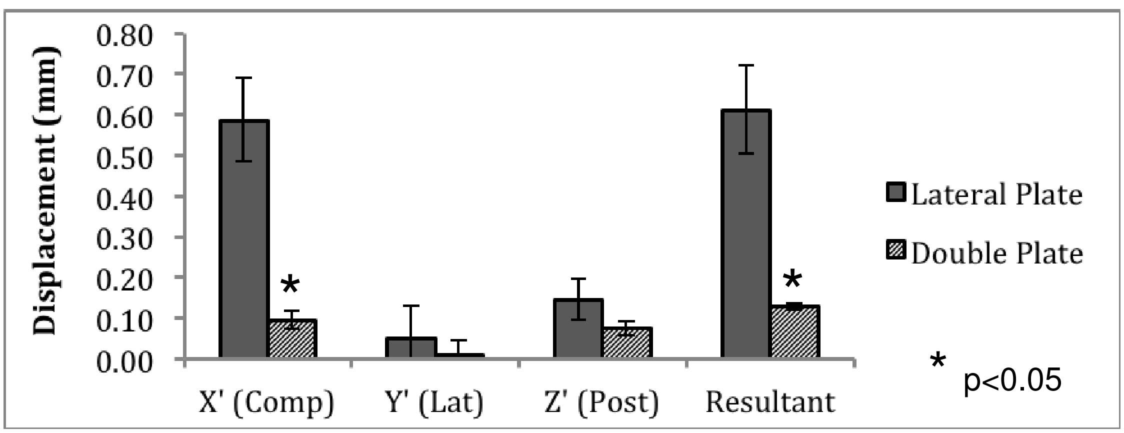

Figure 3.19: **Results from the 3D compression tests.**
Compression test results showing maximum fracture site motion of the lateral plate samples compared to the double plated samples for each of the three primary directions of motion and the total resultant motion. The absolute value of each of the motions was taken and the parentheses provide a description of the direction along the axis.

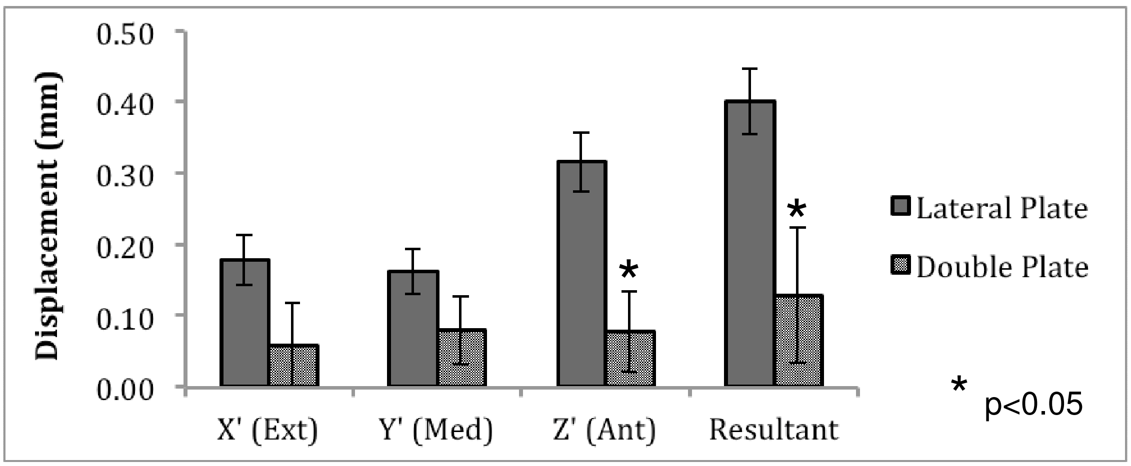

Figure 3.20: Results from the 3D bending tests.
Bending test results showing maximum fracture site motion of the lateral plate samples compared to the double plated samples for each of the three primary directions of motion and the total resultant motion. The absolute value of each of the motions was taken and the parentheses provide a description of the direction along the axis.

for the primary directions of loading in each case (X' for compression; Z' for bending), as well as the total resultant motion ($p<0.05$). It should be noted that the results for one of the double plated samples in bending had to be excluded. Excessive marker artefact and motion was found in the raw data files for that sample which prevented analysis of the three bending tests. Summary tables for the lateral and double plates can be found in Appendix I.

Table 3.4 shows the percent fracture motion for the 3D testing of the LAT and DBL2 samples. Similar to the 2D results, the LAT plate had motions greater than 10% in each of the loading configurations. The DBL2 construct resulted in reduced percent total motions with values of 4.3% in each of the compression and bending tests.

3.4 DISCUSSION

The purpose of this study was to compare fracture motion during experimental mechanical loading between a single lateral plate and a proposed double plated construct (with and without additional distal screws). Bending and compressive loads were applied to a synthetic femur treated with either plating option. Motion tracking was performed first using a set of sequential 2D images followed by 3D motion analysis using infrared cameras and reflective markers. Both methods of tracking demonstrated reduced motion for the double plated construct when compared to the lateral plate.

Table 3.4: Percent fracture motion for 3D testing of LAT and DBL2.

	LAT	***DBL2***
Bending	13.4%	4.3%
Compression	20.4%	4.3%

Several biomechanical studies have investigated the behaviour of clinically-used methods for stabilizing fractures of the distal femur (Bong et al., 2002; Duffy et al., 2006; Heiney et al., 2009; Higgins et al., 2007; Jaakkola et al., 2002; Marti et al., 2001; Otto et al., 2009; Salas et al., 2011a; Zlowodzki et al., 2004, 2006). Only a few of these have actually investigated the fracture motion under non-destructive loads (Bong et al., 2002; Duffy et al., 2006; Marti et al., 2001).

One study compared the motion experienced in treating a distal femoral fracture using a single lateral locking plate, dynamic condylar screw or a condylar buttress plate (Marti et al., 2001). Cadaveric samples under a 1,000 N axial compressive load had average compressive fracture displacements of 1.9 mm, 1.1 mm and 0.7 mm for the locking plate, condylar screw and buttress plate, respectively. Interpolating the 1.9 mm compression for 1,000 N load on the locking plate would give an approximate compression of 0.95 mm at 500 N. Considering the high interspecimen variability of cadaveric samples, this value is comparable to the 0.6 mm of average compressive displacement seen in the LAT samples during 3D testing.

Another study compared allowable motion of a periprosthetic fracture treated with either a locking plate or an intramedullary nail (Bong et al., 2002). An axial load (500 N) applied to the medial condyle (equivalent to varus knee loading) yielded compressive fracture displacements of 6.4 mm for the locking plate and 1.1 mm for the nail. The same axial load applied only to the lateral condyle (equivalent to valgus knee loading) yielded compressive fracture displacements of 0.1 mm for the locking plate and 1.4 mm for the nail.

The unicompartmental (loads isolated to a single condyle) forces applied in this study led to displacements that are harder to compare to the present study. The compressive force applied herein was always directed in the vertical direction (due to the constraints of the materials testing machine). So as the plates deflected, changes in the ratio of medial to lateral condylar load had the potential to change. In the case of the lateral plate testing, the medial side was unsupported and therefore more prone to deflection. After some initial displacement of the fracture, the loads applied to the samples with just the lateral plate would have become somewhat isolated to the lateral condyle (since the medial condyle was free to deflect). Therefore, the compressive loads in the current study are more representative of the isolated lateral condyle loading in the Bong et al. study. The results from both studies align with this hypothesis, as the 0.6 mm of compressive displacement observed the current study is much closer to the 0.1 mm of motion under a lateral condyle load in the Bong et al. study (as opposed to the 6.4 mm under a medial load). This previous study was also the only one found to evaluate the construct under bending loads. However, it was unclear from their methods as to how their results for the bending tests were obtained, so an accurate comparison could not be made. Given the difference in testing methods and conditions between the present study and two described in this section, the results from either can be considered to be comparable in magnitude.

Unlike the majority of previous studies this study investigated the fracture motion under non-destructive loads in multiple configurations (compression and bending). The current study was also the first known to investigate the performance of a novel double plated treatment method in comparison to current surgical techniques. Using 3D motion capture technology to track fracture motion is another novel aspect to this study. Complete 3D motion data were collected for cyclic loading without the need to intermittently measure displacement.

3.4.1 Comparison of 2D and 3D Percent Fracture Motion

As a measure of potential secondary bone healing (and corresponding clinical success), percent fracture motion was calculated by dividing the resultant motion by the fracture gap size. This method of representing construct effectiveness was also performed during a study comparing three different fracture treatment methods (Duffy et al., 2006). Although a different range for optimal secondary bone healing was chosen (5-15%), the principle of using percent fracture gap motion to assess healing potential was the same.

For the current study, the percent motion calculation was performed using results from both the 2D and 3D image capture methods. The values obtained for the 2D percent fracture motion do not represent the entire motion but instead only focus on the motion for a particular view. Therefore, in order to compare 2D and 3D values, the information from the medial and posterior views for each 2D test must be combined to represent expected 3D motion (Table 3.5). 2D extension/compression values were taken from the posterior view (as opposed to the medial view) since the 3D motion was captured from

Table 3.5: Total motion comparison between 2D and 3D results.
Information from 2D and 3D results are combined into the presented table. 2D extension/compression values were taken from the posterior view (as opposed to the medial view) since the 3D motion was captured on the posterior surface. 2D shear (Med/Lat) and shear (Ant/Post) values were taken from the posterior and medial views, respectively. Since different maximum loads were used for 2D and 3D tests, the 2D bending percentages were divided by two and the 2D compression multiplied by 5/6 (to get equivalent loads of 250 N and 500 N, respectively). 3D values for each component of motion were taken directly from the 3D results.

		LAT				DBL2			
	Motion [mm]	*2D*		*3D*		*2D*		*3D*	
Bending (250N)	Extension	*0.11*	*± 0.00*	*0.18*	*± 0.04*	*-0.05*	*± 0.00*	*0.06*	*± 0.06*
	Shear (Med)	*0.10*	*± 0.01*	*0.16*	*± 0.03*	*-0.01*	*± 0.00*	*0.08*	*± 0.05*
	Shear (Ant)	*0.63*	*± 0.00*	*0.32*	*± 0.04*	*0.41*	*± 0.01*	*0.08*	*± 0.06*
	Resultant	***0.65***		***0.40***		***0.41***		***0.13***	
Compression (500N)	Compression	*0.65*	*± 0.02*	*0.59*	*± 0.10*	*0.07*	*± 0.00*	*0.10*	*± 0.02*
	Shear (Lat)	*0.06*	*± 0.00*	*0.05*	*± 0.08*	*0.02*	*± 0.00*	*0.01*	*± 0.04*
	Shear (Post)	*0.08*	*± 0.01*	*0.15*	*± 0.05*	*0.13*	*± 0.01*	*0.07*	*± 0.02*
	Resultant	***0.66***		***0.61***		***0.15***		***0.13***	

the same posterior surface. 2D shear in the medial/lateral and anterior/posterior directions were taken directly from the posterior and medial views respectively. The resultant motions for both analysis methods were calculated and converted into percent fracture motions (Figure 3.21).

All of the values for the 2D and 3D results were similar for the compression testing, as confirmed by the percent fracture motion comparison in Figure 3.21. However, there were large differences between the 2D and 3D bending results. The majority of the disparity was represented in the measurement of the anterior shear. It is hypothesized that since different locations were tracked during bending (posterior vs. medial surfaces), the effect of distal fragment rotation on the translational components would have been different (further highlighted in Figure 3.22). The greater anterior shear for the 2D results along with the larger extension for the 3D motion is consistent with this hypothesis.

Several considerations need to be made when considering percent fracture motion as a means to assess healing potential. First, the calculated percentages depend on the initial fracture gap size and the loads to which the samples were subjected. If percent fracture motion is considered as the only measure of success, it would suggest that if the motion is kept constant, a larger fracture gap would result in improved healing. This is obviously not true as there is a transition point where the gap would be too large for a callus to form. One study looked at the influence of fracture gap size on healing in 42 sheep (L. Claes et al., 1997). Fracture gaps of 1, 2 or 6 mm were created and stimulated under the control of an external fixator. It was found that healing declined between the 2

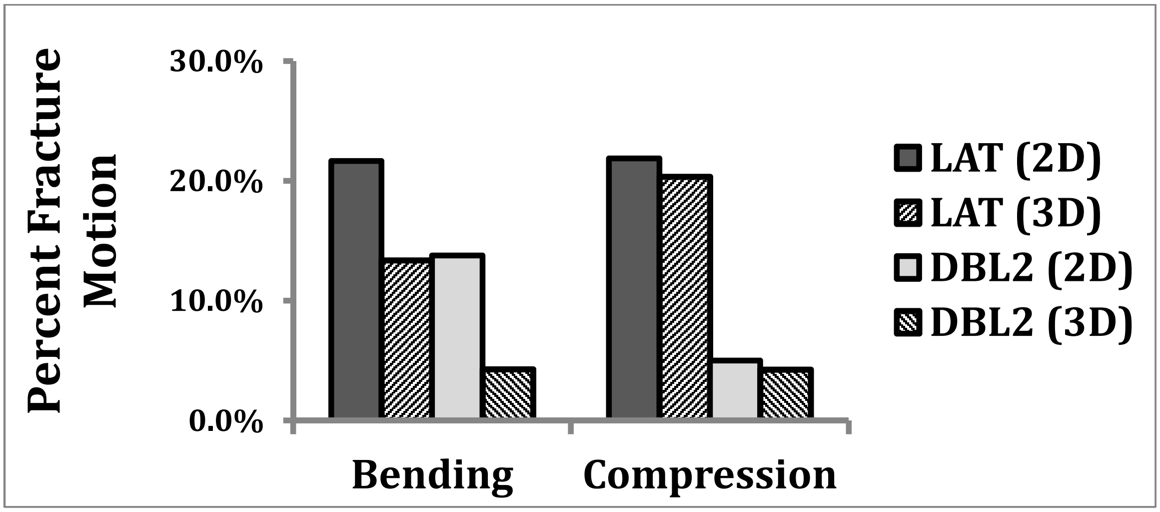

Figure 3.21: **Comparison of percent fracture motion between 2D and 3D results.** Resultant values from Table 3.5were divided by 3 mm (fracture gap size) to get the displayed percent fracture motion.

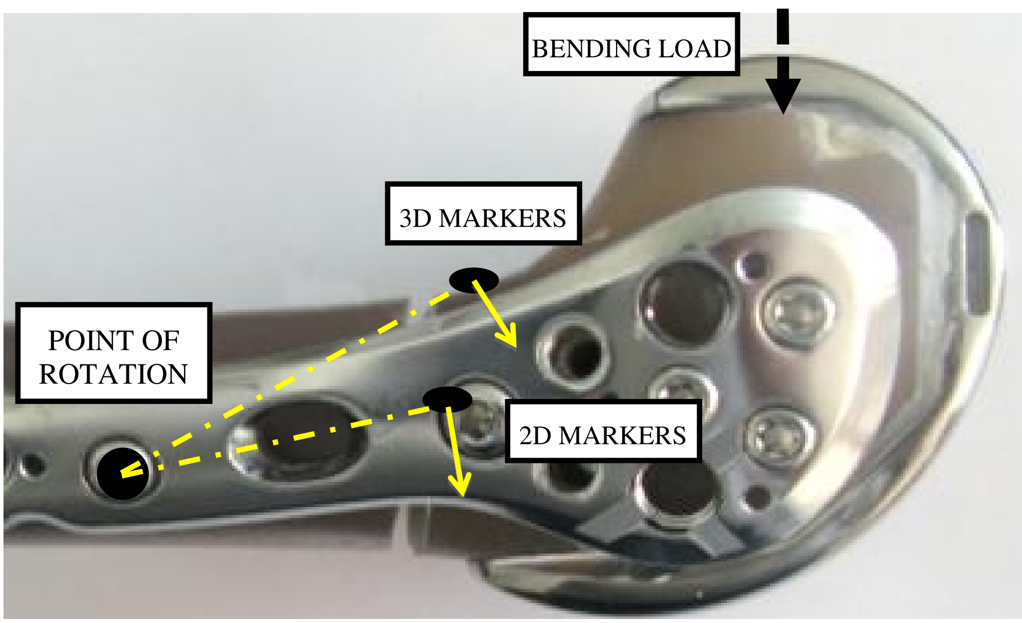

Figure 3.22: **Rotation effects on anterior shear measurement during bending.** The estimated location for the point of rotation (POR) during a bending test was chosen as the most distal screw on the proximal femur (closest to the fracture gap). As the bending load was applied, there was a slight deflection and rotation of the plate downwards about the POR. This rotation caused the two marker sets to shift in the direction shown by the solid arrows (normal to a line connecting the POR to the markers). While the motion of the 2D markers tended to contribute almost exclusively to anterior shear, the 3D markers had a smaller anterior shear since they also contributed to extension.

and 6 mm fracture gap groups. This suggests that the transition point is somewhere between this range. Therefore, a 3 mm gap was chosen based on the information from the aforementioned study, sizes used in previous distal femur fracture fixation studies, as well as through recommendation from an experienced orthopaedic surgeon. The loads applied to the samples also heavily influenced the percentages, and further investigation into the loads experienced at the knee during early stage rehabilitation of the fracture should be conducted.

These percent fracture motion calculations also did not take into account the detrimental effects of shear motion. One study found that 1.5 mm of pure shear motion led to 36% reduction in callus formation when compared to the same magnitude of purely axial loading (Augat et al., 2003). The calculations in the current study were simplified to assume that shear and axial (compression/extension) motions would have the same effect on healing. The fracture motion values also did not consider the effects of rotation of the sample; only the resultant translational motion was considered. Therefore, better representations of the shear vs. axial motion as well as including rotation in the calculations should be considered in future work.

3.4.2 Comparison of 2D and 3D Testing Methods

There are benefits and drawbacks to each of the two methods used to analyze the motion in the current work. The 2D analysis resulted in lower standard deviations than the 3D testing and therefore could be seen as the more precise method. The 2D analysis also included information about the relative rotation between the fragments. This rotational information is available within the 3D data but is much more time consuming to extract. Since the relative rotation in the 2D tests was quite low with an average value of 0.3° (maximum of 0.9°) it was determined that it could be neglected for the 3D analysis.

Drawbacks to the 2D testing were primarily due to the assumptions made during analysis of the results. Firstly, the two views were not focused on the same location of the bone. The posterior region was tracked in the posterior view while the medial region was tracked in the medial view. The 3D testing on the other hand was able to capture the complete motion through a single set of markers situated on the posterior aspect. Secondly, the 2D tests assumed that the fracture motion was identical during the two loading attempts needed to capture both views. The inaccuracies surrounding the use of a screw-driven mechanical test system likely contributed to any error between the motion in the two views and the repeatability between tests. However, the exact magnitude of this contribution has yet to be determined. Thirdly, the 2D tests were performed while holding at the target loads to capture the 2D images, whereas the 3D tests were performed under continuous loading.

Setting up the 2D testing was also quite tedious at times and took much longer than the 3D testing to load a sample. Calibration of the camera had to be performed for each test and in both the medial and posterior views. The need to apply incremental loads and capture two views for each test also significantly added to the total time required for the experiment.

While attaching the digital microscope directly to the proximal femur kept the image in focus for the most part, excessive out-of-plane motion of the distal fragment resulted in the distal bone moving slightly out of focus during loading. The contribution of this motion to the error in the 2D results was evident during the triangle motion analysis (Appendix H). The largest out-of-plane motion occurred when the bending load was viewed posteriorly. As the distal fragment moved out of focus, the triangle lengths changed in size. This resulted in a potential error in that view of 16.1% and 15.2% for shear and compression, respectively.

The primary benefit of using 3D motion capture technology was its ability to fully characterize the fracture motion in a single quick test. It provided complete 3D motion without the need to extrapolate the data such as was required for the 2D results. Also, the uninterrupted ramped loads during this testing made it more conducive to analyzing the effects of cyclic loading. Finally, the speed at which the tests could be performed after the initial configuration and calibration of the cameras allowed for an increase in sample size without a large increase in set-up time.

Despite the improvements in experimental methods, there are still some concerns with limitations in the 3D results. While the presented results indicated that there was little change in motion across the five cycles, inaccuracies of the mechanical testing system prevented precise loading to the desired maximum load (500 N for compression, 250 N for bending). Previous experience with the system suggests that the error in reaching a desired peak during cyclic loading could be as high as ±10 N. Also, the amount of noise seen in some tests and the fact that the bending results for one of the samples had to be neglected suggests that the threshold of the motion capture system's capabilities was approached in the current tests. However, the noise analysis (Figure 3.18) as well as the differences observed in the results between the two plating techniques lead us to believe that we are achieving sufficient accuracy and repeatability in our tests.

Further research in this area should be performed using 3D motion capture technology. Considering the issues involved in each of the analysis techniques, 3D tracking has a much larger potential for success. Refinement of the system parameters, camera placement, number of cameras, and appropriate marker size selection may all help to contribute in reducing marker artefact and noise; whereas the issues involved with the 2D technique are inherent to the method and may be difficult to remedy.

3.5 CONCLUSION

In conclusion, a custom double plated construct achieved increased stabilization in a simulated fracture model when compared to a single lateral plate. While these preliminary results are quite promising, additional experimental testing must be performed to determine the maximum load the construct can withstand, its ability to stabilize complex fractures and how it performs under unicompartmental loading. The results from the current study suggest that the double plated construct would provide better stability than existing techniques for treating periprosthetic fractures of the distal femur.

CHAPTER 4: FINITE ELEMENT ANALYSIS

4.1 INTRODUCTION

Finite element analysis is a powerful tool that can provide important stress and strain information about a structure under loading. One of the most important tasks to perform when developing a finite element model is to validate the results using experimental testing. After a model is validated, a variety of variables can be investigated in a relatively short period of time compared to experimental testing with a real-world physical structure. This makes the combination of experimental and computational models quite valuable in the process of developing and testing a product.

Limited research has been published on the development of a finite element model to study the treatment methods used for fixing a periprosthetic fracture (Salas et al., 2011b; Shah et al., 2011). Both of these studies were successful in using experimental testing to validate the FE model (based on RMS error and the correlation coefficient). However, neither of these studies looked at relative motion across the fracture site.

The purpose of this study was to develop a finite element model representative of the experimental setup described in Chapter 3 and refine it to best match the relative fracture motion results. This is the first known study of its kind to create a model that examines the motion of a fixed periprosthetic distal femur fracture.

4.2 MATERIALS AND METHODS

A simplified 3D model of the experimental setup was developed from the model described in Chapter 2. Using three-dimensional computer aided design software

(Inventor 2011; Autodesk, San Rafael, CA), the plates were joined to the prosthesis with a rigid connection as opposed to the tab-slot interface used experimentally (Figure 4.1). It was assumed that motion between the plate tabs and the prosthesis slots in the experimental model was negligible compared to the plate deformations, and that the rigid connection in the finite element model would suitably model this interaction. In a similar manner, the connections between the plates and the various screws (proximal, distal, and transverse compression) were joined to create a single part. These modifications created a single construct that included the plates, screws, and prosthesis (Figure 4.2) and reduced the number of interactions that needed to be modelled. The screws were further simplified by replacing the threaded screw-bone interface with a smooth rod that was inserted into the bone, as has been done previously (Zdero et al., 2008).

Initially, the tibial components of the experimental testing setup (tibial tray and polyethylene insert) were replaced with a simplified part that was created by extruding a cylinder vertically from a model of the polyethylene insert (Figure 4.3). After preliminary analysis using this simplified part, the original tibial tray and insert were added to account for any deflection that may occur in the shaft of the tray. Models of these components were obtained directly from the manufacturer (Stryker Orthopaedics, Mahwah, NJ) and added to the assembly shown in Figure 4.4. Minor simplifications were made to each of these parts to merge any small faces that could lead to complications during the meshing procedure. The finished assembly was then exported as a .STEP file and imported directly into Abaqus CAE version 6.8-3 (Dassault Systèmes, Waltham, MA).

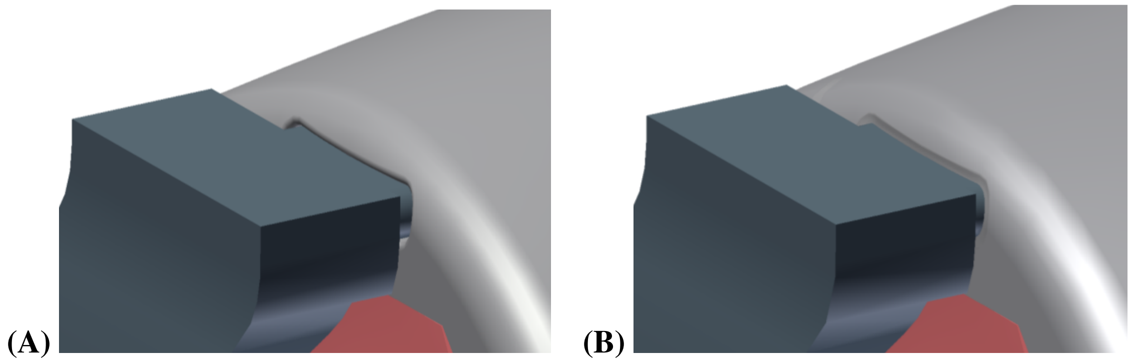

Figure 4.1: Magnified view of the plate-prosthesis connection.
The plate-prosthesis interface was simplified from a tab-slot connection **(A)** to a rigid connection **(B).**

Figure 4.2: Simplified plates, screws, and prosthesis construct.
The plates, screws, and prosthesis were treated as a single construct with rigid connections and the same material properties.

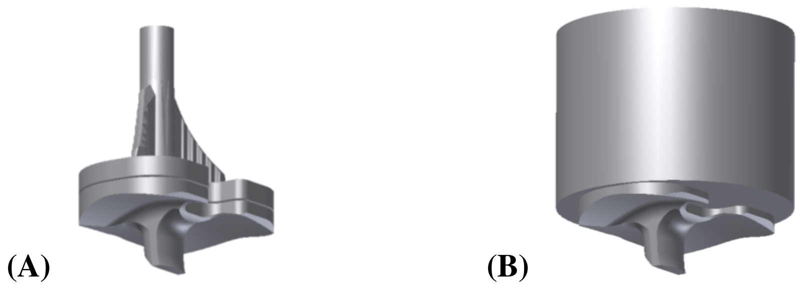

Figure 4.3: Simplified tibial components.
The more complex models of the tibial tray and polyethylene insert **(A)** were initially replaced with a simplified part consisting of a cylinder extruded from the original insert **(B)**.

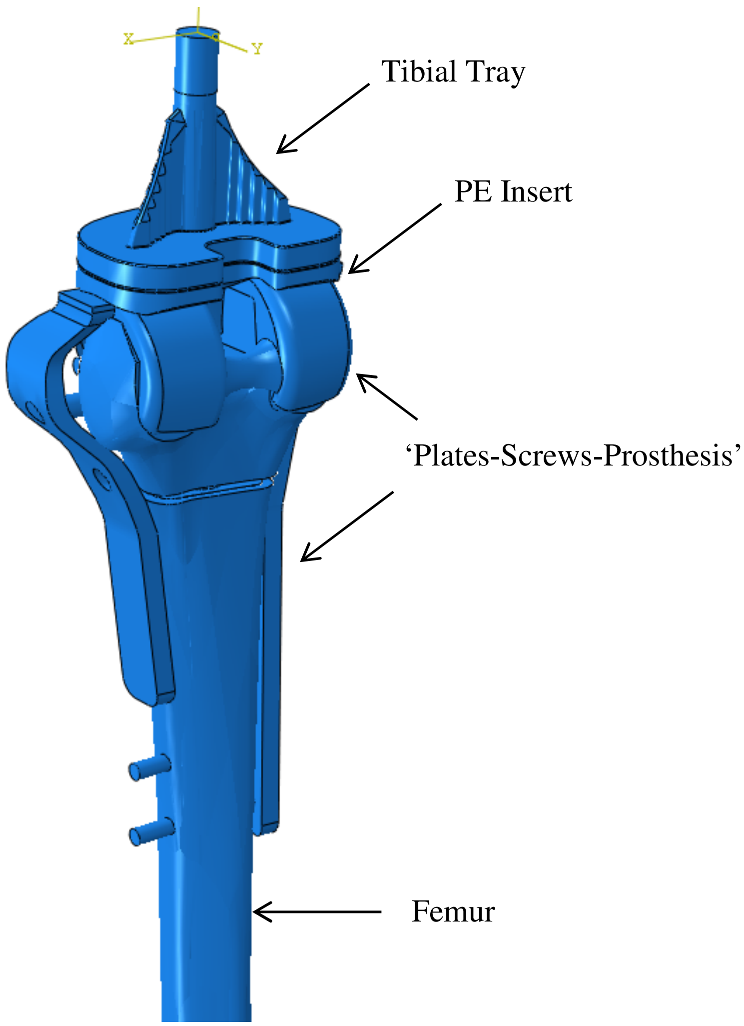

Figure 4.4: Complete FE assembly.
The FE assembly is shown with all the components. Top to bottom: tibial tray, polyethylene insert, plates-screws-prosthesis, and femur.

4.2.1 Meshing

After importing the different components of the model, a 'virtual topology' operation was performed to smooth any remaining small faces and merge tangential surfaces. This was done to reduce the number of distorted elements, thus improving the quality of the mesh. Four-node linear tetrahedral elements were used to create the mesh for each component during initial iterations of the analysis Figure 4.5. Using linear elements reduced the required computational time and allowed multiple analyses to be conducted for quicker refinement of the model. After sufficient refinement had taken place, the element type for each component was switched to ten-node quadratic tetrahedral elements. Quadratic elements are able to better match the geometry of the parts and provide a more accurate response to applied loads. Details about the number of elements for each component of the model can be found in Appendix J.

4.2.2 Material Properties

Material properties for each part were defined based on previous studies or manufacturers specifications (Table 4.1). Each material was considered to be linear elastic and isotropic. The density, elastic modulus, and Poisson's ratio for the synthetic bone was based on values for 4th generation composite bones provided by Pacific Research Laboratories. To get a single elastic modulus for cortical bone, the average of the compressive (16.7 GPa) and tensile moduli (16.0 GPa) was taken, similarly to a previous study (Cheung et al., 2004). The remaining material properties for 316 stainless steel and ultra-high-molecular-weight polyethylene (UHMWPE or PE) were based on

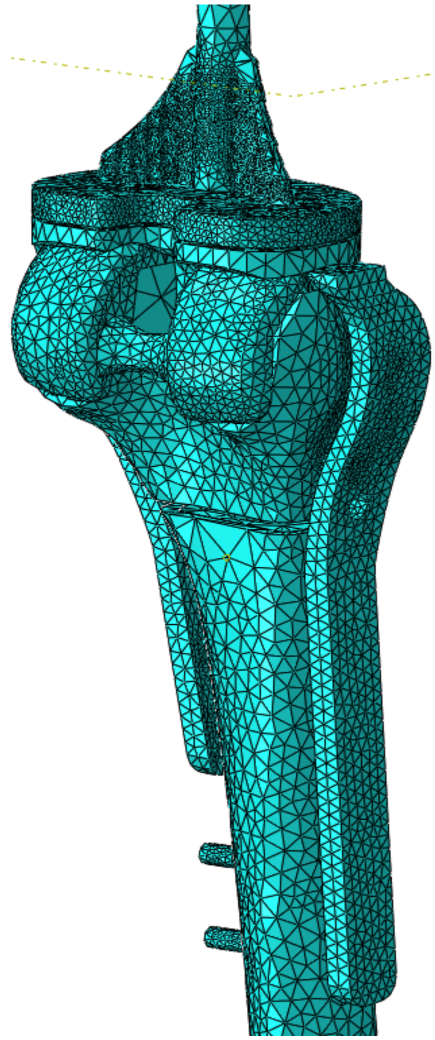

Figure 4.5: FE model after meshing.
The FE model is shown following the meshing operation. Linear 4-node tetrahedral elements were used for the majority of the analyses (shown in the figure). Quadratic 10-node tetrahedral elements were used for the final analysis.

Table 4.1: Material properties for FE model components.
The material properties for each component of the FE model are described below.

Property	Synthetic Cortical Bone	Synthetic Cancellous Bone	316L Stainless Steel	UHMWPE
Density (g/cm^3)	1.64	0.27	8	0.9392
Elastic Modulus, E (GPa)	16.35	0.155	193	0.9
Poisson's Ratio, n	0.26	0.3	0.3	0.4
Material Model	Linear elastic	Linear elastic	Linear elastic	Linear elastic
Property Directionality	Isotropic	Isotropic	Isotropic	Isotropic

those reported in two previous studies (Bougherara et al., 2010; Shah et al., 2011). The components of the model were then assigned materials as shown in Figure 4.6. The entire “plates-screws-prosthesis” part was first assigned 316 stainless steel even though experimentally the prosthesis is made out of a Cobalt Chromium (CoCr). The material was later changed to CoCr to quantify the effect of this simplification. During the initial iterations of the analysis, the entire simplified tibial component (Figure 4.3B) was assigned 316 stainless steel. To account for any deformation in the PE of the insert this part was later partitioned into two sections: the extruded cylinder and the tibial insert. The cylinder was kept as steel while the insert was assigned the PE properties. Finally, to account for any experimental deformation of the tibial tray, the cylinder was eventually replaced with the model of the tray and assigned the stainless steel properties.

4.2.3 Constraints and Boundary Conditions

Next, constraints were applied between different parts to simulate the experimental model. Tie constraints (bonding of surfaces to prevent relative motion) were specified between the cortical and cancellous portions of the femur as well as between the tibial tray and polyethylene insert. Experimentally, a thin layer of bone cement is normally applied between the femoral component and the distal bone. However, a previous pilot study found that modeling the bone cement as a tie constraint was an acceptable representation for the union between the prosthesis and the bone (Bougherara et al., 2010). A tie constraint was also used to simplify the screw-to-bone interface and mimic the thread purchase in the bone (Shah et al., 2011).

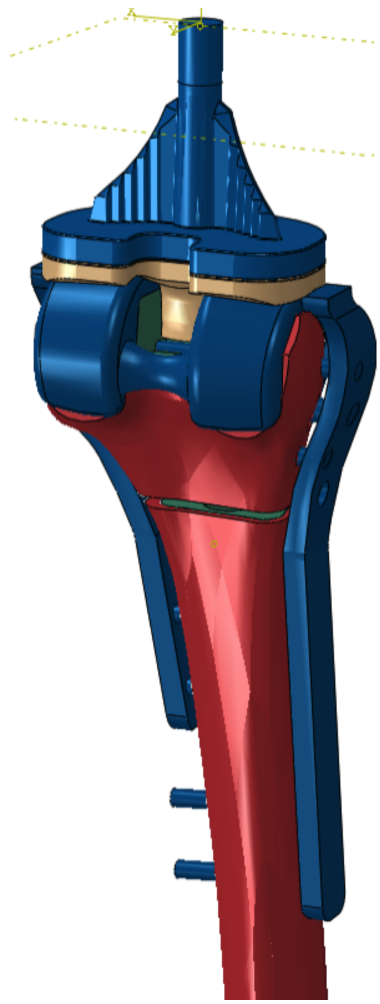

Figure 4.6: FE model showing the different components coloured by material. All of the components of the FE model are displayed in different colours based on their material definitions. Red – cortical bone; green – cancellous bone; blue – 316 stainless steel; gold – UHMWPE.

Initially, the surfaces between the tibial insert and the prosthesis were also tied together. After preliminary analysis, frictional contact was assigned between the polyethylene insert and the femoral implant. This prevented the two surfaces from overlapping and added frictional behaviour to any tangential motion. One previous study investigated the frictional coefficients for polyethylene (UHMWPE) on CoCr (Kim et al., 2011). It was discovered that if both surfaces were dry, the coefficient would change from 0.03 to 0.15 as the contact pressure decreased from 80 MPa to 5 MPa. A preliminary analysis using the FE model found that the contact area between the PE insert and the femoral prosthesis was approximately 1 cm^2. For the 500 N load applied in during compressive loading, this contact area would produce a 5 MPa contact pressure between the surfaces. According to the previous study this would result in a frictional coefficient of 0.15. However, considering the wear of the PE insert from multiple tests being conducted and any scratches that might develop on the prosthesis due to handling, a coefficient of 0.2 was chosen for the analyses.

Boundary conditions were added to the model to replicate those used experimentally (Figure 4.7). To mimic the potting of the sample, the proximal portion of the femur was fixed in all directions so that 230 mm of the distal femur was unconstrained. In order to reproduce the vertical motion of the actuator of the material testing system, the upper portion of the tibial tray was constrained to only allow translation along the vertical z-axis.

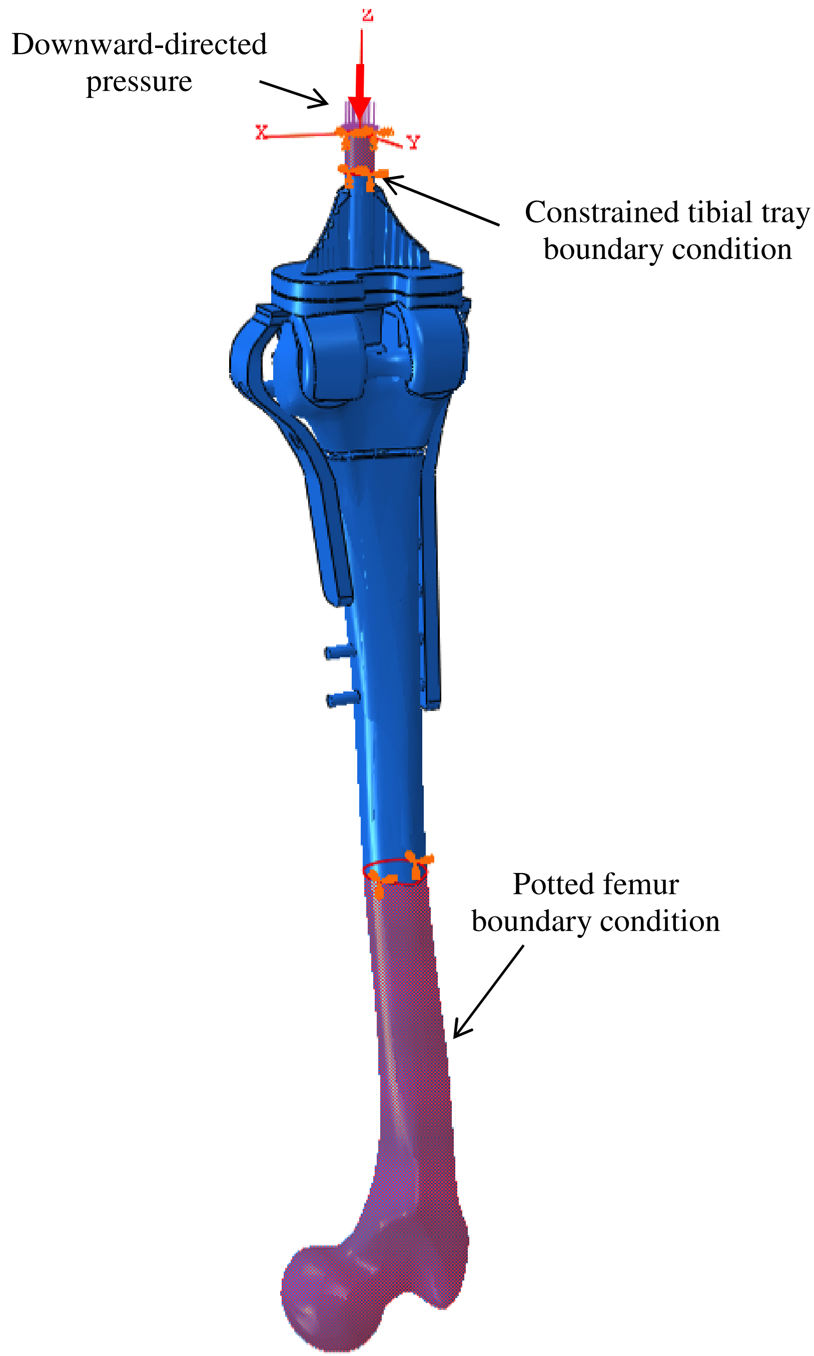

Figure 4.7: **Boundary conditions and loads for the FE model.**
The two boundary conditions applied to the model are highlighted in red. The proximal femur was fully fixed to mimic the potted femur. The tibial tray was only permitted to move in the vertical direction (along the z-axis of a local tibial tray coordinate system) to replicate the loading applied by the materials testing machine. The downward pressure on the top surface of the tibial tray is also shown in the figure by the red arrow.

4.2.4 Loads

The final step was to define the loads applied to the model. An evenly distributed pressure was applied to the top surface of the tibial tray stem to cause a compressive force that was directed downwards through the tray/insert and onto the femoral implant (Figure 4.7). The top of the tibial tray stem was 11.08 mm in diameter, equalling a surface area of 96.45 mm^2 at the top surface of the stem. This corresponded to an applied pressure of 5.184 MPa. The pressure was defined as a uniform ramped pressure that started at 0 MPa and increased to the full amount by the end of the analysis. A seven second analysis was chosen to replicate the time it took for an experimental compression test to reach the peak load. For the analyses where the simplified tibial part was used from Figure 4.3, the pressure was applied to the top surface of the cylinder.

4.2.5 Validation of Initial Assumptions

Several verifications were performed as the model was developed to help validate and determine the impact of the initial assumptions. The friction coefficient, cortical bone modulus, construct material, tibial tray material and the alignment of the tibial components with respect to the prosthesis were all varied to understand how these parameters affected the outputs. This parametric analysis was conducted on the model with four-node linear tetrahedral elements since the computational time to run this model was significantly shorter than the one with quadratic elements. To investigate the assumption of a tied contact at the tab-slot interface, the relative motion between the distal bone and the plates was measured using a digital microscope (DinoLite, AnMo

Electronics Corp, Taiwan) (Figure 4.8). Similar to the 2D experimental testing (Section 3.2.1.3), the positions of florescent pieces of tape were captured at 0 N and 500 N of compression. The change in vertical position was measured using the DinoLite software (DinoCapture; AnMo Electronics Corp, Taiwan). This measurement was then compared to the same two points in the FE model to quantify the relative motion between the plates and the femoral prosthesis. To test the assumption that the screws were rigidly tied to the bone, the relative motion between a point on the lateral plate and the proximal bone was measured in a similar manner (Figure 4.9).

4.2.6 Bending Configuration

The model was then reconfigured to conduct a bending analysis (as was conducted experimentally) (Figure 4.10). The only changes from the described compression analysis were the orientation of the tibial components (rotated 90°) and the maximal applied load (250 N = 2.592 MPa pressure applied to the top surface of the tibial tray stem).

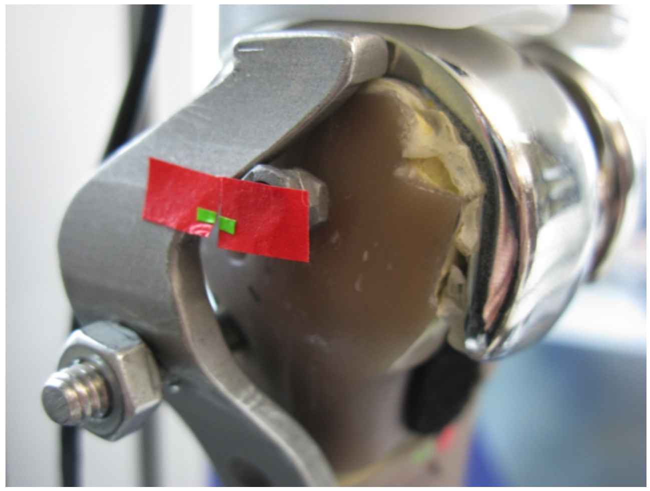

Figure 4.8: **Relative motion between the plates and distal bone.**
The relative vertical motion (parallel to the 'compression' direction) between the medial plate and the distal bone was measured using florescent markers and a digital microscope. The motion of the same two points in the FE model was also calculated to quantify any deflection of the plate between the marker and the tab. By subtracting the motion in the FE model from the experimental motion, the approximate tab-slot relative motion was obtained (since the prosthesis is rigidly cemented to the distal bone).

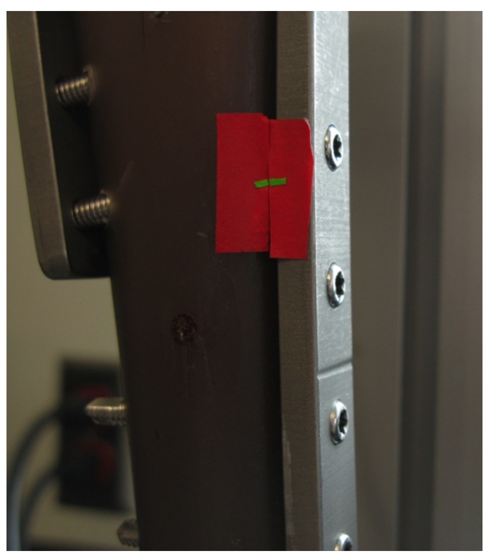

Figure 4.9: **Relative motion between the plates and proximal bone.**
The relative vertical motion (parallel to the 'compression' direction) between the lateral plate and the proximal bone was measured using florescent markers and a digital microscope. The markers were placed below the most distal screw so that only relative motion between the screw-bone and screw-plate interfaces was considered.

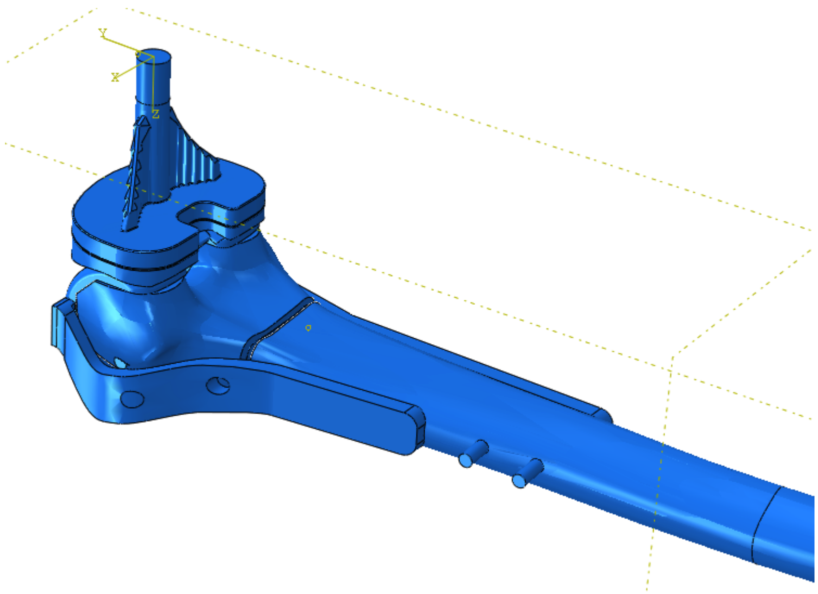

Figure 4.10: **Model reconfigured for a bending analysis.**
The tibial components were rotated 90° and the applied load was reduced to 250 N to model the experimental bending tests of the model.

4.3 RESULTS

To determine the relative motion of the fracture site in the FE model, the displacement of two nodes on the proximal and distal fragments were tracked over the duration of the analysis (Figure 4.11). Their motion was then resolved into a local coordinate system equivalent to the one defined during the experimental testing. The coordinate system followed the motion of the proximal fragment and had its origin at the same location as the proximal tracking node. The relative motion between these nodes was then calculated in each of the three primary directions of the local coordinate system (x,y,z).

Numerous iterations of the analysis were conducted throughout the development of the model. The results from these iterations as well as a description of the input variables for each are outlined in Table 4.2.

<u>Iteration 1</u>: Iteration one was analyzed with the articulating portion of the tibial part tied directly to that of the femoral prosthesis so that no translation could occur between the two surfaces. This resulted in relative motion values that were much lower than the experimental values with only 12-14% of the 2D and 3D resultant motion.

<u>Iteration 2</u>: The tie constraint was replaced with surface-to-surface contact. This resulted in increased motion in all directions (still below the corresponding experimental values) with very large motion in the medial direction. This excessive medial shear was thought to be caused by unrestrained slippage between the tibia and femur parts. Therefore, friction was added to the contact properties for the third iteration.

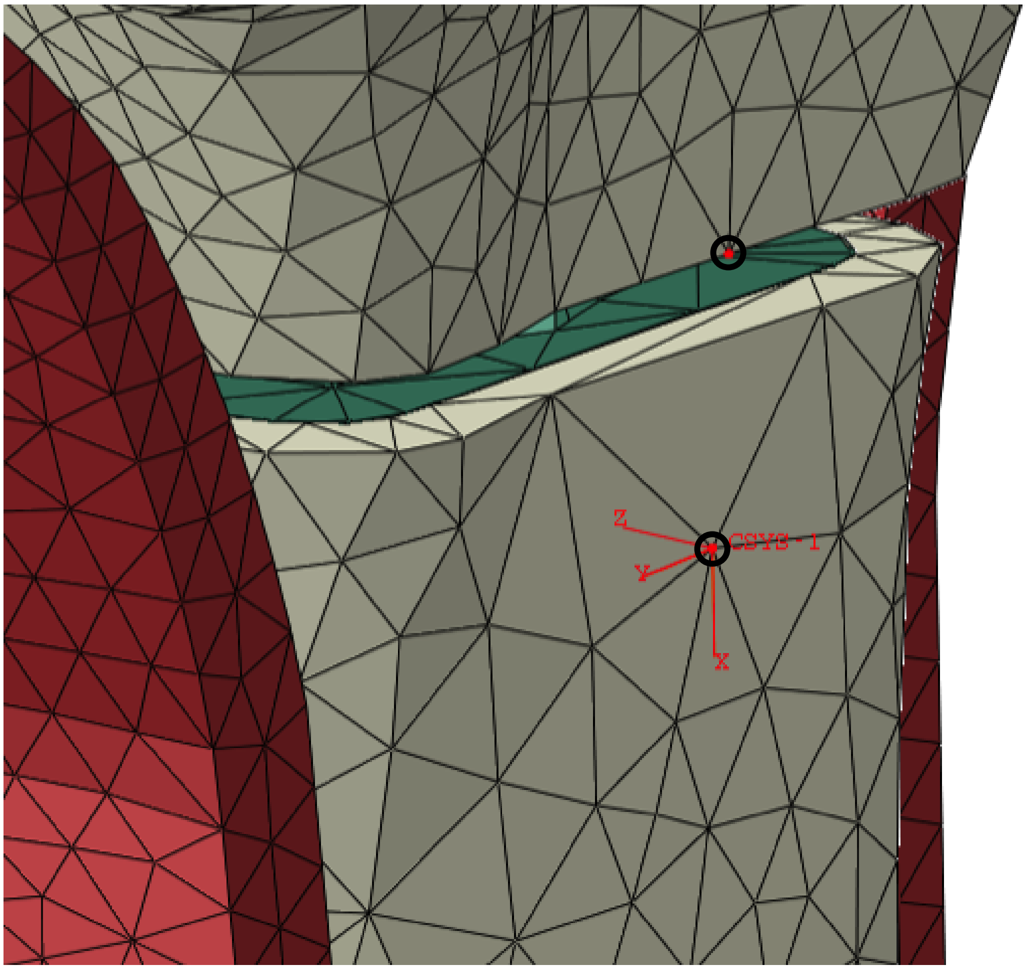

Figure 4.11: Tracking nodes to determine relative fracture motion.
The displacements of two nodes (one on the each of the proximal and distal fragments) were tracked during the analysis. Their motion was then resolved into a local bone co-ordinate system (shown), which was defined in a manner similar to the experimental testing. These specific nodes were chosen because they were aligned with the x-axis and in a similar location to the markers used during experimental testing.

Table 4.2: **Development of the FE model and corresponding results.**
The primary iterations of the FE model development are shown along with their results in each of the primary directions compared to the 2D and 3D testing. Brief descriptions of the iterations are shown in the first column followed by the relative motion results and a further description of the input variables used.

		X (Comp)	Y (Med)	Z (Post)	Resultant	Tibial Components	Friction Coeff.
	Experimental - 3D	0.100	-0.010	0.070	0.130		
	Experimental - 2D	0.070	-0.020	0.130	0.150		
1	Tie Constraint	0.012	0.007	0.011	0.018	Simplified (all steel)	None
2	Surface to Surface Contact	0.033	0.077	0.025	0.087	Simplified (all steel)	None
3	Friction Coefficient (0.1)	0.027	0.035	0.004	0.044	Simplified (all steel)	0.100
4	Friction Coefficient (0.2)	0.024	0.023	-0.005	0.033	Simplified (all steel)	0.200
5	Partitioned Tibial Materials	0.024	0.021	-0.005	0.032	Simplified (steel cylinder; PE insert)	0.200
6	Added Distal Screws	0.016	0.019	0.007	0.026	Simplified (steel cylinder; PE insert)	0.200
7	Added Tibial Tray and PE Insert	0.016	0.016	0.009	0.024	Tray (steel) and Insert (PE)	0.200
8	Refined Plates-Screws-Prosthesis Mesh	0.019	0.021	0.010	0.030	Tray (steel) and Insert (PE)	0.200
9	Quadratic Elements	0.030	0.033	0.016	0.048	Tray (steel) and Insert (PE)	0.200

Iterations 3 and 4: An initial frictional coefficient of 0.1 was chosen followed by 0.2 for the fourth iteration. The addition of friction reduced the motion in each direction with the greatest effect occurring in the medial shear. A higher coefficient of friction limited the amount of shear between the tibia-femur and in turn further reduced the relative motion. At this point in the development of the model, the medial shear was still higher than required and the compression and posterior shear were lower than the experimental results.

Iteration 5: Iteration five involved partitioning the simplified tibial part into a PE and a steel section to account for any deformation of the PE during testing. This change had a negligible effect on the relative fracture motion.

Iteration 6: In an attempt to further reduce the medial shear and redirect it into increased compression, the distal screws used during experimental testing were added to the plate construct. The addition of these two screws reduced the compression and medial motions but increased the posterior shear.

Iteration 7: To further eliminate any differences between the FE model and the experimental setup, the simplified tibial part was replaced with accurate models of both the PE insert and tibial tray. This resulted in a slight decrease in the medial shear and a slight increase in the posterior shear.

Iteration 8: Iteration eight involved refining the mesh of the 'plates-screws-prosthesis' part. The approximate global mesh size (input parameter specified during meshing) was reduced from 4.7 (default) to 3. Slight increases in each of the directions of motion were observed with the decrease in mesh size.

Iteration 9: As a final iteration, all element types in the model were changed from four-node linear to ten-node quadratic. As expected, this further increased the relative motion in all directions. Final compression, medial shear and posterior shear results for the FE model were 0.030 mm, 0.033 mm, and 0.016 mm, respectively (Table 4.3). A Von Mises stress plot was generated for the model after the final iteration was conducted (Figure 4.12). This plot shows the peak areas of stress under the applied compressive load to be at the tab, around the screws and along the contours of the plates. A contour plot was also generated to display the vertical displacement of the model under the load (Figure 4.13).

Variation of the coefficient of friction between the PE insert and the femoral prosthesis had a relatively large impact on relative fracture motion. The coefficient was first set at 0.04, the bottom of the range found experimentally by Kim *et al.*, 2011. This was then increased incrementally to 0.3, with relative fracture motion determined for each value (Table 4.4). As the coefficient increased, motion in each of the directions decreased, with the largest change in medial and posterior shear.

Adjusting the position of the tibial components with respect to the femur resulted in moderate changes to the motions (Table 4.5). Rotating the components 1° medially and laterally increased and decreased the motion, respectively. Translating them 0.3 mm in the anterior direction had a minimal effect on the results.

Table 4.3: **Final FEA results compared to experimental compression tests.** The results from the final iteration of the FE model (iteration 9) are shown compared to the experimental data. The percent differences between the FEA and corresponding experimental results (3D and 2D) are shown in white (all dimensions in mm).

Compression (500N)	X (Comp)	Y (Med)	Z (Post)	Resultant
FEA	0.030	0.033	0.016	0.048
Experimental - 3D	0.100	-0.010	0.070	0.130
% Difference	*70%*	*435%*	*77%*	*63%*
Experimental - 2D	0.070	-0.020	0.130	0.150
% Difference	*57%*	*267%*	*88%*	*68%*

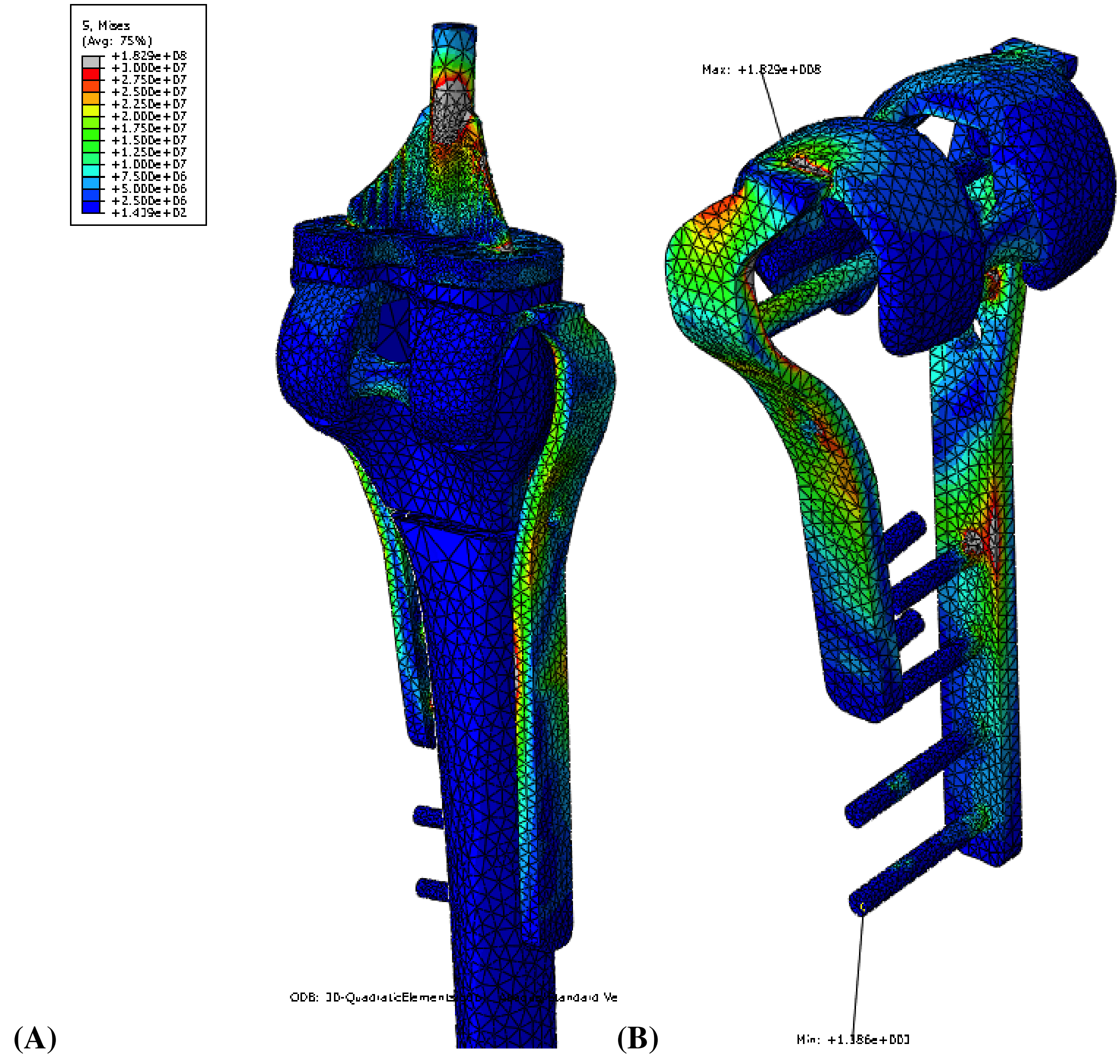

Figure 4.12: **FE model - Von Mises stress plots.**
Von Mises stress plots for **(A)** the entire FE model and **(B)** the isolated 'plates-screws-prosthesis' construct. The maximum and minimum stress locations are shown for the construct (units in Pa).

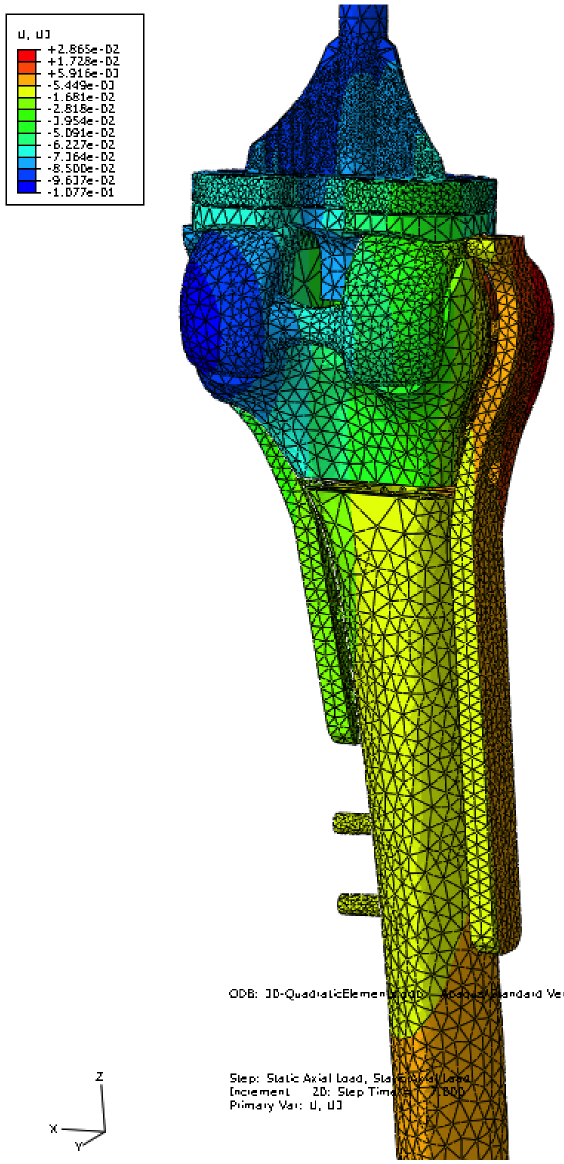

Figure 4.13: **FE model - displacement plot.**
A contour plot is shown for displacement of the model along the 'Z' axis as defined by the co-ordinate system shown (units in mm).

Table 4.4: **Variation of the friction coefficient.**
The friction coefficient between the PE insert and prosthesis was varied between 0.04 and 0.3. Relative fracture motions in each direction as well as the total resultant motion are shown (all dimensions in mm, shaded green represents baseline data from iteration eight).

Friction Coefficient	X (Comp)	Y (Med)	Z (Post)	Resultant
0.04	0.026	0.055	0.029	0.067
0.1	0.022	0.033	0.016	0.042
0.2	0.019	0.021	0.010	0.030
0.3	0.018	0.017	0.008	0.026

Table 4.5: **Variation of the tibial placement.**
The placement of the tibial component was varied slightly to understand the impact on the results. Relative fracture motions in each direction as well as the total resultant motion are shown (all dimensions in mm, shaded green represents baseline data from iteration eight).

Tibia Placement	X (Comp)	Y (Med)	Z (Post)	Resultant
Centered	0.019	0.021	0.010	0.030
Rotated 1° Medial	0.025	0.031	0.015	0.042
Rotated 1° Lateral	0.016	0.015	0.008	0.024
Translated 0.3 mm Anterior	0.019	0.019	0.007	0.028

The manufacturer of the synthetic femurs listed multiple material properties based on the direction of loading. To verify that taking the average of the tensile and compression moduli was a reasonable assumption, an analysis with the larger of the two moduli (16.7 GPa) was performed (Table 4.6). It was then repeated with the much lower transverse tensile modulus (10 GPa). Neither variation from the 16.35 GPa baseline value resulted in a large change in motion.

Finally, the 316 stainless steel of the tibial tray was replaced with the actual titanium material (Table 4.7). In a similar manner, the 'plates-screws-prosthesis' construct was also assigned the properties of CoCr (Table 4.8). Both of these modifications resulted in negligible change from the original data collected.

The relative motion between markers attached to the medial plate and distal bone is shown in Figure 4.14. A displacement of 0.059 mm of vertical motion was observed during 500 N of axial compression. For the FE model, the relative motion between two nodes at the same locations as the markers was only 0.008 mm. The relative motion between markers attached to the lateral plate and proximal bone is shown in Figure 4.15. A displacement of 0.013 mm of vertical motion was observed during 500 N of axial compression. For the FE model, the tie constraints of these two surfaces to the screw meant that there was no relative motion at this location.

The bending analysis resulted in values that fell between those observed during the 2D and 3D experimental tests (Table 4.9). At 250 N, extension was 0.028 mm, medial shear was 0.032 mm and posterior shear was 0.181 mm.

Table 4.6: Variation of the cortical bone modulus.
Analyses were conducted with cortical bone moduli of 10, 16.35, and 16.7 GPa. Relative fracture motions in each direction as well as the total resultant motion are shown (all dimensions in mm, shaded green represents baseline data from iteration eight).

Cortical Bone Modulus	X (Comp)	Y (Med)	Z (Post)	Resultant
10 GPa	0.020	0.024	0.011	0.033
16.35 GPa	0.019	0.021	0.010	0.030
16.7 GPa	0.019	0.021	0.010	0.030

Table 4.7: Stainless steel versus titanium tibial tray.
The tibial tray material was also modeled as titanium to demonstrate the effects of material selection on results. Relative fracture motions in each direction as well as the total resultant motion are shown (all dimensions in mm, shaded green represents baseline data from iteration eight).

Tibial Tray Material	X (Comp)	Y (Med)	Z (Post)	Resultant
316 Stainless Steel	0.019	0.021	0.010	0.030
Titanium	0.019	0.018	0.009	0.028

Table 4.8: Stainless steel versus cobalt chromium construct.
The ‘plates-screws-prosthesis’ construct was also modeled as cobalt chromium (CoCr) to demonstrate the effects of material selection on results. Relative fracture motions in each direction as well as the total resultant motion are shown (all dimensions in mm, shaded green represents baseline data from iteration eight).

Construct Material	X (Comp)	Y (Med)	Z (Post)	Resultant
316 Stainless Steel	0.019	0.021	0.010	0.030
CoCr	0.018	0.019	0.009	0.028

(A)
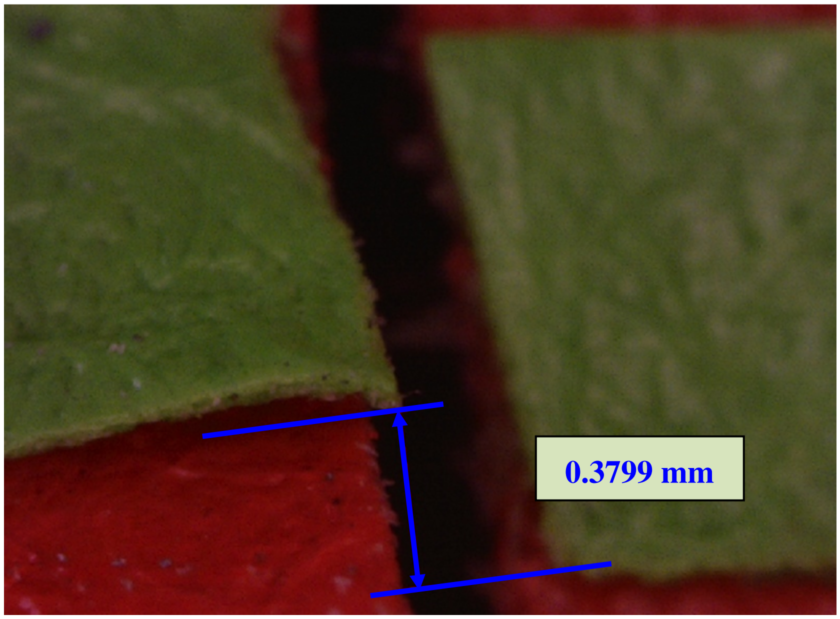

(B)
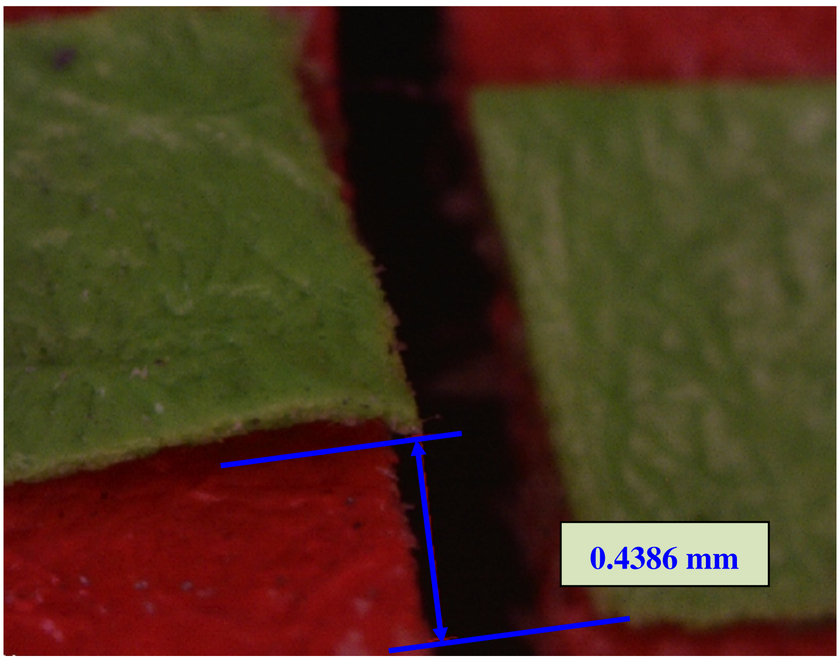

Figure 4.14: Relative motion between the medial plate and the distal bone. The change in vertical distance (parallel to the 'compression' direction) between markers attached to the medial plate and distal bone was measured using the DinoLite software. Image **(A)** shows a 0.380 mm distance between markers when a 0 N load was applied. Image **(B)** shows a 0.439 mm distance between markers when a 500 N load was applied. Therefore, 0.059 mm of relative motion occurred during the compressive load.

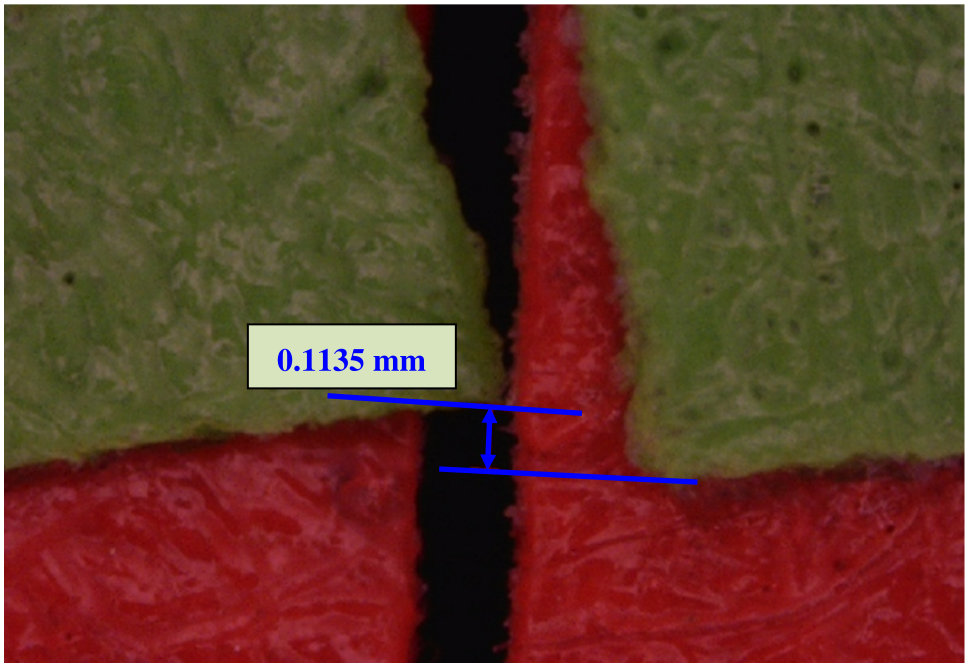

(A)

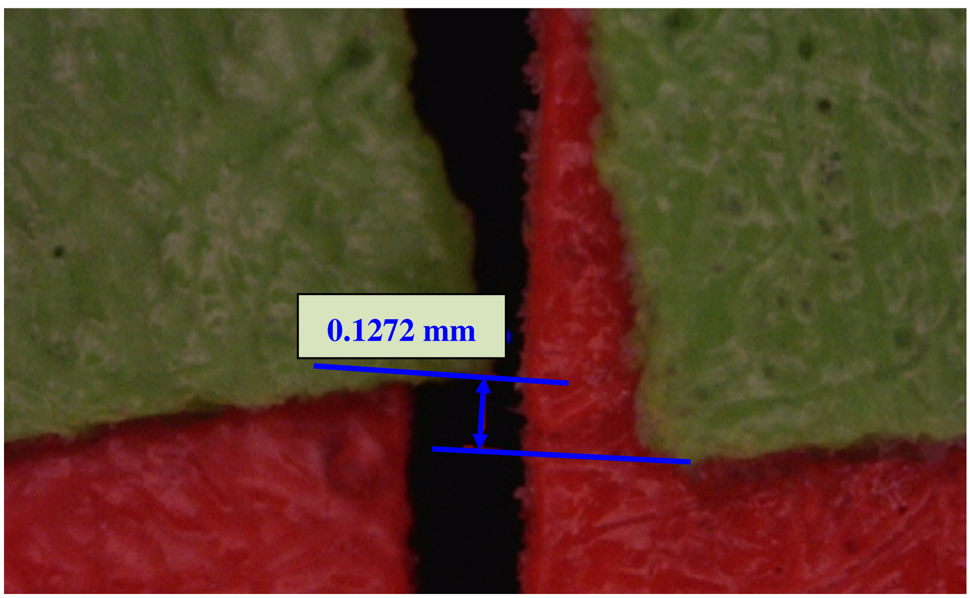

(B)

Figure 4.15: Relative motion between the lateral plate and the proximal bone. The change in vertical distance (parallel to the 'compression' direction) between markers attached to the lateral plate and proximal bone was measured using the DinoLite software. Image **(A)** shows a 0.114 mm distance between markers when a 0 N load was applied. Image **(B)** shows a 0.127 mm distance between markers when a 500 N load was applied. Therefore, approximately 0.013 mm of relative motion occurred during the compressive load.

Table 4.9: **Final FEA results compared to experimental bending tests.**
The results from the bending FE model are shown compared to the 2D and 3D experimental data. The percent differences between the FEA and corresponding experimental results (3D and 2D) are shown in white (all dimensions in mm).

Bending (250N)	X (Ext)	Y (Med)	Z (Ant)	Resultant
FEA	0.028	0.032	0.181	0.186
Experimental - 3D	0.060	0.080	0.080	0.130
% Difference	*53%*	*60%*	*127%*	*43%*
Experimental - 2D	-0.050	-0.010	0.410	0.410
% Difference	*156%*	*421%*	*56%*	*55%*

4.5 DISCUSSION

The purpose of this study was to develop a finite element model that gave similar relative fracture motion results to the experimental testing. A 3D model composed of various experimental components was successfully created to replicate the experimental setup. The results from this model did not initially align with the experimental data so a parametric analysis was conducted to refine the model and validate several assumptions. Additional experimental and computational measurements of the relative motion between the plates and femur were also taken to help to explain any remaining differences between the data.

Only one other study was found that compared experimental results of treating distal femur fractures to a FE model (Salas et al., 2011b). This study achieved good correlation (< 7% error in load at the maximum displacement) between their results for a distal femur fracture treated with either a locking plate or an intramedullary nail. However, only the deflection of the femoral head relative to femoral condyles was measured and no displacement information was reported for the relative fracture motion. The mesh for their locking plate model had 58,120 elements and 105,110 nodes. This was considerably less than the presented model (195,722 elements and 312,238 nodes) and suggests that sufficient mesh refinement was achieved for the current study.

Another study developed a FE model to compare treatment methods for a fracture just distal to a hip implant (Shah et al., 2011). A high correlation between the model and experimental testing was achieved upon comparison (R^2 = 0.92). However, only strain data and construct stiffness were obtained, which are not easily compared to the current study. The mesh for one of the models that contained a fracture plate, four screws and a hip prosthesis had 95,482 elements and 159,420 nodes after a convergence analysis was performed. Once again this mesh is considerably less refined than the mesh in the current study.

In the current study, agreement between the experimental and computational results was lower than expected. Compared to the 3D testing, the final iteration of the model had 0.07 mm lower compression (70% different), 0.04 mm higher medial shear (435% different), and 0.05 mm lower posterior shear (77% different). The discrepancy between the results is likely primarily due to simplification of the tab-slot interface. Experimentally, the relative motion in the 'compression' direction between the plates and the distal bone was 0.059 mm. However, in the model, measurement at the same two points gave only 0.008 mm of motion. This suggests that 0.051 mm of vertical motion occurs between the tab and the slot that is unaccounted for in the FE model due to the tie constraint. Similarly, the relative vertical motion between the plates and the proximal bone at the location of the locking screws was calculated to be 0.013 mm. However, since the screws are tied directly to the bone and the plates in the model, this relative motion could not occur. These two sources of error account for 0.064 mm of compression, which leaves only a difference of 0.006 mm between the 3D testing and FEA compression values. While not measured directly, both the tab-slot and plate-screw-bone simplifications could also contribute to the differences observed in the medial and posterior shear values.

The additional analyses investigating the variation in the alignment of the tibial components with respect to the femoral implant demonstrate that their position has a large effect on the relative fracture motion. Experimentally, the tibial tray was attached directly to the vertical actuator of the materials testing machine, which caused the articulating surface to be horizontal. The femoral implant was also adjusted to be horizontal using a level placed directly on the condylar surface. The repeatability observed in the experimental data suggests that there was minimal variation from true compressive loading and thus the ‘centered’ loading configuration used during the FEA was appropriate.

The results from the bending analysis fell between the 2D and 3D experimental results for each direction of motion. As expected, the bending load caused the largest motion in the anterior shear direction. Compared to the 3D testing, the final iteration of the model had 0.032 mm lower extension (53% different), 0.048 mm lower medial shear (60% different), and 0.101 mm higher anterior shear (127% different). Once again, some of the discrepancy between the results can likely be attributed to the simplified tab-slot interaction. A parametric analysis similar to the compression model could also assist in explaining some of the observed differences. However, the relatively high standard deviation for the 3D bending results (since only two samples were considered) makes comparison between the experimental and FEA data more difficult.

The Von Mises stress plots generated demonstrate the areas of peak stress in the construct. The maximum stress locations are at the tabs, around the screws and along the contoured surfaces of the plates. These stress values are currently below the yield stress for 316 stainless steel (205 MPa) suggesting that plastic deformation does not occur under the applied loads. However, the stress maps have not been validated as of yet since the primary objective of the model was to investigate relative fracture motion. Therefore, data should be obtained from strain gauges placed along the surface of the experimental model to verify the FEA stress / strain results.

There were a number of limitations to this study. The tab-slot simplification had the greatest effect on the difference in fracture motion between the FE model and the experimental testing. Proper modelling of this interaction would likely cause the results to better match the experimental values. A second limitation was the assumption of a coefficient of friction for the articulating surface. Although it may not significantly vary from the assumed 0.2, experimental testing should be performed to determine the actual coefficient between these surfaces. Another limitation was the assumption that the geometry of the medial and lateral plates matched the experimental setup perfectly. Manufacturing of the plates using the water jet cutter and CNC machining may have resulted in inconsistencies between the model and the final product. However, several measurements taken of the plates using a digital calliper confirmed that they were manufactured within ± 0.5 mm of the model. The variation in alignment of the plates on the femur is also something that the FE model does not consider. Experimentally, there was up to 5° of variation in the vertical alignment (in the anterior-posterior plane) of the plates on the synthetic femur. While this did not seem to heavily influence the standard deviation of the experimental results in compression, it may have contributed to the higher standard deviation observed for the bending results. Therefore, further analysis using the FE model should be performed to understand the effect of plate alignment on the results.

4.6 CONCLUSION

In conclusion, a FE model was developed to simulate the fracture motion that occurs for a periprosthetic fracture of the distal femur instrumented with the novel plates. Although the results did not yet achieve a high level of agreement with the experimental data, this difference may be reduced by further development of the model to address the limitations discussed above. Upon successful validation, the model can be used to investigate the stress distribution throughout the femur, optimize the plate geometry to minimize peak stresses and understand the response of the construct to additional loading configurations and higher loads.

CHAPTER 5: DISCUSION AND CONCLUSIONS

5.1 SUMMARY

With the increasing number of knee replacements being performed, treating periprosthetic fractures of the distal femur is becoming a common occurrence for orthopaedic surgeons (Streubel et al., 2010). Current treatment methods are inadequate and can lead to complication rates as high as 29% (Herrera et al., 2008). To address the high complication rates and poor management of these fractures, a novel treatment method was conceptualized whereby fixation would be enhanced through attachment of medial and lateral plates directly to the femoral prosthesis. Therefore, the overall purpose of this thesis was to design, manufacture and evaluate this bilateral plating method as a means to stabilize periprosthetic fractures of the distal femur.

The first objective of this project involved the design and manufacturing of the plates. Using 3D models of a synthetic femur and femoral prosthesis, medial and lateral plates were created with tabs that hook directly into pre-existing slots on the prosthesis. The plates were held in place using a transverse compression screw and several proximal locking screws. The completed design was then successfully manufactured from 316 stainless steel using a water jet cutter and CNC machining.

For the second objective of the project, the manufactured plates were experimentally compared to a single lateral plate by fixing a fractured synthetic femur with each method. The relative motion across the fracture site was tracked while compressive and bending loads were applied to each sample. Both 2D and 3D tracking demonstrated that total motion was successfully reduced to within the target range when the bilateral plates were used. This suggests that the proposed concept may be more capable of promoting enhanced healing of the fracture when compared to a current treatment method.

The final objective concerned the development of a finite element model to represent the experimental testing. Several iterations of the model were completed to reduce the differences between the computational and experimental results and investigate the most appropriate method of modeling the various input parameters. The fracture gap motion from the final model did not completely agree with the experimental data; however, additional experimental measurements of the relative motion between the plates and femur found that the majority of these differences could be attributed to the simplification of the tab-slot interaction. The presented results represent a significant step forward in the modeling of periprosthetic fracture treatment, and further refinement of the model would allow validation of the stress distribution and optimization of the plate design.

5.2 STRENGTHS AND LIMITATIONS

There are several general strengths and limitations to the presented research. The overall objective of evaluating a novel method for treating periprosthetic distal femur fractures is a topic that has not previously been researched. The majority of similar studies focus on treating distal femur fractures without a prosthesis and do not consider alternatives to commercially-available methods (Duffy et al., 2006; Heiney et al., 2009; Higgins et al., 2007; Otto et al., 2009; Salas et al., 2011a).

A further strength of the research was that the evaluation of the plates and interpretation of the results were focused on being clinically relevant. Many other studies lack an explanation of how their results can be interpreted clinically. While it is useful to know which device will provide the greatest amount of fixation, it is more useful to know if the results are clinically acceptable and relevant. Therefore, multiple loading configurations were tested at magnitudes that mimic rehabilitation loading of the femur (as opposed to destructive testing). The evaluation of the plates involved measuring the relative fracture motion between the fragments of bone, which is very important for understanding the ability of the fracture to heal.

The combination of experimental and computational analyses to assess the plates was also a strength of this research. Each method is important in the product design process and allows for a thorough evaluation of the mechanical construct. The use of a 3D motion capture system during experimental testing was novel in this field of study and shows potential over more traditional methods that are not able to rapidly capture 3D data. Other than the tab-slot interface, there were very few geometrical simplifications made to the finite element model from the experimental setup. This level of detail is often overlooked in similar orthopaedic finite element studies.

There are a number of limitations to the presented research that should be noted. The sample size of three during the 3D testing was quite small. However, for the primary measures the standard deviation was low enough to demonstrate significant differences with only three samples. Even after one of the bending tests had to be excluded due to excessive noise, significant differences were still observed. Also, the isolated compression and bending loading configurations were relatively simple compared to some of the dynamic unicompartmental loading that may be experienced *in vivo*. For samples treated with a single lateral plate, medial condyle loading has been shown to result in up to 60x greater displacement of the fracture gap than lateral condyle loading (Bong et al., 2002). These differences would likely be reduced with the double plated construct, as the addition of the medial plate would help to support the medial condyle and prevent excessive motion from occurring.

A further limitation was that only a simple transverse fracture was considered during testing. It has been reported that between 40-52% of periprosthetic fractures are associated with notching of the distal femoral cortex (performed during the TKR procedure) (Dennis, 2001). This suggests that some fractures are more complicated than just a simple transverse fracture. They likely originate at the notch and propagate up between the condyles to create a type of complex comminuted fracture. However, simple transverse fractures still occur frequently in patients, and testing of fixation devices on these types of fractures provides a good starting point for a biomechanical comparison.

Using percent fracture motion as a means to clinically assess performance has several inherent limitations. This metric is a function of fracture size and applied load so caution has to be taken when considering the results. It cannot be expected that every fracture encountered will have the same size and be exposed to the same loading. Nevertheless, it still provides a point of comparison for the presented data and encourages a clinical perspective to be taken when considering the results.

The present study also did not consider what might happen under higher loads that could cause failure. If the tabs were to fail or pull out of the slots, fracture healing could be jeopardized and additional complications could arise that may affect the function of the knee replacement. Loosening of the compression screw over time could contribute to this tab pull-out and is something that was not considered but should be investigated in the future. The physiological effects of adding the medial plate and the associated surgical risk should also be assessed. Finally, the plates were designed to match the geometry of a standard synthetic femur. It is unknown if the plates would perform equally for different femurs (size and bone quality) and how geometrical variation might impact function of the transverse compression screw guide. Regardless of these limitations, the presented studies still demonstrate the improved performance of the bilateral plates when compared to the single lateral plate.

5.3 RECOMMENDATIONS

The research presented in this thesis has demonstrated improved stability of the bilateral plating system compared to a lateral plate. Additional work should be performed to further understand the biomechanical and clinical performance of the plates. Conducting experimental tests under different loading configurations (e.g. unicompartmental loading) and increased magnitudes would reveal additional information about how the plates could fail and any resulting complications. Introducing more complicated fracture patterns into the testing would also assist in the comparison of the plates to current treatment methods and could highlight further benefits not yet noted. Successful treatment of these fractures with a traditional lateral plate or intramedullary nail requires sufficient screw purchase in the distal bone to achieve adequate stabilization. The multiple fragments in a complex fracture could jeopardize the distal bone quality and hinder the performance of these constructs. With the double plated construct, fracture fixation is primarily obtained through direct connection to the prosthesis as opposed to just relying on screw purchase in the distal bone. Therefore, stabilization would likely not be compromised when treating a complex fracture having multiple fragments.

Further development of the FE model to replicate the tab-slot interface would likely improve the agreement between experimental and computational results. In doing so, the model could then be used to optimize the plate geometry and validate the stress distribution throughout the construct and the femur. Improvements in the plate geometry could be made to ensure that its profile best matches the contours of the femur and that the tabs are sufficiently strong to prevent failure. Additional plate sizes could then be manufactured and tested on cadaveric femurs. Using an increased number of samples during this stage of testing along with the variability in geometry and bone quality of the cadaveric femurs would strengthen the results and their clinical relevance.

5.4 SIGNIFICANCE

In conclusion, a novel method for treating periprosthetic fractures of the distal femur has been successfully designed, manufactured and tested. The results of this thesis suggest that an alternative approach to treating this difficult fracture exists that is capable of improving fracture stabilization to promote enhanced healing and maintain alignment of the bone. Further refinement of the FE model can lead to a better understanding of how implants and fixation devices affect the stresses in the bone and the healing that follows. Also, the unique approach for gaining increased stabilization via the prosthesis is a technique that could be used elsewhere in the body for improved fracture treatment.

REFERENCES

Augat, P., Burger, J., Schorlemmer, S., et al. (2003). Shear movement at the fracture site delays healing in a diaphyseal fracture model. *Journal of orthopaedic research : official publication of the Orthopaedic Research Society*, *21*(6), 1011–7.

Bong, M., Egol, K. a, Koval, K. J., et al. (2002). Comparison of the LISS and a retrograde-inserted supracondylar intramedullary nail for fixation of a periprosthetic distal femur fracture proximal to a total knee arthroplasty. *The Journal of Arthroplasty*, *17*(7), 876–881.

Bottlang, M., Lesser, M., Koerber, J., et al. (2010). Far cortical locking can improve healing of fractures stabilized with locking plates. *The Journal of bone and joint surgery. American volume*, *92*(7), 1652–60.

Bougherara, H., Zdero, R., Mahboob, Z., et al. (2010). The biomechanics of a validated finite element model of stress shielding in a novel hybrid total knee replacement. *Proceedings of the Institution of Mechanical Engineers, Part H: Journal of Engineering in Medicine*, *224*(10), 1209–1219.

Carter, D., & Spengler, D. (1982). *Biomechanics of fracture. In: Sumner-Smith ed. Bone in clinical orthopaedics: a study in comparative osteology.* (pp. 305–334). Philadelphia: WB Saunders.

Cheung, G., Zalzal, P., Bhandari, M., et al. (2004). Finite element analysis of a femoral retrograde intramedullary nail subject to gait loading. *Medical Engineering & Physics*, *26*(2), 93–108.

Claes, L., Augat, P., Suger, G., et al. (1997). Influence of size and stability of the osteotomy gap on the success of fracture healing. *Journal of orthopaedic research□: official publication of the Orthopaedic Research Society*, *15*(4), 577–84.

Claes, L. E., & Heigele, C. a. (1999). Magnitudes of local stress and strain along bony surfaces predict the course and type of fracture healing. *Journal of biomechanics*, *32*(3), 255–66.

Cunningham, J. L. (2001). The biomechanics of fracture fixation. *Current Orthopaedics*, (5), 457–464.

Dennis, D. a. (2001). Periprosthetic fractures following total knee arthroplasty. *Instructional course lectures*, *50*, 379–89.

Downing, M. R., Ashcroft, P. B., Johnstone, A. J., et al. (2008). Assessment of inducible fracture micromotion in distal radial fractures using radiostereometry. *Journal of orthopaedic trauma*, *22*(8 Suppl), S96–105.

Duffy, P., Trask, K., Hennigar, a, et al. (2006). Assessment of fragment micromotion in distal femur fracture fixation with RSA. *Clinical orthopaedics and related research*, *448*(448), 105–13.

Egol, K. A., Kubiak, E. N., Fulkerson, E., et al. (2004). Biomechanics of locked plates and screws. *Journal of orthopaedic trauma*, *18*(8), 488–93.

Fitzpatrick, D. C., Doornink, J., Madey, S. M., et al. (2009). Relative stability of conventional and locked plating fixation in a model of the osteoporotic femoral diaphysis. *Clinical Biomechanics*, *24*(2), 203–209.

Gautier, E. (2003). Guidelines for the clinical application of the LCP. *Injury*, *34*, 63–76.

Hamblen, D. L., & Simpson, H. R. W. (2007). *Adams's Outline of Fractures: Including Joint Injuries* (p. 328). Edinburgh: Churchill Livingstone Elsevier.

Heiney, J. P., Barnett, M. D., Vrabec, G. a, et al. (2009). Distal femoral fixation: a biomechanical comparison of trigen retrograde intramedullary (I.M.) nail, dynamic condylar screw (DCS), and locking compression plate (LCP) condylar plate. *The Journal of trauma*, *66*(2), 443–9.

Herrera, D. a, Kregor, P. J., Cole, P. a, et al. (2008). Treatment of acute distal femur fractures above a total knee arthroplasty: systematic review of 415 cases (1981-2006). *Acta orthopaedica*, *79*(1), 22–7.

Hertel, R., Eijer, H., Meisser, A., et al. (2001). Biomechanical and biological considerations relating to the clinical use of the Point Contact-Fixator--evaluation of the device handling test in the treatment of diaphyseal fractures of the radius and/or ulna. *Injury*, *32 Suppl 2*, B10–B14.

Higgins, T. F., Pittman, G., Hines, J., et al. (2007). Biomechanical analysis of distal femur fracture fixation: fixed-angle screw-plate construct versus condylar blade plate. *Journal of orthopaedic trauma*, *21*(1), 43–6.

Jaakkola, J. I., Lundy, D. W., Moore, T., et al. (2002). Supracondylar femur fracture fixation, *73*(1), 72–76.

Kim, D.-W., Lee, K.-Y., Jun, Y., et al. (2011). Friction and wear characteristics of UHMWPE against Co-Cr alloy under the wide range of contact pressures in lumbar total disc replacement. *International Journal of Precision Engineering and Manufacturing*, *12*(6), 1111–1118.

Kurtz, S., Ong, K., Lau, E., et al. (2007). Projections of primary and revision hip and knee arthroplasty in the United States from 2005 to 2030. *The Journal of bone and joint surgery. American volume*, *89*(4), 780–5.

Marti, A., Fankhauser, C., Frenk, A., et al. (2001). Biomechanical evaluation of the less invasive stabilization system for the internal fixation of distal femur fractures. *Journal of orthopaedic trauma*, *15*(7), 482–7.

McGraw, P., & Kumar, A. (2010). Periprosthetic fractures of the femur after total knee arthroplasty. *Journal of orthopaedics and traumatology□: official journal of the Italian Society of Orthopaedics and Traumatology*, *11*(3), 135–41.

Nauth, A., Ristevski, B., Bégué, T., et al. (2011). Periprosthetic distal femur fractures: current concepts. *Journal of orthopaedic trauma*, *25 Suppl 2*, S82–5.

Otake, N., Chen, H., Yao, X., et al. (2007). Morphologic study of the lateral and medial collateral ligaments of the human knee. *Okajimas folia anatomica Japonica*, *83*(4), 115–22.

Otto, R. J., Moed, B. R., & Bledsoe, J. G. (2009). Biomechanical comparison of polyaxial-type locking plates and a fixed-angle locking plate for internal fixation of distal femur fractures. *Journal of orthopaedic trauma*, *23*(9), 645–52.

Perren, S. M. (2002). Evolution of the internal fixation of long bone fractures. The scientific basis of biological internal fixation: Choosing a new balance between stability and biology. *The Journal of Bone and Joint Surgery*, *84-B*(8), 1093–1110.

Platzer, P., Schuster, R., Aldrian, S., et al. (2010). Management and outcome of periprosthetic fractures after total knee arthroplasty. *The Journal of trauma*, *68*(6), 1464–70.

Salas, C., Mercer, D., DeCoster, T. a, et al. (2011a). Experimental and probabilistic analysis of distal femoral periprosthetic fracture: a comparison of locking plate and intramedullary nail fixation. Part A: experimental investigation. *Computer methods in biomechanics and biomedical engineering*, *14*(2), 157–64.

Salas, C., Mercer, D., DeCoster, T. a, et al. (2011b). Experimental and probabilistic analysis of distal femoral periprosthetic fracture: a comparison of locking plate and intramedullary nail fixation. Part B: probabilistic investigation. *Computer methods in biomechanics and biomedical engineering*, *14*(2), 175–82.

Shah, S., Kim, S. Y. R., Dubov, a., et al. (2011). The biomechanics of plate fixation of periprosthetic femoral fractures near the tip of a total hip implant: cables, screws, or both? *Proceedings of the Institution of Mechanical Engineers, Part H: Journal of Engineering in Medicine*, *225*(9), 845–856.

Sirouspour, S. (2012). Spatial Description of a Rigid Body [Lecture Note 3]. *EE4BE4: Medical Robotics, McMaster University*.

Streubel, P. N., Gardner, M. J., Morshed, S., et al. (2010). Are extreme distal periprosthetic supracondylar fractures of the femur too distal to fix using a lateral locked plate? *The Journal of bone and joint surgery. British volume*, *92*(4), 527–34.

Stryker. (2012). Scorpio NRG - Surgical Protocol. *Stryker Orthopaedics*, 1–54.

Uhthoff, H. K., Poitras, P., & Backman, D. S. (2006). Internal plate fixation of fractures: short history and recent developments. *Journal of orthopaedic science□: official journal of the Japanese Orthopaedic Association*, *11*(2), 118–26.

Wagner, M. (2003). General principles for the clinical use of the LCP. *Injury*, *34*, 31–42.

Winemaker, M. (2007). Periprosthetic Distal Femur Fractures [Presentation]. *The Hamilton Arthroplasty Group*.

Zdero, R., Olsen, M., Bougherara, H., et al. (2008). Cancellous bone screw purchase: a comparison of synthetic femurs, human femurs, and finite element analysis. *Proceedings of the Institution of Mechanical Engineers, Part H: Journal of Engineering in Medicine*, *222*(8), 1175–1183.

Zehntner, M. K., & Ganz, R. (1993). Internal fixation of supracondylar fractures after condylar total knee arthroplasty. *Clinical orthopaedics and related research*, *293*, 219–224.

Zlowodzki, M., Williamson, S., Cole, P. a, et al. (2004). Biomechanical evaluation of the less invasive stabilization system, angled blade plate, and retrograde intramedullary nail for the internal fixation of distal femur fractures. *Journal of orthopaedic trauma*, *18*(8), 494–502.

Zlowodzki, M., Williamson, S., Zardiackas, L. D., et al. (2006). Biomechanical evaluation of the less invasive stabilization system and the 95-degree angled blade plate for the internal fixation of distal femur Fractures in human cadaveric bones with high bone mineral density. *The Journal of trauma*, *60*(4), 836–40.

APPENDICES

APPENDIX A: DETAILED DRAWINGS OF THE MEDIAL AND LATERAL PLATES

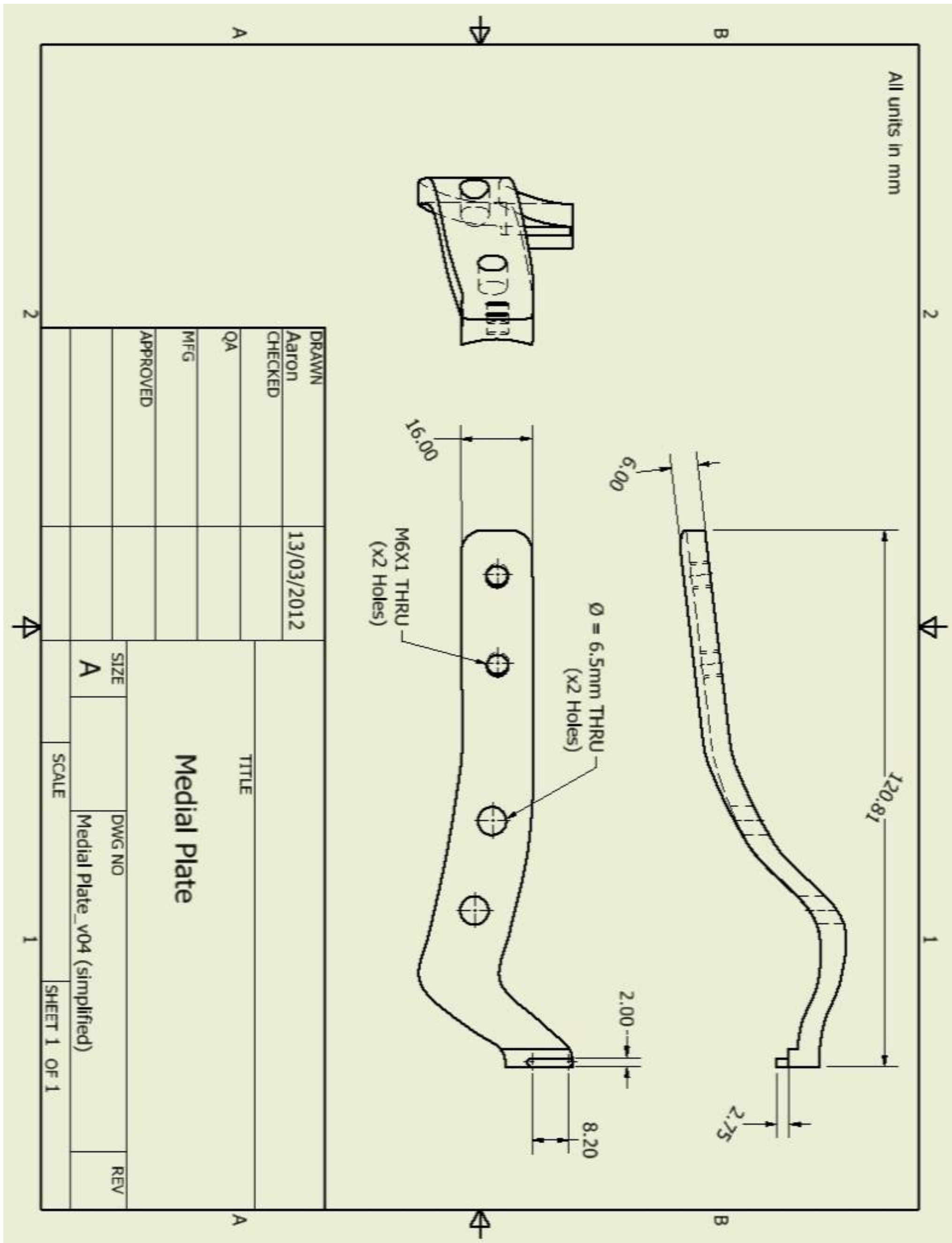

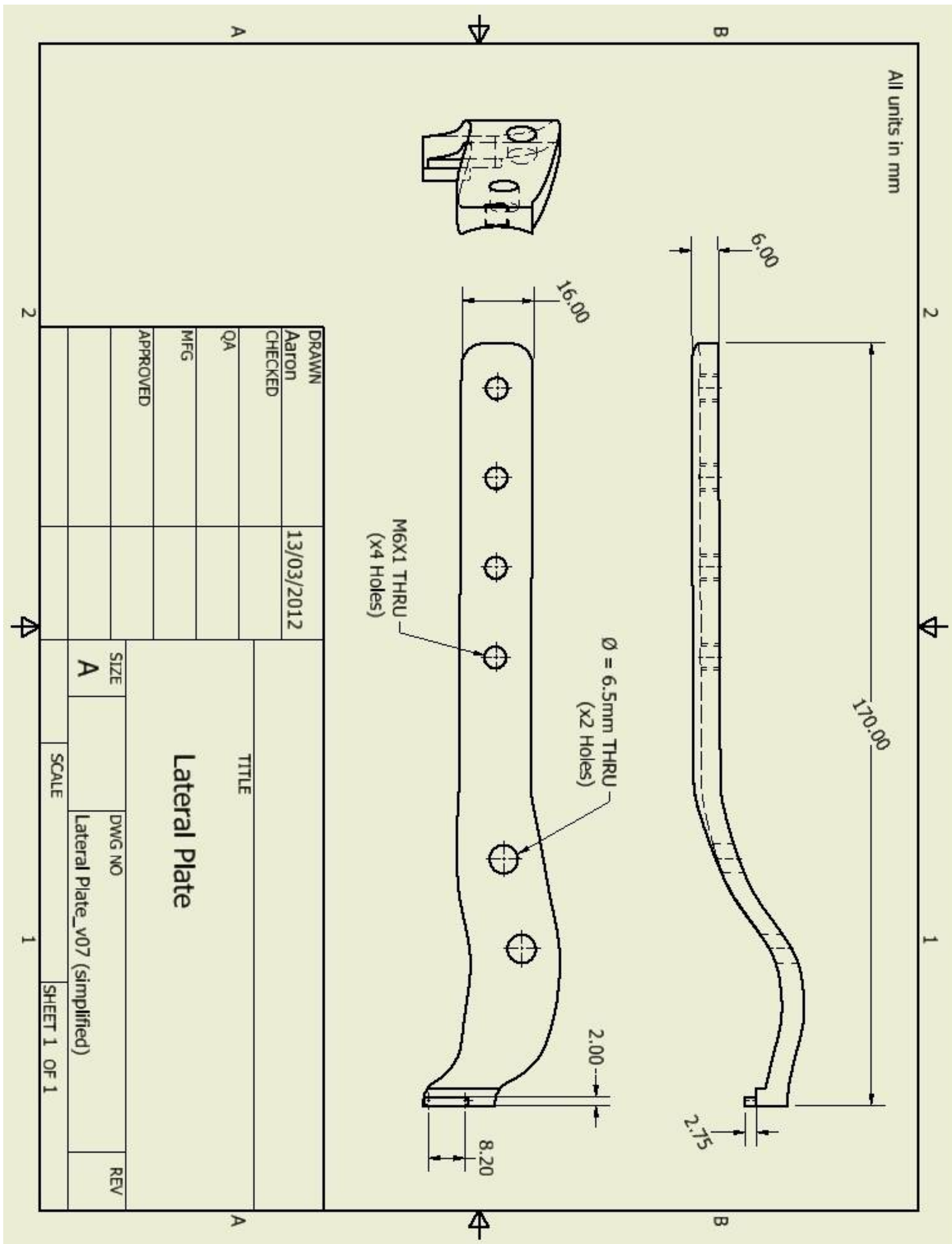
All units in mm
6.00
16.00
170.00
M6X1 THRU
(x4 Holes)
Ø = 6.5mm THRU
(x2 Holes)
2.00
2.75
8.20
DRAWN
Aaron
13/03/2012
CHECKED
QA
MFG
APPROVED
TITLE
Lateral Plate
SIZE
A
DWG NO
Lateral Plate_v07 (simplified)
REV
SCALE
SHEET 1 OF 1

APPENDIX B: VISUALIZATION OF THE SURGICAL PROCEDURE

The following is a detailed visualization of the proposed surgical procedure for creating the transverse compression screw hole and implanting the bilateral plates.

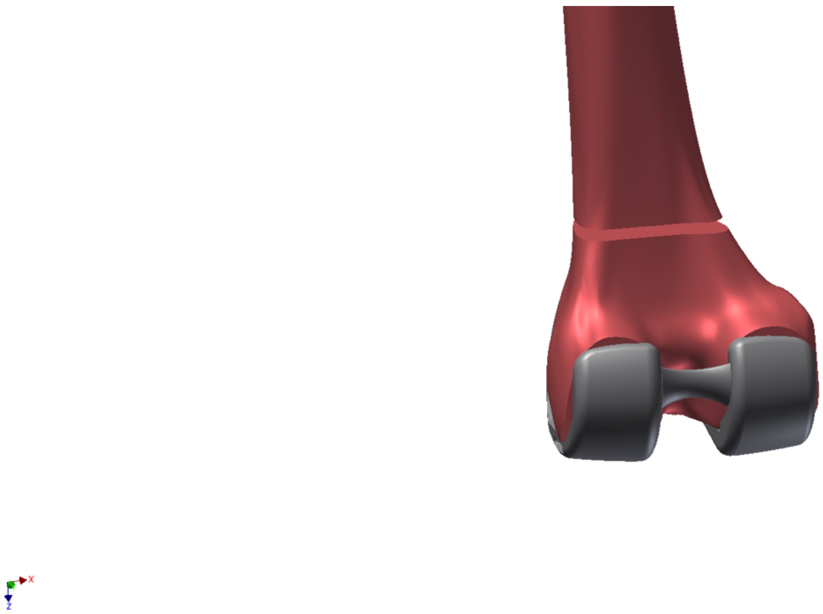

1) A periprosthetic fracture is shown in the 3D model of the femur.

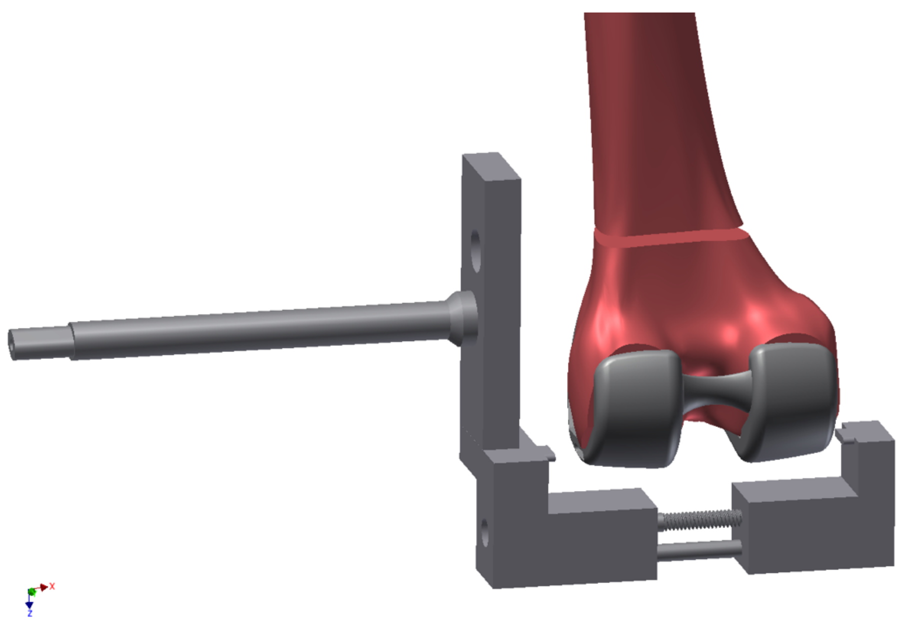

2) The custom drill guide is aligned with the femoral component.

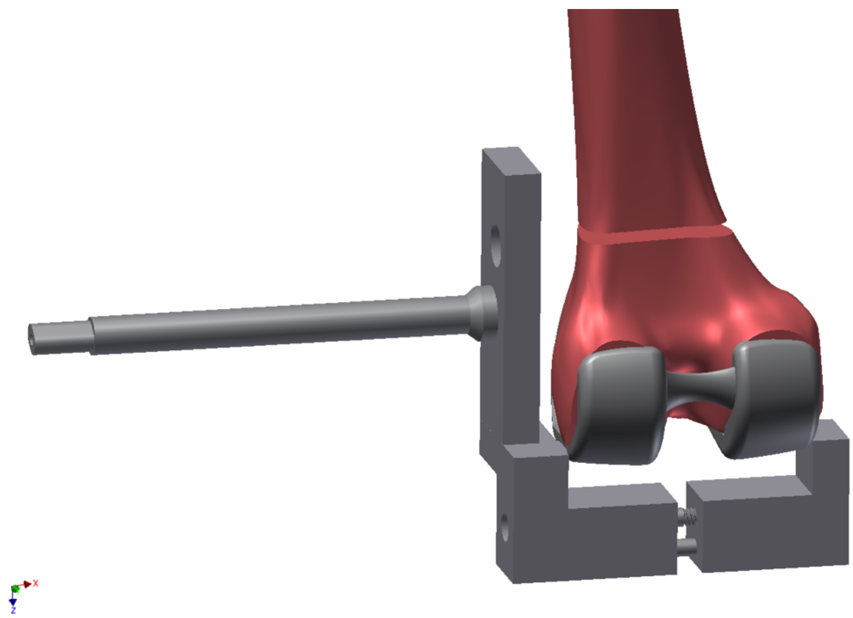

3) A screw is tightened to clamp the guide around the prosthesis. The guide has tabs similar to the plates that hook directly into the slots and provide a reference point for the compression screw hole.

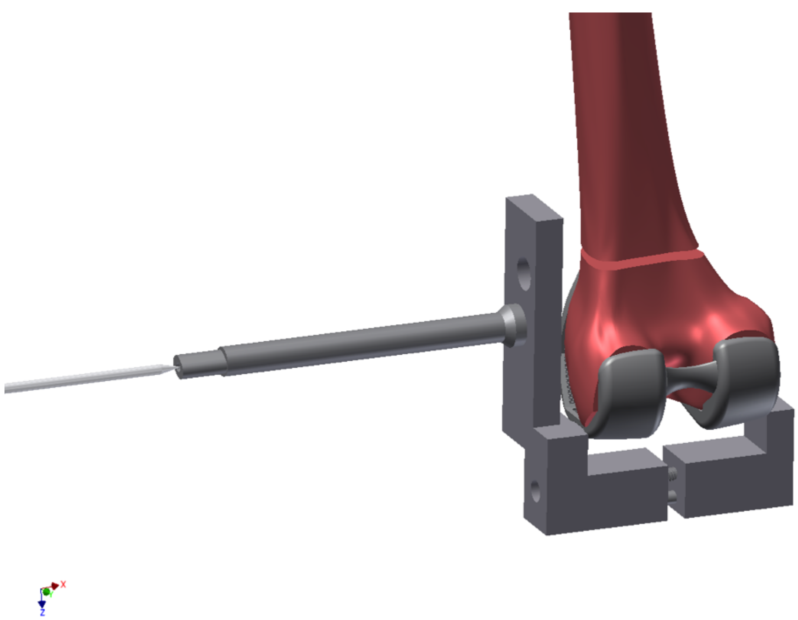

4) Using a surgical drill, a K-wire (3.2-mm diameter: Stryker [1210-6450]) is inserted into the drill sleeve at the pre-determined location for the clearance hole into which the transverse compression screw is inserted.

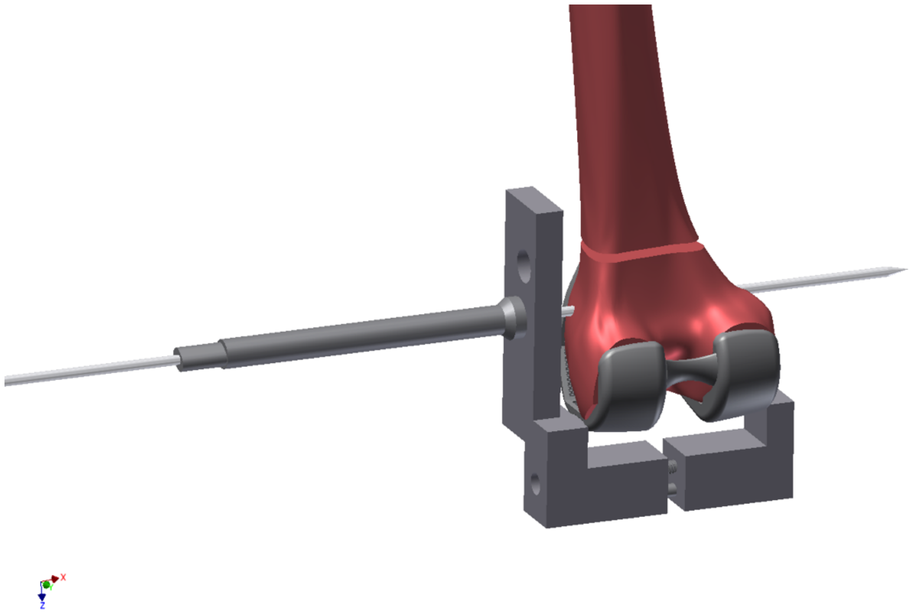

5) The K-wire is drilled through the distal femur.

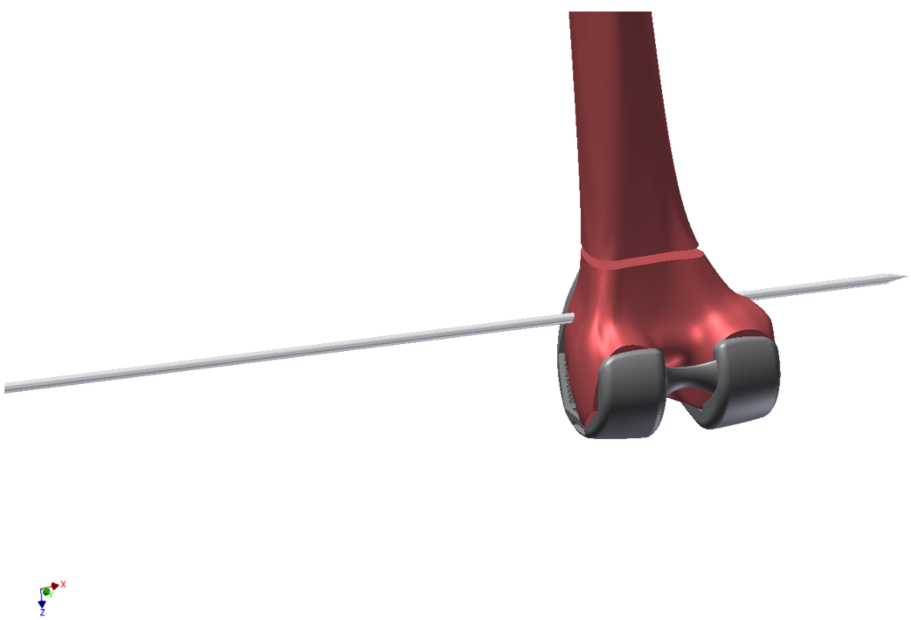

6) The K-wire is left in the distal bone while the drill guide is removed from the area. The K-wire remains at the proper location and orientation for the compression screw hole.

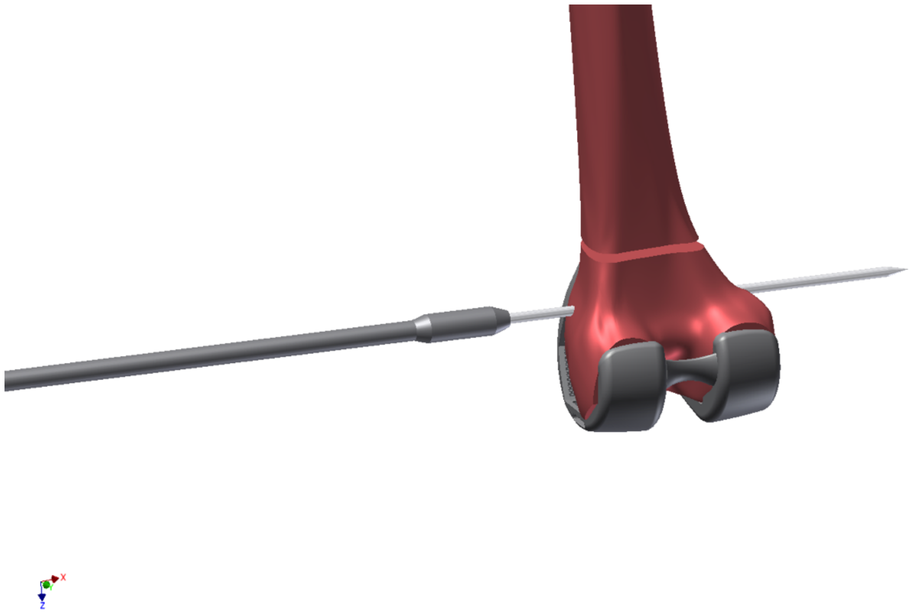

7) A 10-mm diameter cannulated drill bit (10-mm outer diameter: Stryker [1806-2010]) is fitted over top of the K-wire and the surgical drill is used to bore out the clearance hole to the correct diameter.

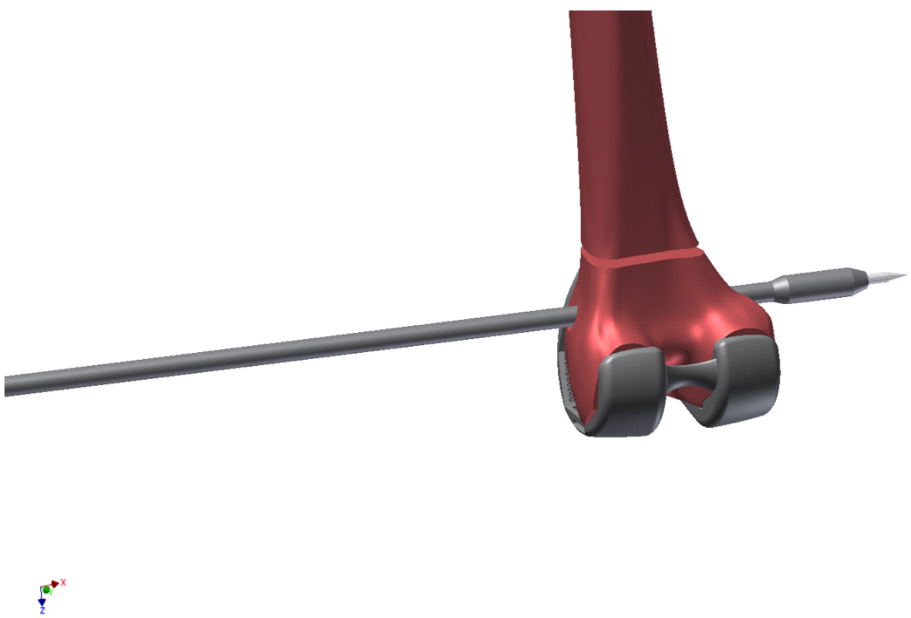

8) The cannulated drill bit is fully inserted into the distal bone.

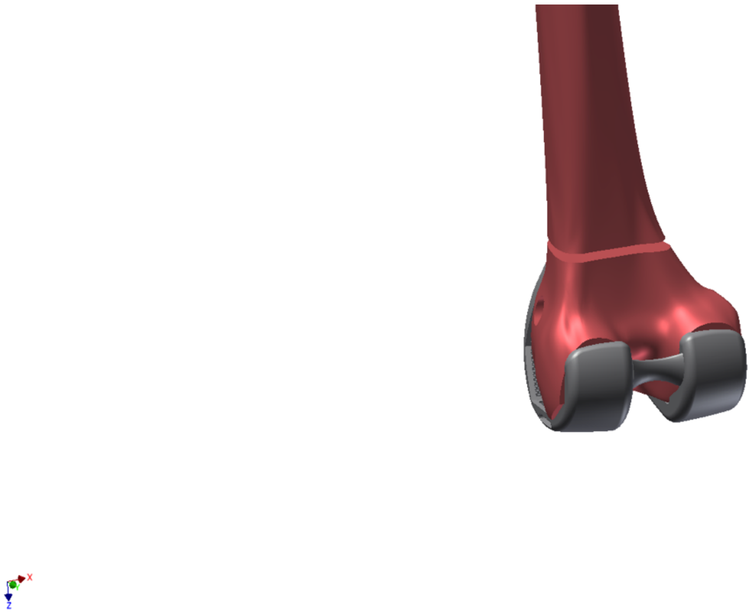

9) The drill bit and K-wire are removed from the bone.

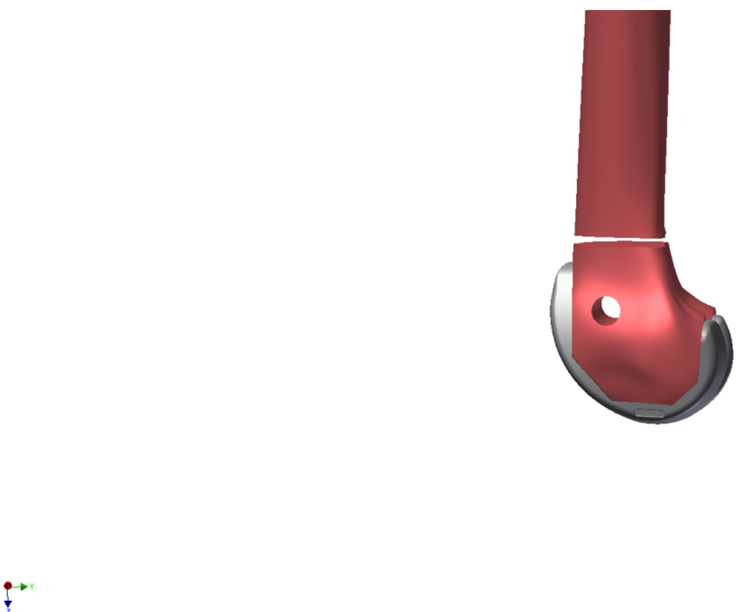

10) Side profile of the femur showing the clearance hole for the transverse compression screw.

11) The tabs of the medial and lateral plates are inserted into the slots on the femoral prosthesis and aligned with the proximal femur. Any manual adjustment / bending of the plates to match the bone profile takes place at this time.

12) The transverse compression screw is inserted through the matching holes on the plates and into the bone. A nut on the end of the screw is tightened to apply a compressive force to the plates and hold them in place. Proximal locking screws are inserted as necessary on either plate to fix the alignment of the prosthesis with respect to the proximal bone.

APPENDIX C: DETAILED DRAWING OF THE CUSTOM DRILL GUIDE

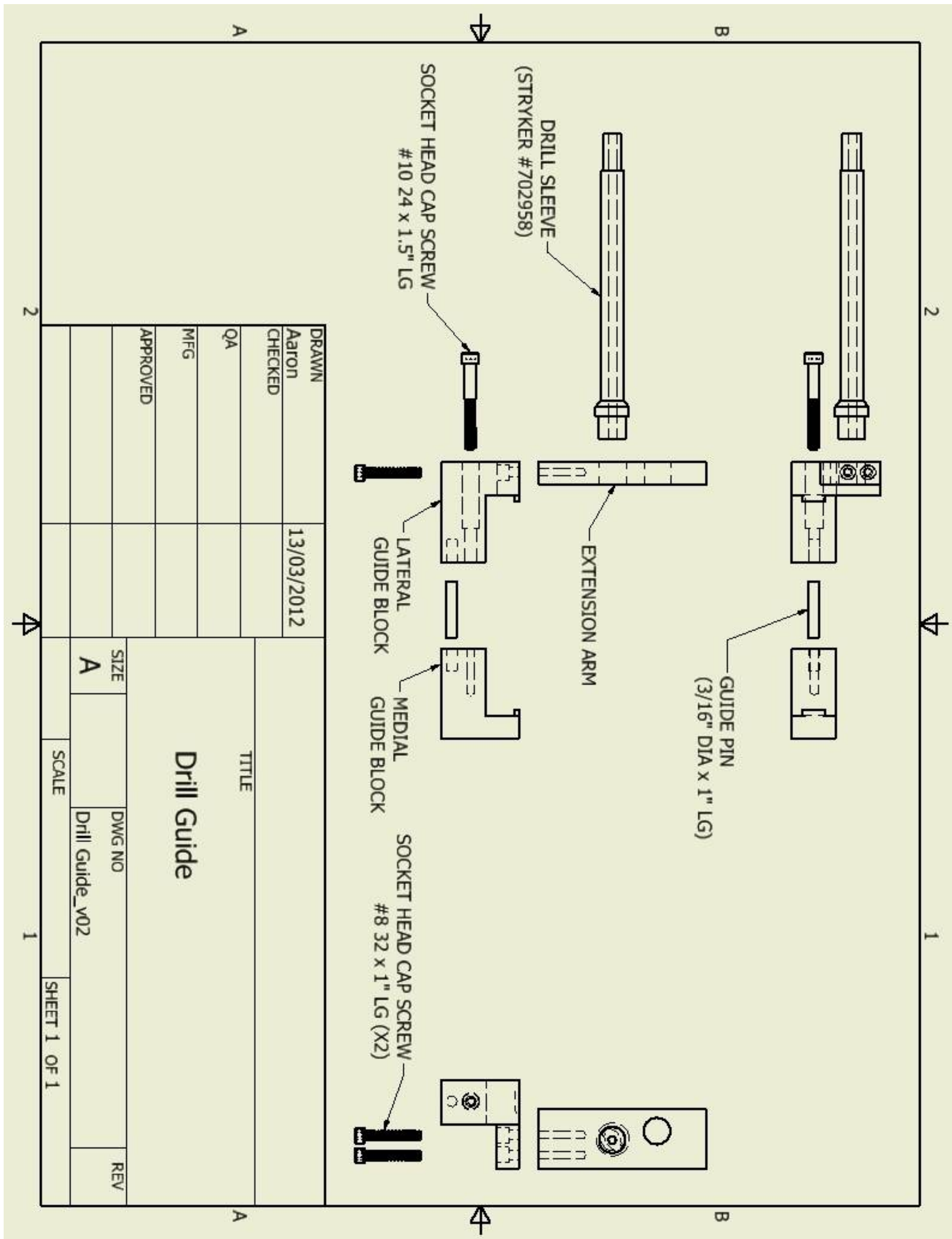

APPENDIX D: FASTENER DETAILS

The following is a summary of the fasteners used during implantation of the single lateral plate and the bilateral plate with and without distal screws.

<table>
<tr><th></th><th>Single Lateral Plate</th><th colspan="2">Bilateral Plates</th><th colspan="2">Bilateral Plates;
2 Distal Screws</th></tr>
<tr><td>PROXIMAL</td><td>40*</td><td rowspan="4">Lateral Plate</td><td>44*</td><td rowspan="6">Lateral Plate</td><td>44*</td></tr>
<tr><td></td><td>40*</td><td>44*</td><td>44*</td></tr>
<tr><td></td><td>42***</td><td>28*</td><td>28*</td></tr>
<tr><td></td><td>44*</td><td>30*</td><td>30*</td></tr>
<tr><td></td><td>80**</td><td rowspan="2">Medial Plate</td><td>20*</td><td>26*</td></tr>
<tr><td></td><td>75*</td><td>24*</td><td>75*</td></tr>
<tr><td></td><td>24*</td><td rowspan="2" colspan="2"></td><td rowspan="2">Medial Plate</td><td>20*</td></tr>
<tr><td>DISTAL</td><td>24*</td><td>24*</td></tr>
</table>

*** - AxSOS 5.0 mm cortical locking screw**

**** - AxSOS 4.5 mm SPS cancellous screw**

***** - AxSOS 6.5 mm SPS cancellous full thread screw**

APPENDIX E: TEST SETUP – COMPRESSION LOADS

The following is a summary of the setup-up and test protocol for conducting the compressive load tests.

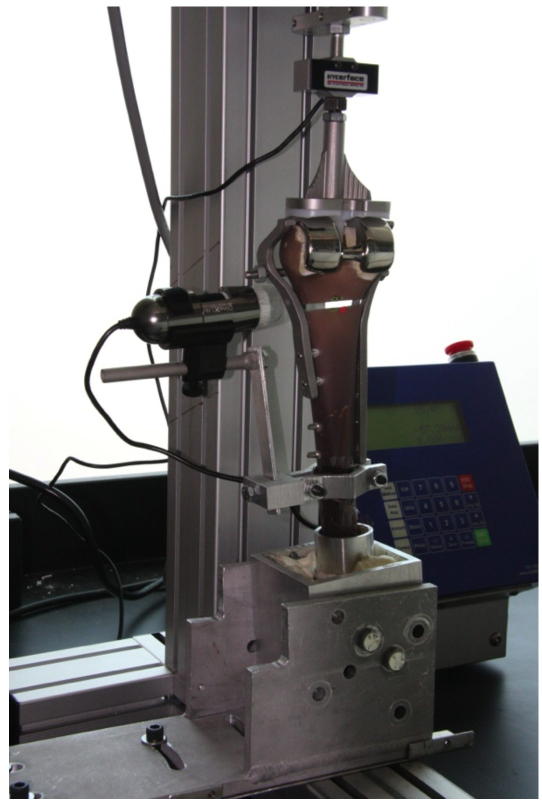

1. Secure the polyethylene tibial insert into the tibial tray and screw into 300-lbs load cell. Attach load cell to the ADMET. Visually align the tray so that the medial-lateral plane of the tray is parallel to the ADMET. Tighten the nuts to secure the load cell and tray.
2. Slide sample holder onto aluminum extrusion slots on ADMET as shown on the right.
3. Insert the potted femur into the circular opening of the sample holder and align with polyethylene insert. Insert spacer below the rectangular box to set height of the femur and tighten the 2 set screws on rectangular box.
4. Use a handheld level to ensure the condyles of the femoral prosthesis are horizontal. Tighten the 4 bolts that clamp the rectangular box to secure its position.
5. Move sample into place under the polyethylene insert and slowly lower (10mm/s) the actuator until a compressive load of approximately 30 N is obtained. Adjust the femur (rotation and translation) until the load observed on the ADMET is at its lowest value. Tighten the 2 bolts connecting the holder to the ADMET frame.
6. Slowly raise the loading actuator until a 0 N load of achieved and zero the displacement reading on the ADMET.
7. Attach the digital microscope (DinoLite) to the femur using the padded clamp. Use the DinoLite software to focus the microscope and ensure that all of the markers are in the field of view (allow adequate room for movement of markers).

APPENDIX F: TEST SETUP – BENDING LOADS

The following is a summary of the setup-up and test protocol for conducting the bending load tests.

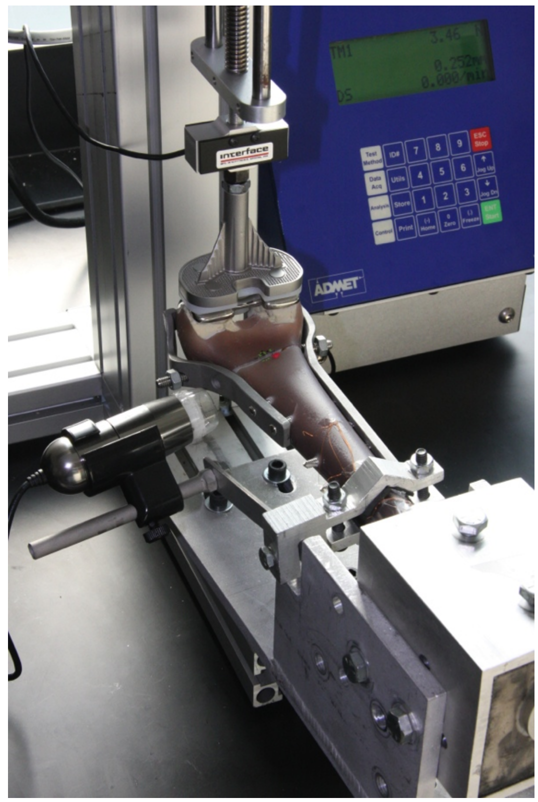

1. Secure the polyethylene tibial insert into the tibial tray and screw into 300 lbs load cell. Attach load cell to the ADMET. Visually align the tray so that the medial-lateral plane of the tray is parallel to the ADMET. Tighten the nuts to secure the load cell and tray.
2. Slide sample holder onto aluminum extrusion slots on ADMET as shown on the right. Be sure to tighten the 4 bolts on the side of the holder that clamp the rectangular box.
3. Insert the potted femur into the circular opening of the sample holder and align with polyethylene insert.
4. Use a handheld level to ensure the condyles of the femoral prosthesis are horizontal. Tighten the 2 set screws on the top of the rectangular box to secure the position of the sample.
5. Move sample into place under the polyethylene insert and slowly lower (10mm/s) the actuator until a compressive load of approximately 30 N is obtained. Adjust the femur (rotation and translation) until the load observed on the ADMET is at its lowest value. Tighten the 3 socket head cap screws connecting the holder to the ADMET frame.
6. Slowly raise the loading actuator until a 0 N load of achieved and zero the displacement reading on the ADMET.
7. Attach the digital microscope (DinoLite) to the femur using the padded clamp. Use the DinoLite software to focus the microscope and ensure that all of the markers are in the field of view (allow adequate room for movement of markers).

APPENDIX G: 2D TEST RESULTS FOR EACH CONSTRUCT

The following is a summary of the results obtained for each construct using the 2D analysis.

	View	Motion	LAT		DBL		DBL2	
Posterior Load (500N)	**Medial**	Shear (Ant) [mm]	*1.26*	*± 0.00*	*0.88*	*± 0.02*	*0.82*	*± 0.01*
		Extension [mm]	*0.67*	*± 0.01*	*0.20*	*± 0.04*	*0.04*	*± 0.00*
		Rotation [deg]	*0.4°*	*± 0.09*	*0.0°*	*± 0.14*	*0.8°*	*± 0.16*
	Posterior	Shear (Med) [mm]	*0.21*	*± 0.01*	*0.25*	*± 0.03*	*-0.01*	*± 0.00*
		Compression [mm]	*-0.22*	*± 0.00*	*0.20*	*± 0.02*	*0.09*	*± 0.00*
		Neg. Rotation [deg]	*0.4°*	*± 0.04*	*0.0°*	*± 0.09*	*0.0°*	*± 0.01*
Axial Load (600N)	**Medial**	Shear (Post) [mm]	*0.10*	*± 0.01*	*0.01*	*± 0.02*	*0.16*	*± 0.01*
		Compression [mm]	*1.07*	*± 0.02*	*0.06*	*± 0.01*	*0.08*	*± 0.00*
		Neg. Rotation [deg]	*0.7°*	*± 0.09*	*0.1°*	*± 0.11*	*0.1°*	*± 0.21*
	Posterior	Shear (Lat) [mm]	*0.07*	*± 0.00*	*0.04*	*± 0.01*	*0.02*	*± 0.00*
		Compression [mm]	*0.78*	*± 0.02*	*0.07*	*± 0.01*	*0.08*	*± 0.00*
		Rotation [deg]	*0.9°*	*± 0.03*	*0.0°*	*± 0.06*	*0.1°*	*± 0.07*

APPENDIX H: RIGID BODY VERIFICATION (LATERAL PLATE)

The following is a summary of the results obtained from the rigid body verification conducted for the 2D analysis.

	View	Segment	AVG Segment Length SD (mm)	Motion (mm)		Potential Error (Distal Segment)	
				Shear	Compression	Shear	Compression
Posterior Load (500N)	Medial	Proximal	0.0023	1.262	-0.673	0.8%	-1.6%
		Distal	0.0104				
	Posterior	Proximal	0.0234	0.208	-0.222	16.1%	-15.2%
		Distal	0.0336				
Axial Load (600N)	Medial	Proximal	0.0028	-0.099	1.070	-4.0%	0.4%
		Distal	0.0040				
	Posterior	Proximal	0.0049	-0.073	0.778	-9.4%	0.9%
		Distal	0.0069				

"Potential Error" sample calculation:
0.0104 / 1.262 = 0.8%

APPENDIX I: 3D TEST RESULTS FOR EACH CONSTRUCT

The following is a summary of the results obtained for each construct using the 2D analysis.

		Sample	X [mm]	(STD DEV)	Y [mm]	(STD DEV)	Z [mm]	(STD DEV)	Resultant [mm]	(SD)
Lateral Plate	Bending	2	0.20	(±0.06)	0.15	(±0.05)	-0.36	(±0.05)	0.45	(±0.04)
		4	0.14	(±0.03)	0.14	(±0.05)	-0.29	(±0.02)	0.35	(±0.04)
		6	0.19	(±0.00)	0.20	(±0.00)	-0.29	(±0.00)	0.40	(±0.00)
		AVG	**0.18**	***(±0.04)***	**0.16**	***(±0.03)***	**-0.32**	***(±0.04)***	**0.40**	***(±0.05)***
	Compression	2	-0.67	(±0.03)	-0.14	(±0.02)	0.11	(±0.02)	0.69	(±0.03)
		4	-0.47	(±0.01)	0.02	(±0.00)	0.12	(±0.01)	0.49	(±0.00)
		6	-0.62	(±0.01)	-0.03	(±0.02)	0.20	(±0.01)	0.66	(±0.02)
		AVG	**-0.59**	***(±0.10)***	**-0.05**	***(±0.08)***	**0.15**	***(±0.05)***	**0.61**	***(±0.11)***

		Sample	X [mm]	(STD DEV)	Y [mm]	(STD DEV)	Z [mm]	(STD DEV)	Resultant [mm]	(SD)
Double Plate 2	Bending	1	-	-	-	-	-	-	-	-
		3	0.10	(±0.05)	0.11	(±0.03)	-0.12	(±0.01)	0.20	(±0.00)
		5	0.01	(±0.01)	0.05	(±0.00)	-0.04	(±0.00)	0.06	(±0.00)
		AVG	**0.06**	***(±0.06)***	**0.08**	***(±0.05)***	**-0.08**	***(±0.06)***	**0.13**	***(±0.10)***
	Compression	1	-0.12	(±0.00)	-0.03	(±0.01)	0.06	(±0.00)	0.13	(±0.00)
		3	-0.09	(±0.02)	0.03	(±0.02)	0.08	(±0.01)	0.13	(±0.00)
		5	-0.07	(±0.00)	-0.03	(±0.02)	0.09	(±0.01)	0.12	(±0.01)
		AVG	**-0.10**	***(±0.02)***	**-0.01**	***(±0.04)***	**0.07**	***(±0.02)***	**0.13**	***(±0.01)***

APPENDIX J: FE MODEL MESH INFORMATION

The following is a summary of the number of elements and nodes for each part of the FE model. The number of nodes is displayed for the both types of analyses (linear elements and quadratic elements).

Part	# of Elements	# of Nodes (Linear Analysis)	# of Nodes (Quadratic Analysis)
Proximal Femur (Cancellous)	11536	3135	20189
Proximal Femur (Cortical)	19911	5511	35257
Distal Femur (Cancellous)	5255	1217	8359
Distal Femur (Cortical)	3923	1435	8223
Plates-Screws-Prosthesis	38015	10033	64820
PE Tibial Insert	5007	1257	8290
Tibial Tray	112075	23108	167100
Total:	**195722**	**45696**	**312238**